STUDY OF Ni(111) WITH OXYGEN ADSORPTION BY ANGLE-RESOLVED PHOTOEMISSION

Somchai Chumpolkulwong

A Thesis Submitted in Partial Fulfillment of the Requirements for

the Degree of Doctor of Philosophy in Physics

Suranaree University of Technology

Academic Year 2007

การศึกษานิกเกิล (111) ที่ดูดซับออกซิเจนโดยเทคนิคโฟโตอิมิชชันแบบแยกแยะเชิงมุม

นายสมชาย ชุมพลกุลวงศ์

วิทยานิพนธ์นี้เป็นส่วนหนึ่งของการศึกษาตามหลักสูตรปริญญาวิทยาศาสตรดุษฎีบัณฑิต
สาขาวิชาฟิสิกส์
มหาวิทยาลัยเทคโนโลยีสุรนารี
ปีการศึกษา 2550

STUDY OF Ni (111) WITH OXYGEN ADSORPTION BY ANGLE-RESOLVED PHOTOEMISSION

Suranaree University of Technology has approved this thesis submitted in partial fulfillment of the requirements for the Degree of Doctor of Philosophy.

Thesis Examining Committee

_____

(Assoc. Prof. Dr. Prapun Manyum)

Chairperson

_____

(Asst. Prof. Dr. Prayoon Songsiriritthigul)

Member (Thesis Advisor)

_____

(Prof. Dr. Sukit Limpijumnong)

Member

_____

(Dr. Saroj Rujirawat)

Member

_____

(Dr. Hideki Nakajima)

Member

_____ _____

(Assoc. Prof. Dr. Saowanee Rattanaphani) (Assoc. Prof. Dr. Sompong Thammathaworn)

Vice Rector for Academic Affairs Dean of Institute of Science

สมชาย ชุมพลกุลวงศ์ : การศึกษานิกเกิล (111) ที่ดูดซับออกซิเจนโดยเทคนิคโฟโตอิมิชชันแบบแยกแยะเชิงมุม (STUDY OF Ni(111) WITH OXYGEN ADSORPTION BY ANGLE-RESOLVED PHOTOEMISSION) อาจารย์ที่ปรึกษา : ผู้ช่วยศาสตราจารย์ ดร.ประยูร ส่งสิริฤทธิกุล, 170 หน้า.

โครงสร้างอิเล็กทรอนิกส์ของผิวโลหะนิกเกิล (111) และผิวของโลหะนิกเกิล (111) ที่มีการดูดซับออกซิเจนถูกศึกษาโดยเทคนิคโฟโตอิมิชชันแบบแยกแยะเชิงมุม บริเวณผิวของโลหะนิกเกิล (111) มีการจัดเรียงตัวของอะตอมใหม่เมื่อมีการดูดซับอะตอมของออกซิเจน ลักษณะการจัดเรียงตัวขึ้นอยู่กับปริมาณของอะตอมของออกซิเจน พบว่าเมื่อปริมาณของอะตอมของออกซิเจนมีเทียบเท่ากับ 0.51 และ 0.88 ของปริมาณอะตอมที่อยู่ในระนาบ (111) จะมีการจัดเรียงตัวใหม่ในลักษณะ c(2×2) และ p(1×1) ตามลำดับ การกระจายของพลังงานในมิติของโมเมนตัมหรือความสัมพันธ์ระหว่างพลังงาน และโมเมนตัมที่มีผลมาจากอะตอมของออกซิเจนที่ดูดซับหาได้จากผลต่างของสเปกตรัมที่วัดได้จากโลหะนิเกิล (111) ที่สะอาด และสเปกตรัมที่วัดได้จากโลหะนิเกิล (111) ที่มีการดูดซับออกซิเจน เมื่อเทียบผลที่ได้จากการทดลองกับผลจากการคำนวณ พบว่าในกรณีของโลหะนิกเกิล (111) ที่มีการดูดซับของอะตอมของออกซิเจนนั้น ออร์บิทัล $3d_{xz}$-$2p_x$ และออร์บิทัลไพที่ต้านการสร้างพันธะ $3d_{yz}$-$2p_y$ ทำให้เกิดสถานะอิเล็กทรอนิกส์บริเวณรอยต่อ และทำให้มีความเป็นแม่เหล็กที่มีทิศตั้งฉากกับผิวเพิ่มมากยิ่งขึ้น

สาขาวิชาฟิสิกส์ ลายมือชื่อนักศึกษา _____

ปีการศึกษา 2550 ลายมือชื่ออาจารย์ที่ปรึกษา _____

SOMCHAI CHUMPOLKULWONG : STUDY OF Ni(111) WITH OXYGEN ADSORPTION BY ANGLE-RESOLVED PHOTOEMISSION. THESIS ADVISOR: ASST. PROF. PRAYOON SONGSIRIRITTHIGUL, Ph.D. 170 PP.

SURFACE BAND STRUCTURE/AUGER/ANGLE-RESOLVED PHOTOEMISSION /NICKEL(111)

This thesis provides new information on the surface-energy-band structure of oxygen-adsorbed Ni(111) using angle-resolved photoemission spectroscopy. We have investigated surface electronic states of clean and oxygen-adsorbed Ni(111) surfaces using angle-resolved photoemission spectroscopy. In Ni(111) surface, c(2x2) and p(1x1) lattice structures appear in 0.51 ML and 0.88 ML oxygen-adsorbed surfaces, respectively. The energy dispersion of surface electronic states was obtained as the difference spectra between clean and oxygen-adsorbed Ni(111) surfaces. Comparing obtained spectra with molecular-orbital and energy-band calculations, it is shown that $3d_{xz}$-$2p_x$ and $3d_{yz}$-$2p_y$ anti-bonding π states are responsible for the electronic states at the interface and enhancement of the perpendicular magnetic anisotropy in the oxygen-adsorbed Ni(111) surfaces.

School of Physics Student's Signature_____

Academic Year 2007 Advisor's Signature_____

ACKNOWLEDGEMENTS

This thesis would not have been completed without assistance and guidance by many persons. I would like to thank:

• Asst. Prof. Dr. Prayoon Songsiriritthigul, my thesis advisor, for the invaluable advice and the unfailing support during the course of my studies at the School of Physics.

• Dr. Hideki Nakajima, manager of the BL4 beamline at the Siam Photon Laboratory, for his helping and training in the experiments. His ideas have been of vital importance for this thesis.

• Assoc. Prof. Dr. Sompong Thammathaworn, the dean of Institue of Science, Suranaree University of Technology, for his support in various respects.

• Assoc. Prof. Dr. Prapun Manyum, the head of School of Physics, Suranaree University of Technology, for his kind support.

• NSRC staff, especially engineers in the beamline division for their generous help.

• Udonthani Rajabhat University and National Synchrotron Research Center, for financial support.

• My father and my mother for their love, which cannot be expressed by any words on the earth.

Somchai Chumpolkulwong

CONTENTS

Page

ABSTRACT IN THAI I

ABSTRACT IN ENGLISH II

ACKNOWLEDGEMENTS III

CONTENTS IV

LIST OF TABLES VII

LIST OF FIGURES VIII

CHAPTER

I INTRODUCTION 1

1.1 Overview of the study 1

1.2 Motivation 11

1.3 Purpose of the research 14

II THEORETICAL BACKGROUND 15

2.1 Electronic Structure 15

2.2 Surface Electronic States 43

2.3 Photoemission Spectroscopy 49

2.3.1 Basic Principle 50

2.3.2 The Three-step Process 55

2.3.3 Cross Section 61

2.3.4 Electron Escape Depth 69

2.3.5 Measurement of EDC'S 71

CONTENTS (Continued)

Page

2.3.6 Angle-Resolved Photoemission Spectroscopy (ARPES) 78

2.3.7 Parity Determination 84

2.4 Computational electronic structure calculation 86

2.4.1 Cluster model 88

2.4.2 Band model 88

III EXPERIMENTAL 90

3.1 Experimental Instruments 90

3.1.1 Ultrahigh Vacuum System 93

3.1.2 Sample Holder and Manipulator 99

3.1.3 Low Energy Electron Diffraction (LEED) 99

3.1.4 Auger Electron Spectroscopy (AES) 104

3.1.5 Ion Gun 107

3.1.6 Electron Gun 110

3.1.7 Energy Analyzer 110

3.1.7.1 ARPES Analyzer 113

3.1.7.2 CLAM 114

3.1.8 Light Source: Synchrotron Radiation Source 115

3.2 Optical Beamline 120

3.3 Sample Preparation and Characterization 123

CONTENTS (Continued)

Page

IV RESULTS AND DISCUSSION 127

4.1 Experimental conditions 127

4.2 Electronic structure on oxygen adsorbed surface 130

4.3 Bulk energy bands 133

4.4 Interfacial energy bands 135

4.5 Surface energy bands 145

V CONCLUSION 151

REFERENCES 152

APPENDICES 160

APPENDIX A MOLECULAR ORBITAL CALCULATION 161

APPENDIX B ENERGY BAND CALCULATION 165

CURRICULUM VITAE 170

LIST OF TABLES

Table **Page**

2.1 Comparison of calculated μ_B and DOS (Connolly, 1967). 31

2.2 The energy levels at symmetry points as determined by Eberhardt and Plummer (1980) (units are electron volts). 42

2.3 Dipole selection rule using linear polarized light coming to single crystal surface. (Hermanson, 1977). 87

3.1 Pressure ranges used in vacuum (Thermo Vacuum Generators catalogue,www, 2006). 96

3.2 Specifications of the ARUPS10 analyzer. 113

3.3 Specifications of the CLAM2 analyzer. 114

3.4 Some of the machine parameters of the storages ring of the SPS. 119

3.5 Parameters of the gratings used in the BL-4 beamline. 121

LIST OF FIGURES

Figure **Page**

1.1 Schematic illustration of longitudinal and perpendicular HDD recordings. Hitachi Global Storage Technologies (www, 1999). 3

1.2 Magnetic anisotropy of films analyzed by Gradmann. ΔE is magnetic anisotropy energy in Eqation (1.1). Arrows represent magnetic moments (Gradmann, 1986). 5

1.3 The origin of shape anisotropy. Left figure shows longitudinal magnetization and right figure perpendicular magnetization. Arrows represent magnetic moments (Gradmann, 1986). 5

1.4 Two different PMA realized in films (Schulz and Babershke, 1994). 7

1.5 Dislocation and distortion of films on substrate. a_d and a_s represent lattice constant of substrate and film materials, respectively (Bruno and Renard, 1989). 7

1.6 Relationship between spin (m_{spin}) and orbital ($m_{orb.}$) moments of electron through spin-orbit interaction with respect to in-plane electron orbital in the film (Bruno, 1989). 9

1.7 (a) Layer-dependent magnetic anisotropy energy in Ni/Cu(001) (Uiberschke *et al*., 1999). (b) Thickness dependence of magnetic anisotropy energy in Ni/Cu (001). Lines represent theoretical results and markers experimental results. The temperature of samples (T) is shown in t = T/Tc (Hong *et al*., 2004). 9

LIST OF FIGURES (Continued)

Figure **Page**

1.8 Relationship between spin and orbital moments depending on film thickness and surface CO adsorption (Amemiya *et al*., 2005). 10

1.9 Magnetization curves in fcc nickel crystal (Seitz, 1987). 13

1.10 Mechanism of suppression of surface in-plane magnetic anisotropy. Small arrows represent electron behavior around electron orbit and large arrows orbital moments from small arrows. Spin moments favor to align with the same orientation as the orbital moments through spin-orbit interaction. Since gas atom makes out-of-plane orbital suppressed, in-plane magnetic anisotropy is reduced as illustrated in right-hand side (Bruno, 1989). 13

2.1 Four examples of the first Brillouin zone. (a) represents sc lattice, (b) fcc lattice, (c) bcc lattice and (d) hcp lattice. See text for various notations in each figure. 26

2.2 Three types of solids such as (a) Metal, (b) Semiconductor and (c) Insulator. Dots represent the occupation of the bands. 27

2.3 The calculated energy band structure of Ni (Moruzzi *et al*., 1978). 28

2.4 Comparison of the calculated density of state (DOS) curve with the measured energy distribution curve (EDC) for $Ce_2Cu_2Si_2$. Features in the DOS curve are shown by vertical bars and those in the EDC by arrows. The energy of excitation light is 35.5 eV (Soda *et al*., 1988). 29

LIST OF FIGURES (Continued)

Figure **Page**

2.5 Rigid band model for Ni and Cu. Hatched areas exhibit the bands filled with electrons (Wiwat Wongkokua, 2004). 31

2.6 Photoelectron EDC curves expected from DOS curve in Fig.2.5 (Wiwat Wongkokua, 2004). 32

2.7 Schematic illustration of the DOS curves of a ferromagnetic transition metal. Down-spin band is shifted from the up-spin band by the amount of the exchange energy, J. E_F : the Fermi level (Wiwat Wongkokua, 2004). 32

2.8 DOS of fcc Ni. Upper panel represent DOS for up-spin electrons, lower panel DOS for down-spin electrons and E_F Location of the Fermi level (Connolly, 1967). 36

2.9 DOS curves of paramagnetic Ni. Upper panel represents total DOS. Lower panel partial DOS for $d\varepsilon$ electrons (full line) and that for $d\gamma$ electrons (broken line), (Wakoh and Yamashita, 1964). 37

2.10 Panel (a) shows energy-band dispersion of Ni. Full line represents up-spin band (α) and broken line down-spin band (β). Numbers label the different bands. Panel (b) shows splitting of the 3d and 4s band by mixing (Wakoh, 1965). 38

2.11 Binding energy dependence of spin polarization of photoelectrons and the pertinent EDC. Upper curve depicts EDC and lower figure spin polarization (Kinoshita *et al*., 1993). 40

LIST OF FIGURES (Continued)

Figure **Page**

2.12 Empirical-band structure of nickel along some symmetry lines. The solid Lines indicate spin-up states, the dashed lines spin-down states. The experimental values are given by squares. The zero of energy is the experimental Fermi energy. The Fermi energy is E_F = 0.0548 eV (Weling and Callaway, 1982). 41

2.13 Electronic wave function in the surface region (Feuerbacher and Willis, 1976). 47

2.14 Schematic illustration of the surface energy bands (upper panels) and the surface eigenfunctions (lower panels). The projected bulk bands (hatched part) are shown for comparison. Left represent bulk state, middle surface state and right surface resonanace. The surface occurs at z = 0 (Feuerbacher and Willis, 1976). 48

2.15 Schematic diagram of spin and angle-resolved photoemission. This diagram is to show all the angular parameters. θ_i is the polar angle of photon incidence (incident angle). θ_e is the polar angle of photoelectron emission. ϕ_p and ϕ_e are azimuthal angles of light incidence and photoelectron emission, respectively. **p** is the momentum of the photoelectron. e_s (s-polarization) and e_p (p-polarization) are electric vector components of excitation light parallel and normal to the plane of incidence, respectively. ...53

LIST OF FIGURES (Continued)

Figure **Page**

2.16 Schematic illustration of the generation of photoelectrons. Excitation light with energy *hv* falls normally on the sample with the surface area, *S*. Photoelectrons generated in a small portion, *dz dS*, at *z* from the surface and progressing toward the direction (θ,ϕ) are considered. The sample surface is at z =0. Excitation light propagates toward $z > 0$. 63

2.17 Escape function versus ε_u/χ. ε_u : Kinetic energy; χ : Work function (Berglund and Spicer, 1964). 64

2.18 Atomic subshell photoionization cross section of Ni for 0-1500 eV(Yeh and Lindau, www, 1985). 65

2.19 Atomic subshell photoionization cross section of O for 0-1500 eV(Yeh and Lindau, www, 1985). 66

2.20 The three-step model of photoemission: (1) photoexcitation of electrons; (2) travel to the surface with concomitant production of secondary (shaded); (3) penetration through the surface (barrier) and escape into the vacuum (Hüfner, 1996). 70

2.21 The mean free path or escape depth of the electrons in solid. The open and close symbols represent experimental measurements and the dashed curve a calculation (Hüfner, 1996). 72

LIST OF FIGURES (Continued)

Figure **Page**

2.22 Relation between the kinetic energy of a photoelectron in vacuum and that in the field of an electrostatic energy analyzer. (I): Energy in a sample. (II): Energy in an experiment arrangement. The part of an electron lens is illustrated as retardation electrodes (Ishii, 1989). 76

2.23 Schematic illustration of photoelectron EDC, corresponding energy levels and the DOS curve. ε_f, ε_g, E_V and E_F are the energies for the final state, the initial state, vacuum level and Fermi level, respectively (Ishii, 1989). 77

2.24 Energy dispersion in the nearly free electron model for photoelectrons in ARPES. The right half represents the energy levels in a crystal. Curves illustrated by dots are energy-bands. Full lines are energy-band for the nearly free electron model. The left half represents the energy levels outside the crystal. **K** is a reciprocal lattice vector. hv: Photon energy. χ: work function. ε_u: Kinetic energy in the crystal. ε_k: Kinetic energy is a free space. E_F: The Fermi level. E_V: Vacuum level. V_0: Crystal potential (Ishii, 1989). ...83

2.25 Schematic illustration of the ARPES measurement geometries with polarized light. 87

2.26 Iteration process of DV- Xα method (Kresse and Hafner, 1993). 89

3.1 Schematic diagram of the new experimental station of the BL4 beamline at Siam Photon Laboratory (www, 2006). 92

LIST OF FIGURES (Continued)

Figure **Page**

3.2 Photoemission system at the experimental station of the BL-4 beamline. 94

3.3 Baking of the photoemission system by thermal insulators box. 97

3.4 Schematic diagram of the photoemission system. CLAM2 and ARUPS10 energy analyzers are the main instruments. 98

3.5 Schematic diagram of the sample holder and manipulator 100

3.6 A schematic plot of mean free path and electron energy(Quinn, 1962). 102

3.7 The energy distribution of emitted electrons from a target bombarded by electrons with primary energy E_p. (a) the true secondary electron peak; (b) Auger electrons shown in an exaggerated scale; (c) plasmon and interband losses; (d) elastic scattered electron (Rudburg, 1930). 102

3.8 Schematic diagram of rear view LEED setup. 105

3.9 Schematic energy level diagram illustrating the origin of the Auger effect. The Auger process in this figure is the KL_1L_3 process (Wild, 1981).....108

3.10 Auger spectrum from *LVV* Ni in differential spectrum. (a) The upper graph represents the graph with contamination. (b) The lower graph is the graph from the clean Ni(111) structure. 109

3.11 Simple sketch of ion gun. 111

3.12 Simple sketch of electron-gun. 112

3.13 Schematic diagram of CLAM2 with an electrostatic lens. 116

LIST OF FIGURES (Continued)

Figure **Page**

3.14 The magnet arrangement of the storage ring of the Siam Photon Source. 118

3.15 The optical layout of the BL-4 beamline at the Siam Photon Laboratory. 122

3.16 Auger spectra of clean surface p(1×1), 0.23 ML - p(2×2), 0.51 ML - c(2×2) and 0.88 ML - p(1×1) oxygen-adsorbed surfaces.....125

3.17 Surface atomic models for clean, p(2×2), c(2×2)-3 domains and p(1×1) oxygen adsorbed Ni(111) surfaces (Top view). 126

4.1 Schematic illustration of atomic and reciprocal structures on O/Ni(111) surfaces. Left figure shows atomic structure of c(2×2)-0.50 ML (top) and p(1×1)-1.00 ML (bottom) oxygen-adsorbed Ni(111) surfaces. Right figure represents LEED patterns on c(2×2) (top) and p(1×1) (bottom) oxygen-adsorbed Ni(111) surfaces. First Brillouin zones are also illustrated with corresponding irreducible representations in the inset of the illustration of LEED patterns. 129

4.2 Normal-emission spectra of p(1×1)-clean, c(2×2)-0.51 ML oxygen-adsorbed and p(1×1)-0.88 ML oxygen-adsorbed Ni(111) surfaces. Photon energy of 45 eV is incident on the sample at 60° and photoelectrons are measured in normal emission mode. 131

LIST OF FIGURES (Continued)

Figure **Page**

4.3 ARPES spectra dependent on photon energy on p(1×1)-clean Ni(111) surface. The spectra were measured at 60° of incident angle. Photon energy is varied in between 40 eV and 100 eV in normal-emission mode that corresponds to the bulk band along the Γ-Λ-L direction. Tick markers represent spectral features and dashed lines the spectral features shown in Fig. 4.2. 134

4.4 ARPES spectra of the clean Ni(111), c(2×2)-0.51 ML O/Ni(111) and p(1×1)-0.88 ML O/Ni(111) surfaces along the Γ-Σ-M direction. The geometry of ARPES measurement is also shown in the inset with incident angle of θ_i and emission angle of θ_e. Emission angles are indicated on the right-hand side of each spectrum. Tick makers in the normal-emission spectra correspond the spectral features in Fig. 4.2. 136

4.5 Subtracted ARPES spectra of the (a) c(2×2)-0.51 ML and (b) p(1×1)-0.88 ML O/Ni(111) surfaces from that of the clean Ni(111) surface shown in Fig. 4.3. A positive area is filled with black, while negative area is filled with gray. Tick markers in the normal-emission spectra correspond to the spectral features in Fig. 4.2. 137

LIST OF FIGURES (Continued)

Figure **Page**

4.6 First-principle energy-band dispersions calculation by using Vienna *ab-initio* simulation package (Adachi, Tsukada and Satoko, 1978). On the p(1×1)-clean Ni(111) and p(2×2)-0.25 ML O/Ni(111) surfaces. Left figure represents the energy band on the p(1×1)-clean Ni(111) surface and right figure the energy band on the p(2×2)-0.25 ML O/Ni(111) surface. Only majority-spin bands are shown in the figure. 139

4.7 DOS calculated by DV-Xα method (Kresse and Hafner, 1993). On the Ni cluster. Ni 3*d* partial DOS is also shown. Majority spin and minority spin bands are plotted in positive and negative ordinates, respectively. Cluster models are illustrated in the inset of each figure. 140

4.8 DOS calculated by DV-Xα method (Kresse and Hafner, 1993). On the O_4/Ni_9 cluster. Ni 3*d* and O 2*p* partial DOS are also shown. Majority spin and minority spin bands are plotted in positive and negative ordinates, respectively. Cluster models are illustrated in the inset of each figure. Large spheres represent Ni atom and small spheres O atom. Bottom figure shows a corresponding overlap population between Ni and O atoms. Positive and negative overlap populations indicate bonding and anti-bonding characters, respectively. 141

LIST OF FIGURES (Continued)

Figure **Page**

4.9 Polarization dependence of ARPES spectra on the clean and p(1×1)-0.88 ML O/Ni(111) surfaces. The polarization was selected by changing incident angle of linearly polarized light on the Ni(111) surface. The incident angles at 20° and 60° correspond to s-polarization (dashed lines) and sp-polarization (solid lines), respectively. Tick markers correspond to the spectral features shown in Fig. 4.2. 144

4.10 Surface energy-band map compared with spin-dependent surface energy-band calculation along the Γ-Λ-M direction in the surface BZ (Mittendorfer *et al*., 1999). M point in the surface BZ corresponds to a line at 1.46 $Å^{-1}$. Asterisks with error bars represent energy-band dispersions obtained by second-derivative process of c(2×2)-0.51 ML O/Ni(111) spectra. Open circles without error bars indicate energy-band dispersions on p(1×1)-0.88 ML O/Ni(111) surface. Thick lines are majority-spin bands and dashed lines minority-spin bands. 147

LIST OF FIGURES (Continued)

Figure **Page**

4.11 Surface energy-band map compared with spin-dependent surface quasi-particle band calculation along the Γ-Λ-M direction in the surface BZ (Grechnev *et al*., 2007). M point in the surface BZ corresponds to a line at 1.46 $Å^{-1}$. Left and right figures represent majority-spin and minority-spin bands with rainbow-colored scale, respectively. Asterisks with error bars represent energy-band dispersions obtained by second-derivative process of c(2×2)-0.51 ML O/Ni(111) spectra. Open circles without error bars indicate energy-band dispersions on p(1×1)-0.88 ML O/Ni(111) surface. 149

CHAPTER I

INTRODUCTION

1.1 Overview of the Study

This thesis describes the surface electronic structure of Ni(111) with and without oxygen adsorption measured by angle-resolved photoemission spectroscopy (ARPES) technique using synchrotron radiation. The observed ARPES spectra show an experimental proof of the enhancement of perpendicular magnetic anisotropy (PMA) on O/Ni surface. This result is important to not only understand the mechanism of PMA based on the electronic structure but also to develop advanced PMA recording media

Electronic and lattice structures are of importance to understand fundamental properties of materials. In particular, since the magnetism is due to electron spin and its interaction, a detailed analysis of the electronic structure gives an insight on the appearance of magnetic properties in materials.

Recent progress of ultra-high-vacuum (UHV) and film-growth techniques enables us to control material structures and its properties at surfaces and interfaces of films and multilayer. In particular, magnetic ultra-thin films have been studied actively because of their potential applications such as hard disc drive (HDD), magneto-optic disc (MO) and magnetic random-access memory (MRAM). A big challenge in this field of magnetic memories is the manipulation of magnetic properties including critical temperature, magnetic domain structure and magnetic

anisotropy. However, the underlying physics of these magnetic properties in low-dimensional system is still controversial.

Among the magnetic properties, the magnetic anisotropy plays a crucial role in the development of high-density recording HDD since the recording density is limited by the interaction between magnetic domains as shown in Fig. 1.1. A longitudinal recording used in a conventional HDD increases a magnetic fluctuation as the domain size decreases. A PMA recording developed recently suppresses the magnetic fluctuation since the magnetic interaction between magnetized domains is smaller than that in longitudinal recording. The PMA recording has a further advantage for reading and writing mechanism as shown in Fig. 1.1. The magnetic field from scanning head can be focused on the smaller domain than that in longitudinal recording. Although the conventional HDD stands highest recording density among the existing recording media, PMA recording HDD is expected to break through the current density limit.

The PMA of the magnetic ultra-thin films on various substrates depends on film thickness. For example, Co films on Pd(111), Pt(111) and Au(111) show PMA at thin films and in-plane magnetic anisotropy at thick films. In contrary, Ni films on Cu(001) show PMA at thick films and in-plane magnetic anisotropy at thin films (Schulz and Babershke, 1994). These controversial results were analyzed by the magnetic anisotropy energy (ΔE) consisting of shape ($-2\pi M_S^2$), bulk magneto-elastic (K_{2v}) and surface (K_{2s}) and interface (K_{2i}) magneto-crystalline anisotropies as follows.

$$\Delta E = -2\pi M_s^2 + K_{2v} + \left(K_{2s} + K_{2i}\right)/d \tag{1.1}$$

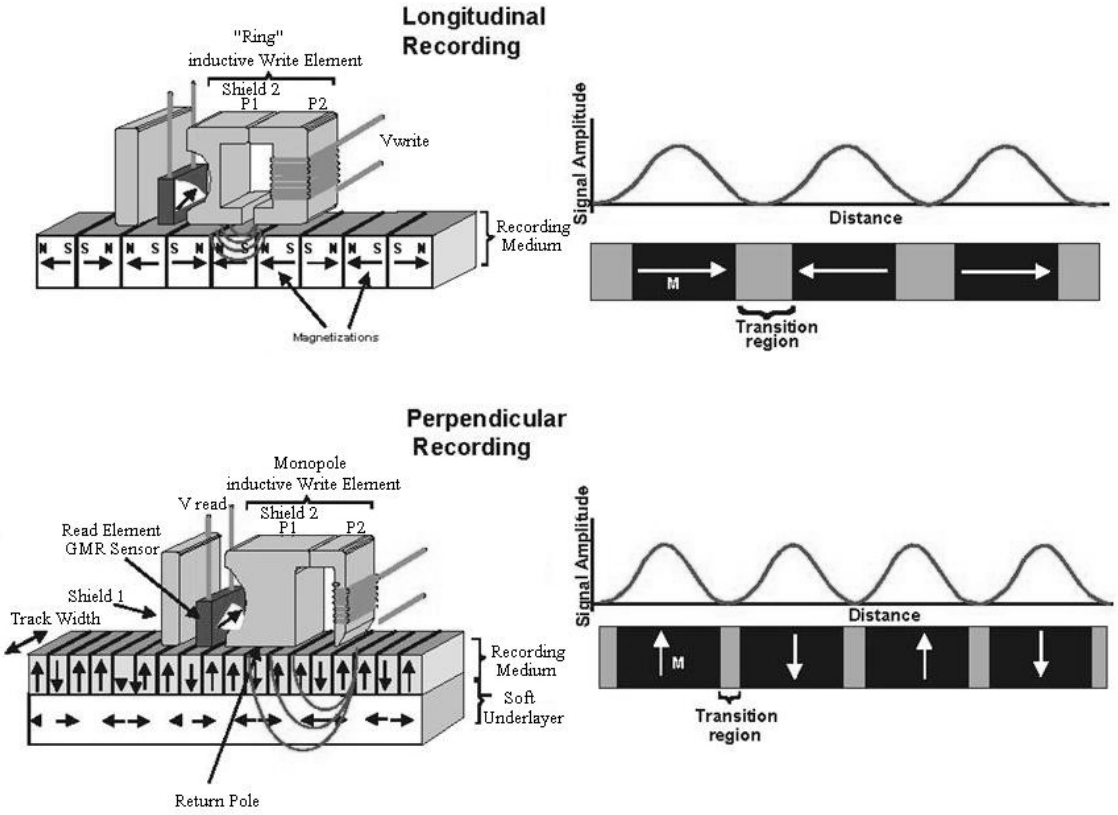

Fig. 1.1 Schematic illustration of longitudinal and perpendicular HDD recordings. Hitachi Global Storage Technologies (www, 1999).

Here d represents film thickness. A negative ΔE favors in-plane magnetic anisotropy, while a positive ΔE favors PMA in films as shown in Fig. 1.2. Shape anisotropy in the first term is due to magnetic dipole-dipole interaction between magnetic moments $\boldsymbol{\mu}_i$ and $\boldsymbol{\mu}_j$ with a distance of $\mathbf{r}_{ij}$ as follows

$$H_{\text{dip}} = \sum_{i \neq j} r_{ij}^{-3} \left[(\mu_i \cdot \mu_j) - \frac{3}{r_{ij}^2} (\mu_i \cdot \mathbf{r}_{ij})(\mu_j \cdot \mathbf{r}_{ij}) \right] \tag{1.2}$$

The second term of (1.2) shows that the dipole energy depends on the orientation of the magnetic moments with respect to its distance, while the summation over all lattice sites i, j in cubic symmetry and infinite-sized samples vanishes, namely isotropic. For finite-sized samples like ultra thin films, a continuum dipole density is commonly assumed. This leads to the energy using demagnetizing factor (N) times the magnetization (M).

$$E_{\text{dip}} = 2\pi (N_{\perp} - N_{\parallel}) M^2 \tag{1.3}$$

This energy is always negative in ultra thin films as illustrated in Fig. 1.3. Since the shape anisotropy is dominant in the equation (1.1), PMA do not realize in many films. Bulk-elastic anisotropy in the second term of equation (1.1) represents the contribution from easy magnetization axis of material. This term depends on the crystal structure of films including the effect from strain. The third term indicates surface and interface contributions to the magnetic anisotropy and it contribution increases as film thickness decreases. The surface anisotropy depends on the surface condition such as surface relaxation and gas adsorption, and the interface anisotropy depends on the lattice mismatching and dislocations between film and substrate.

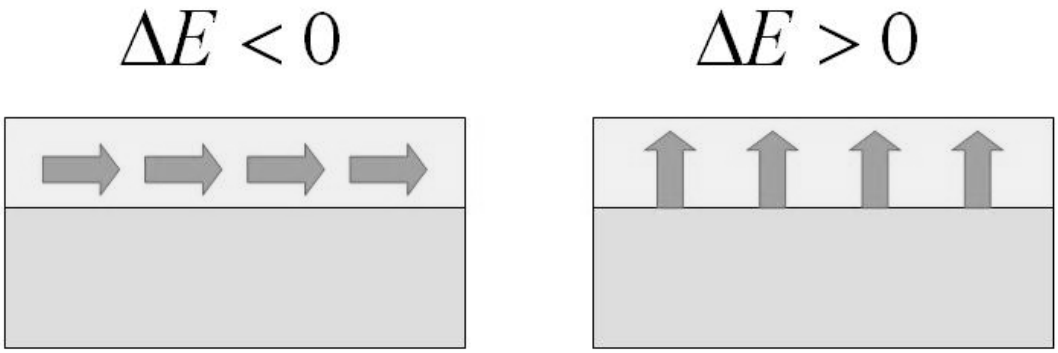

Fig. 1.2 Magnetic anisotropy of films analyzed by Gradmann. *ΔE* is magnetic anisotropy energy in Equation (1.1). Arrows represent magnetic moments (Gradmann, 1986).

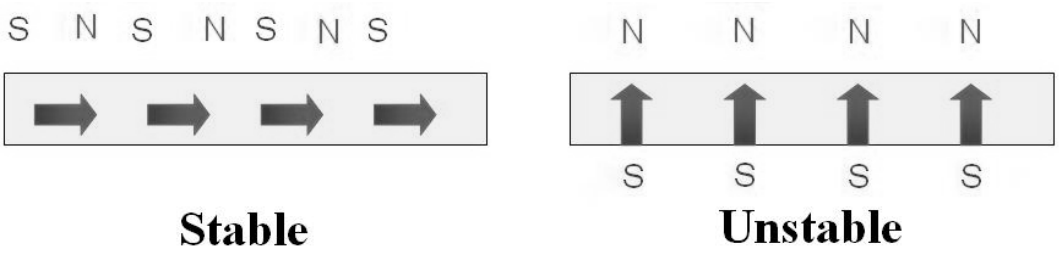

Fig. 1.3 The origin of shape anisotropy. Left figure shows longitudinal magnetization and right figure perpendicular magnetization. Arrows represent magnetic moments (Gradmann, 1986).

There are two combinations to explain PMA in two different systems as illustrated in Fig. 1.4. Co films on Pd(111), Pt(111) and Au(111) realize PMA due to negative interface anisotropy, while Ni films on Cu(001) show PMA due to negative bulk-elastic anisotropy (Schulz and Babershke, 1994). For the device application such as magnetic memories, the latter has a great advantage because of the manufacturing process of films in a commercial factory. Therefore, this thesis focus on PMA on Ni.

The electronic structure resulting PMA is mainly influenced by the lattice structure, especially in strained films as shown in Fig. 1.5 (Bruno and Renard, 1989). Since the nearest neighbor distance in bulk Cu is a_{Cu} = 2.55 Å and in Ni a_{Ni} = 2.49 Å, the pseudo-morphic growth of Ni on Cu(001) results in face centered tetragonal (fct) structure up to 15 monolayers (ML) and it relaxes into its original bulk fcc structure above 20 ML by producing dislocations to release the strain (Baberschke, 1996). On the other hands, the electronic structure plays a key role in PMA from a contribution of spin-orbit interaction.

The spin-orbit interaction combines electron spin with electron orbits showing various symmetries in the crystal field as illustrated in Fig. 1.6. These contributions have been investigated by both theoretical and experimental methods. Theoretical calculations revealed layer and thickness-dependent magnetic anisotropy energies in Ni/Cu(001) as shown in Figs. 1.7(a) and (b), respectively (Hong *et al*., 2004). According to depth-dependent x-ray magnetic circular dichroism (MCD) measurement, the relationship between spin and orbital moments was confirmed on Ni/Cu (001) as shown in Fig. 1.8 (Amemiya *et al.,* 2005).

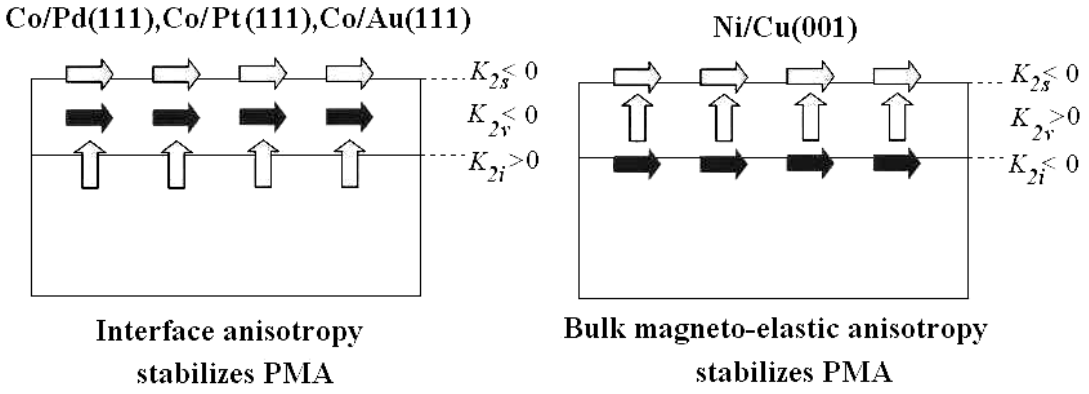

Fig. 1.4 Two different PMA realized in films (Schulz and Babershke, 1994).

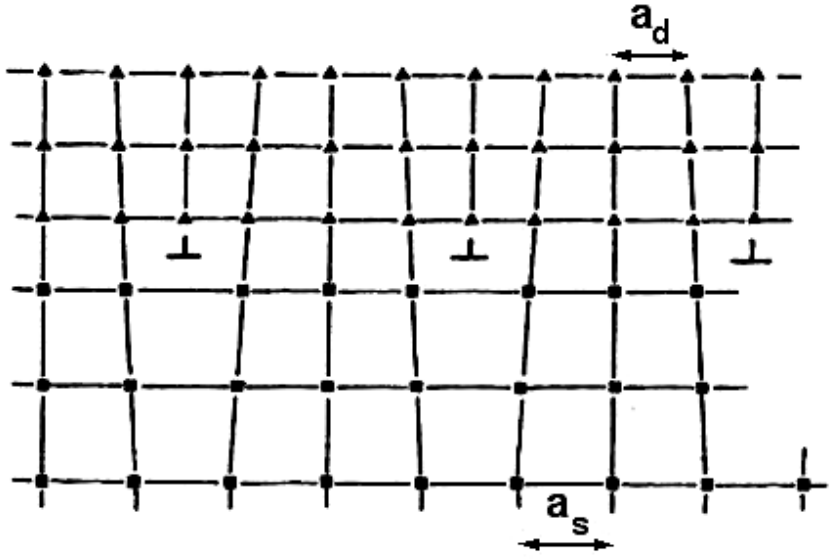

Fig. 1.5 Dislocation and distortion of films on substrate. a_d and a_s represent lattice constant of substrate and film materials, respectively (Bruno and Renard, 1989).

However, MCD does not provide detailed information on the surface and interface electronic structures responsible for PMA. In this sense, a deep understanding of PMA based on the electronic structure is essential. For this purpose, ARPES technique is suitable to investigate the energy-band structure at surface, film and interface. In order to avoid the effect from the lattice distortion of Ni films, the Ni surface is prepared in the bulk crystal oriented to [111] direction corresponding to easy magnetization axis as shown in Fig. 1.9 (Seitz, 1987). Since Ni(111) surface is closed pack structure, the surface relaxation and reconstruction effects are expected to be negligible even if the surface is adsorbed by gases. Therefore, Ni(111) is an ideal system to analyze the surface electronic structure responsible for PMA.

The surface condition is also an important factor to control the transition thickness from in-plane magnetic anisotropy to PMA. The surface magnetic anisotropy of Ni/Cu(001) favors in-plane magnetization making PMA suppressed. The in-plane surface magnetic anisotropy is reinforced by the typical surface electronic structure forming out-of-plane electron orbits due to no periodic potential to surface normal. If the surface electronic structure is suppressed by gas adsorption, PMA would be stabilized in the film less than the transition thickness as shown in Fig. 1.10. This was already confirmed by the surface magneto-optic Kerr effect (SMOKE) and MCD measurements using capped films and adsorption of gases such as O_2, H_2, NO, CO on Ni/Cu(001) as shown in Fig. 1.8 (Amemiya *et al.,* 2005). However, a detailed analysis of the energy-band and molecular-orbital structures on gas-adsorbed Ni surface is not examined yet. This is another reason to investigate Ni(111) surface electronic structure with and without gas adsorption as described above.

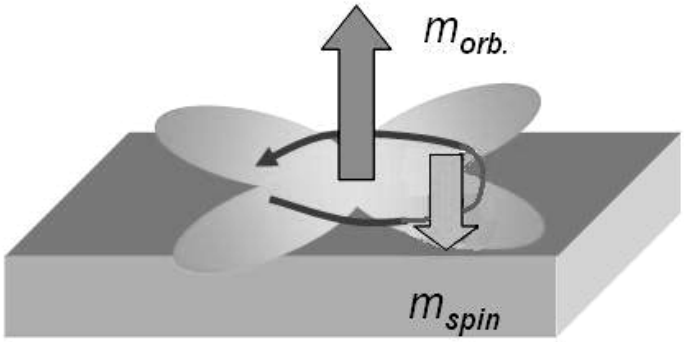

Fig. 1.6 Relationship between spin (m_{spin}) and orbital ($m_{orb.}$) moments of electron through spin-orbit interaction with respect to in-plane electron orbital in the film (Bruno, 1989).

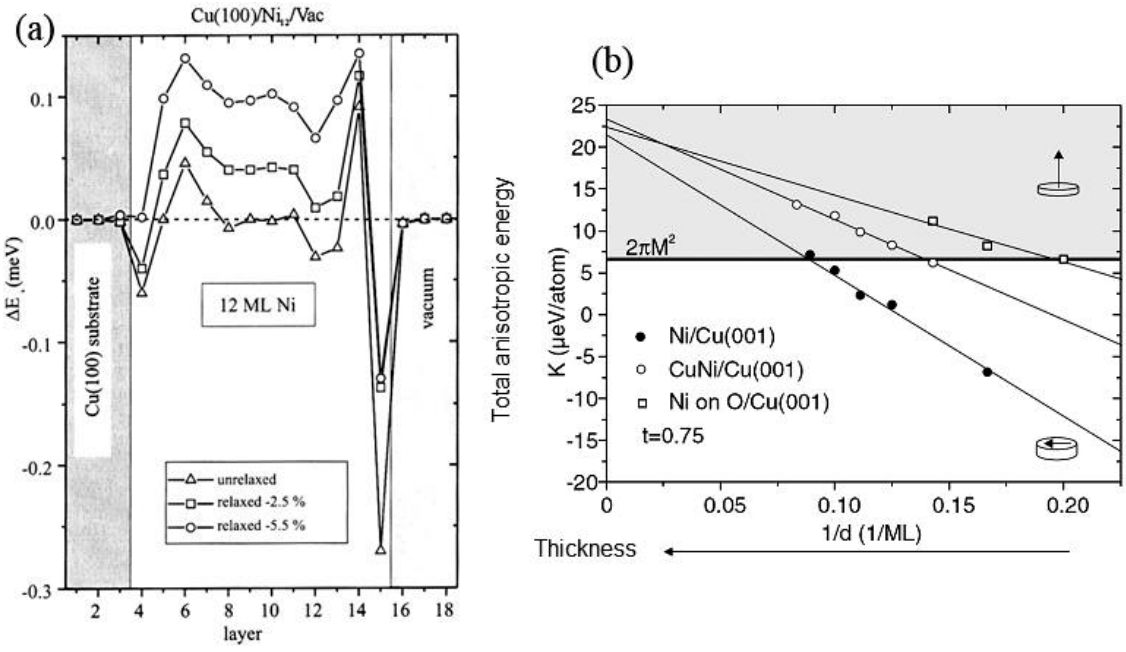

Fig. 1.7 (a) Layer-dependent magnetic anisotropy energy in Ni/Cu(001) (Uiberschke *et al*., 1999). (b) Thickness dependence of magnetic anisotropy energy in Ni/Cu (001). Lines represent theoretical results and markers experimental results. The temperature of samples (T) is shown in t = T/Tc (Hong *et al*., 2004).

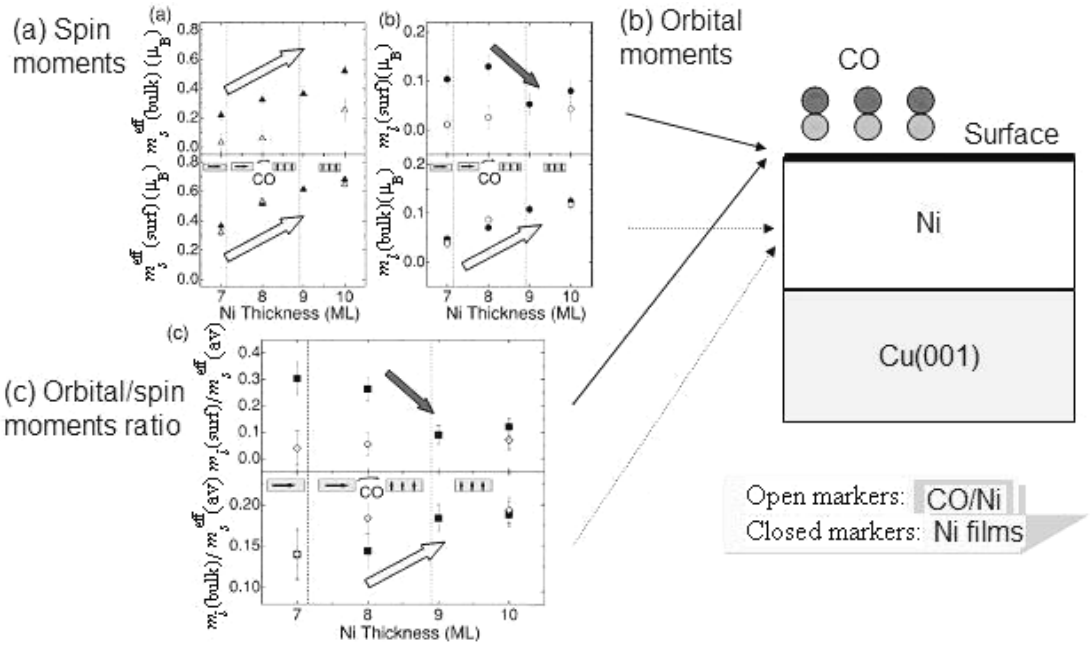

Fig. 1.8 Relationship between spin and orbital moments depending on film thickness and surface CO adsorption (Amemiya *et al*., 2005).

1.2 Motivations

In the last decades, magnetic anisotropy of transition-metal thin films is one of the most attractive research fields to develop high-density recording media (Schulz and Baberschke, 1994). Among a number of prototype, nickel films were found to be a valuable model because on a copper substrate, they show perpendicular magnetic anisotropy up to several dozen monolayers, which is more favorable for the device application than magnetic films with a few monolayers (Hong, *et al.,* 2004; Amemiya, *et al.,* 2005). It was also found that the transition thickness from in-plane magnetic anisotropy to perpendicular magnetic anisotropy was varied by surface condition of nickel films. However, the relationship between the surface condition and the transition of the magnetization direction of the film is not fully understood yet. Since in the device production process, surfaces of magnetic films are prepared not only as clean surfaces but also as gas-adsorbed surfaces, it is important to investigate the electronic structures of gas-adsorbed nickel surfaces by surface sensitive experimental techniques. For this purpose, we have measured the angle-resolved photoemission (ARPES) spectra of gas-adsorbed nickel surfaces as well as of clean surfaces to analyze the surface effects to the magnetic anisotropy. ARPES is a powerful tool to determine the energy-band structure responsible for the magnetism at the surface and interface, because photoemission phenomena of solids are quite surface sensitive. Since SR provides a clean source and a tunable energy, the combination of SR with ARPES gives us a great opportunity to investigate the surface and interface as well as bulk energy-band structures. The polarization of SR is also useful to determine the symmetry of wave function responsible for magnetic anisotropy. Molecular-orbital

and energy-band calculations were also used as a complementary approach to identify the surface and interface electronic structures.

We have chosen Ni(111) surface and oxygen as adsorbate since the former reveals a closed-pack structure despite large interlayer distance compared with those in others (Mittendorfer, Eichler and Hafner, 1999) and the latter is suitable for this kind of study due to a large electron affinity as well as a good vacuum compatibility. From the magnetic anisotropy point of view, Ni(111) surface is to be sensitive to adsorbate-induced reorientation of magnetization direction, since the easy magnetization axis of bulk nickel is along [111] direction (Seitz, 1987). In Ni(111) surface, a surface state is observed at 0.25 eV of binding energy and identified to be sp-like Λ_1 symmetry states (Himpsel and Eastman, 1978; Himpsel, Knapp and Eastman, 1979). The energy-band dispersion of unoccupied surface states was investigated using momentum-resolved inverse photoemission spectroscopy (Goldmann, Dose and Borstel, 1985). Several works on O/Ni and NiO surfaces were reported (Kilcoyne, Woodruff, Rowe and Gaylord, 1989; Thuler, Benbow and Hurych, 1983), so far. Experimental studies of c(2×2) O/Ni(111) structure revealed that the energy-band structures originated from O 2*p* states were in a good agreement with the result of an energy-band calculation (Kilcoyne, Woodruff, Rowe and Gaylord, 1989). However, detail information on the hybridization between Ni 3*d* and O 2*p* states and its relationship to the magnetic anisotropy is not fully understood.

This thesis work emphasize on the surface energy band structure of Ni(111) with and without oxygen adsorption. All experiments can be carried out in the ultra-high-vacuum condition by using experimental station at the BL-4 beamline at the Siam Photon Laboratory.

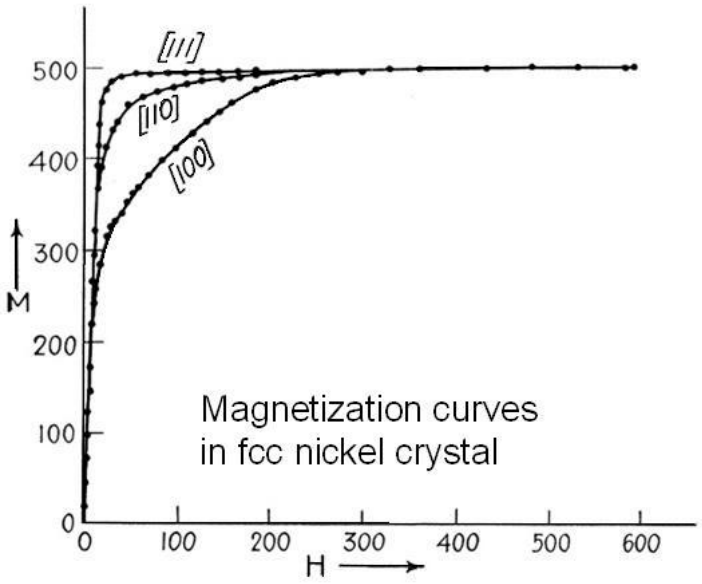

Fig. 1.9 Magnetization curves in fcc nickel crystal (Seitz, 1987).

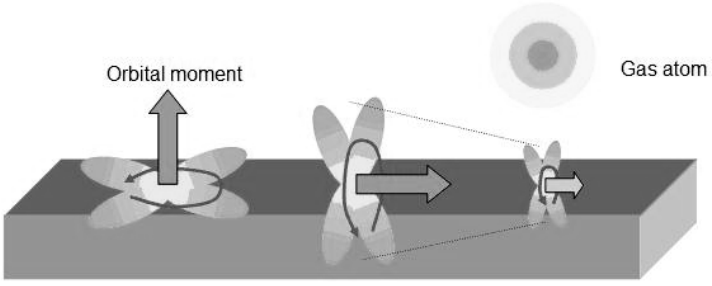

Fig. 1.10 Mechanism of suppression of surface in-plane magnetic anisotropy. Small arrows represent electron behavior around electron orbit and large arrows orbital moments from small arrows. Spin moments favor to align with the same orientation as the orbital moments through spin-orbit interaction. Since gas atom makes out-of-plane orbital suppressed, in-plane magnetic anisotropy is reduced as illustrated in right-hand side (Bruno, 1989).

1.3 Purpose of the Research

The goal of this thesis work is to provide surface magnetic information from surface electronic structure of O/Ni(111) surface by probing the surface energy-band structure. Especially, the energy band responsible for enhancement of PMA on O/Ni(111) surface will be identified by a combination between photoemission technique and theoretical calculations.

CHAPTER II

THEORETICAL BACKGROUND

This chapter provides the necessary background knowledge such as the electronic structures of both the bulk and surface, the theoretical aspects of photoemission spectroscopy (PES) and angle-resolved photoemission spectroscopy.

2.1 Electronic Structure

2.1.1 Energy Band Structure

In metallic materials, the electronic structure is described by the energy band picture in the first approximation. In other words, electrons in metals form energy bands as their energy states. Since the investigation of the electronic state of the Ni metal is the object of the research of this work, a brief description of the energy band is presented in this section.

Suppose there are N atoms in a solid. They are arranged symmetrically in this solid material. The symmetrical layout of atoms in a crystal is verified by the X-ray diffraction pattern that the crystal shows. An atom in a solid is ionized to a considerable extent and charged. Suppose the ion thus formed has a charge amount Ze where e is the charge of an electron. We call this ion as an ionic core. Then, obviously, Z is the valence number of the ionic core. Thus there are ZN electrons in the solid material we are dealing with. Here we do not count the electrons in the core. This is reasonable since core electrons do not contribute the solid state properties.

An electron sees the attractive potential from core ions as

$$V_1 = -\sum_j \frac{Ze^2}{|\mathbf{r}_i - \mathbf{R}_j|} \tag{2.1}$$

Here, $\mathbf{r}_i$ and $\mathbf{R}_j$ represent the locations of *i*-th electron and *j*-th core, respectively. The repulsive potential acts between a pair of electrons as

$$V_2 = \sum_{i \neq j} \frac{e^2}{|\mathbf{r}_i - \mathbf{r}_j|} \tag{2.2}$$

In addition to these, there is repulsive potential working between ion cores as

$$V_3 = \sum_{i \neq j} \frac{Z^2 e^2}{|\mathbf{R}_i - \mathbf{R}_j|} \tag{2.3}$$

If we ignore the magnetic interaction arising from the interactions between magnetic moments, the hamiltonian describing the electronic state is written as

$$H = -\frac{\hbar^2}{2m}\sum_i \nabla_i^2 - \sum_{i,j} \frac{Ze^2}{|\mathbf{r}_i - \mathbf{R}_j|} + \sum_{i \neq j} \frac{e^2}{|\mathbf{r}_i - \mathbf{r}_j|} + \sum_{i \neq j} \frac{Z^2 e^2}{|\mathbf{R}_i - \mathbf{R}_j|} \tag{2.4}$$

In some cases, the spin-orbit interaction is not negligible. This introduces extra complexity. The number of the resulting energy bands increases. The hamiltonian equation is handled by the relativistic treatment. In Ni whose atomic potential is large, the relativistic effect is not negligible. In spite of the neglect of the relativistic effect, however, the essence of the energy band treatment is unchanged.

If we can solve the hamiltonian equation

$$H\Phi(\mathbf{r}_1\mathbf{r}_2.....\mathbf{r}_{ZN}) = E\Phi(\mathbf{r}_1\mathbf{r}_2.....\mathbf{r}_{ZN}) \tag{2.5}$$

We obtain the eigen energy and eigenfunction describing the state of the solid. Among four terms in equation (2.4), the last terms, V_3 as in equation (2.3), does not contain the coordinate of an electron. Then it is a constant term in the electronic hamiltonian, which will be omitted from the hamiltonian. The result is given as

$$H = -\frac{\hbar^2}{2m}\sum_i \nabla_i^2 - \sum_{i,j}\frac{Ze^2}{|\mathbf{r}_i - \mathbf{R}_j|} + \sum_{i\neq j}\frac{e^2}{|\mathbf{r}_i - \mathbf{r}_j|} \tag{2.6}$$

It is impossible to solve the hamiltonian equation (2.5) using equation (2.6), since it contains the electron-electron interaction term in equation (2.2).

One method to simplify the hamiltonian equation and derive the one electron equation formally is the Hartree-Fock approximation in which the one electron equation is formed in a self-consistent way (Kittel, 1963). In the Hartree-Fock approximation, the many electron state $F(\mathbf{r}_1\ \mathbf{r}_2.....\ \mathbf{r}_{ZN})$ is approximated as the Slater determinant of one electron function $F_n(\mathbf{r}_i)$. By inserting the Slater determinant to the many electron hamiltonian equation in the manner that the energy expectation value is calculated as

$$E = \langle F|H|F\rangle \tag{2.7}$$

Thus, using equation (2.7), the relation that a one-electron function must satisfy is written down. In this equation many electron interaction parts are involved. If we formally integrate those parts in the self-consistent way, we can obtain the one electron solution in the scheme of the self-consistent approximation.

It is out of the scope of this thesis to describe the Hartree-Fock approximation in a quantitative way. However, it should be pointed out that carrying out this calculation in our system does not make sense. This is because we have *ZN* electrons, and therefore, we have to solve *ZN* variables simultaneous equations. Note $NZ \sim 10^{24}$. The Hartree-Fock approximation is useful in a small electron number system like an isolated atom, a molecule or an equivalent system.

Instead, we will make a drastically simplifying assumption. Let us start with one electron. The interactions between electrons are so complicated that the electron sees only the average field. In this average field, the potential acting on one electron is a function of the coordinate of this electron. All other contributions are averaged out. In the approximation like this, the core ion is regarded as being singly charged. (*Z*-1) charges are screened by electrons around the core to give resultant single charge. Thus, the total number of electron to consider is *N*. we define the one-electron eigenfunction and the one-electron energy eigenvalue as $f(\mathbf{r}_i)$ and $\varepsilon^{(i)}$, respectively.

It is easy to prove that the solution of the equation (2.5) is given as

$$F = f(\mathbf{r}_1) f(\mathbf{r}_2) \ldots\ldots f(\mathbf{r}_N) \tag{2.8}$$

$$E = \varepsilon^{(1)} + \varepsilon^{(2)} + \ldots\ldots + \varepsilon^{(N)} \tag{2.9}$$

Here, the one-electron Schrödinger eigenequation is given as

$$H_i f(\mathbf{r}_i) = \varepsilon^{(i)} f(\mathbf{r}_i) \tag{2.10}$$

In what follows, just for convenience, we omit subscript and superscript in treating the one-electron Schrödinger eigenequation as

$$H\psi(\mathbf{r}) = \varepsilon\psi(\mathbf{r}) \tag{2.11}$$

The one-electron potential, $V(\mathbf{r})$, is symmetric in space. The symmetry is the same as that of the crystal, *i.e*., the solid material we are dealing with. The crystal has both rotational and translational symmetry. Thus the hamiltonian has the similar symmetry. We ignore the mathematical rigorousness and try to understand the situation from observation and intuition. Mathematically, what we describe below are proved by using the group theory.

In this way, there are many atoms in a crystal and accordingly there are many electrons. Electrons feel attractive forces from ionic cores and repulsive forces from other electrons. Such interactions are complicated in principle but they can be simplified to one particle potential. This is because there are very many particles and the complicated interactions are averaged. Suppose one electron in a crystal sees such an averaged potential, $V(\mathbf{r})$, has the translational symmetry, for which **r** is the electron coordinate. Then $V(\mathbf{r})$ has the periodicity of the crystal lattice, since the atoms are aligned regularly in crystal. So we have

$$V(\mathbf{r}+\mathbf{a}) = V(\mathbf{r}) \tag{2.12}$$

Here, **a** is a lattice translation vector. According to Bloch's theorem (Ziman, 1963; Kittel, 1963), the solution of the hamiltonian eigenequation under the condition given in equation (2.12) has the form expressed as

$$\psi_{nk}(\mathbf{r}) = \exp(i\mathbf{k}\mathbf{r})u_{nk}(\mathbf{r}) \tag{2.13}$$

$$u_{nk}(\mathbf{r}+\mathbf{L}) = u_{nk}(\mathbf{r}) \tag{2.14}$$

Here n is a quantum number assigning the state and **k** is the electron wave vector, defined as

$$\begin{aligned} k_x &= \frac{\pi}{2a_x}\left(\frac{l}{N}\right) \\ k_y &= \frac{\pi}{2a_y}\left(\frac{m}{N}\right) \\ k_z &= \frac{\pi}{2a_z}\left(\frac{n}{N}\right) \end{aligned} \tag{2.15}$$

Here a_x ,a_y, a_z are lattice constants; l, m ,n are integers in the range

$$-N \le l, m, n \le N \tag{2.16}$$

The function described as equation (2.13) is called the Bloch function. The energy eigenvalues of equation (2.11) and the corresponding eigenfunctions are obtained by solving equation (2.11) in the unit cell, since the eigenfunction, $u_{\mathbf{nk}}(\mathbf{r})$, is translationally symmetric as shown in equation (2.14).

Here, it should be remarked that the energy eigenvalues, ε, of equation (2.13) is a periodic function of **k** as

$$\varepsilon(\mathrm{k}+\mathrm{K}) = \varepsilon(\mathrm{k}) \tag{2.17}$$

The relation (2.17) is based on the reason that the reciprocal lattice space is periodic with a period of the reciprocal lattice vector, **K**. Thus, the corresponding eigenstate must be translationally symmetric in the **k** space with the reciprocal lattice vector, **K**. This is written as

$$f_{\mathrm{nk}}(\mathrm{r}) = f_{\mathrm{nk+K}}(\mathrm{r}) \tag{2.18}$$

Since the energy eigenvalues are periodic, we have to consider the energy states only in the unit cell. The unit cell is defined as

$$-\frac{\mathrm{K}}{2} \le \mathbf{k} \le \frac{\mathrm{K}}{2} \tag{2.19}$$

The condition (2.19) is more definitely expressed as

$$\begin{aligned} -\frac{\pi}{a_x} \le k_x \le \frac{\pi}{a_x} \\ -\frac{\pi}{a_y} \le k_y \le \frac{\pi}{a_y} \\ -\frac{\pi}{a_z} \le k_z \le \frac{\pi}{a_z} \end{aligned} \tag{2.20}$$

The space confined in the region specified by relation (2.20) is called the Brillouin zone or the first Brillouin zone. Since the Brillouin zone is the unit cell, the Wigner-Seiz (WS) cell, of the reciprocal lattice space, the border is depicted easily. Four examples are shown in Fig. 2.1. They are for sc, fcc, bcc and hcp lattices. It should be remarked that the reciprocal lattice of the fcc lattice has the bcc structure and that of the bcc lattice has the fcc structure.

The WS cell has the center of symmetry. Therefore the WS cell has the rotational and mirror reflection symmetry. In solving the eigenequations, the use of the results provided by the group theory is quite helpful. It is out of scope of this thesis to touch the group theory, since it is found in many textbooks (Heine, 1960; Kittel, 1963; Slater, 1965). Suppose that there are some special points, axes or mirror planes in the WS cell of the reciprocal lattice space and the rotation or mirror operation with respect to them do not change the reciprocal lattice space. The assemblies of such operations form the groups. The operations commutate with the

hamiltonian and the dimension of the irreducible representation presents the degeneracy states of the eigenstate.

The solutions of the eigenequation (2.11) in the WS cell are degenerated in general. However, for **k** not at the symmetric points, all the degeneracy is lifted. In this case, the number of the basis functions necessary to solve eigenequation by the perturbation approach is appreciable and solving the eigenequation is almost impossible. The state degeneracy reduces the number of the basis functions. Thus, in the energy band treatment, the only energy eigenvalues with **k** is such symmetric points or lines are calculated. In recent years, the computer capacity and the speed of processing have greatly enhanced. This has increased the dimension, the size, of the secular equation to be solved to a great extent and the accuracy of the calculated results. However, the situation that the calculation is made for highly symmetric points or lines has not been changed.

Examples of such symmetric points and lines are indicated with various notations in Fig. 2.1. The notation was first used by Bouchaert, Smoluchowski and Wigner (1936) and the notation has been employed by many authors. Now it is the world standard. The notation that they used to specify the energy bands have also been widely used. It appears that the characters used in the notation have no specific meaning. They are just the signs to distinguish different points or lines. In practice, the notation such as Γ_1, Γ_2, Γ_{12}, Γ_{25},…,Δ_1, Δ_2,…,X_1, X_2,…,Λ_1, Λ_2,…,Σ_1, Σ_2,…etc. are used instead of ε_1, ε_2, ε_3,…

The energy eigenvalues are the function of **k** that varies continuously. Accordingly $\varepsilon_n(\mathbf{k})$ varies continuously. Here n distinguishes the different eigenstate as $u_{n\mathbf{k}}(\mathbf{r})$. For **k** in the Brillouin zone, $\varepsilon_n(\mathbf{k})$ is confined in the range as

$$\varepsilon_n^{(\min)} \le \varepsilon_n(\mathbf{k}) \le \varepsilon_n^{(\max)} \tag{2.21}$$

For a given n, $\varepsilon_n(\mathbf{k})$ distributes in a range with a width. Thus, $\varepsilon_n(\mathbf{k})$ is referred to as the energy-band. The dependence of E on $\mathbf{k}$ is called the energy dispersion. Drawing the energy dispersion curves for various n is called the energy-band mapping. The Bloch function extends over the whole crystal. It represents the state where the electron is itinerant. Therefore it includes implicitly the state where the charge is fluctuating at a lattice site.

The energy bands, which can be occupied by electrons, are called the allowed bands and the energy regions between adjacent allowed bands are called the forbidden bands. The size of the forbidden band, the shortest distance between two adjacent bands is called the band gap. Electrons occupy an energy band successively from the low energy to the high energy. $2N$ electrons can occupy one band. One $\mathbf{k}$ site is occupied by two electrons with opposite spins. If a band is filled with electrons completely and the bands above it are completely empty, the corresponding material is an insulator. If a band filled up to a certain level and the level above its is empty, the material is a metal. The level, up to which in a band is filled with electrons, is called the Fermi level. In an insulator, the Fermi level is located halfway in the band gap. If the band gap of a material is very narrow, the material is a semiconductor. The location of the Fermi level of a semiconductor in the band gap is decided by the locations of the levels of impurities such as donors and acceptors. The locations of the Fermi levels in three types of the solids are shown in Fig. 2.2. In the figure, small dots represent the situation that the energy band is occupied. Panel (a) is for a metal, (b) for a semiconductor and (c) for an insulator.

Practical calculation to obtain $\varepsilon(\mathbf{k})$ is carried out by various approximations. Some approximations are very useful in understanding the essence of the energy band, although they are not used in the practical calculations. They are the nearly free electron approximation, the Bloch function is formed by plane waves with different wave vectors and the tight binding approximation, we take electrons to be bound at lattice sites and approximate the Bloch function with linear combination of atomic orbitals. Instead better approximations are used. They are the orthogonalized plane wave (OPW) method, the augmented plane wave (APW), and the Green function method. In order to introduce the effect of the correlation interaction, a method called the α method has been proposed and used. Recently, the method called the density functional calculation is quite popular. Recent advance in computer calculation technique and upgrading of computers have made it possible to calculate the energy-bands and associated Bloch functions with high accuracy. It is not practical to introduce the calculation methods here, since the description must be lengthy and we do not deal with the theoretical calculation. Instead, we introduce the reported results of the energy-band calculation in what follows. In Fig. 2.3, the energy band dispersion curves of Ni calculated by Moruzzi *et al.* are presented (Moruzzi, Janak and Williams, 1978).

An important quantity describing the energy states of a solid material is the density of states (DOS). DOS indicates the number of states in the unit energy range. This is obtained by summing up all possible state number in the energy range from ε to $\varepsilon + d\varepsilon$ and the dividing the sum by $d\varepsilon$ as

$$D(\varepsilon)d\varepsilon = \frac{2}{(2\pi)^3}\iint_{\varepsilon}^{\varepsilon + d\varepsilon} d\mathbf{k} \tag{2.22}$$

$$= \frac{2}{(2\pi)^3} \int\int_{\varepsilon} \frac{dS}{|\nabla_{\mathbf{k}} \varepsilon(\mathbf{k})|} \tag{2.23}$$

Where $d(\varepsilon)$ is DOS. The surface integration is carried out on the surface of a given constant energy. When the energy band calculation is made, DOS is calculated numerically using equation (2.22). An example of calculated DOS curve as compared with measured photoelectron energy distribution curve for CeCu2Si2 is shown in Fig. 2.4 (Soda, Mori, Onuki, Komatsubara and Ishii, 1988).

Before we proceed further, we briefly mention the rigid band model, which is quite useful to understand the DOS curves of Ni qualitatively. If electrons are not widely spread from a lattice site, the width of the energy dispersion is narrow. Therefore, localized electron forms a narrow and high density band. If electron wave functions are widely spread in a crystal, they form a broad weak band. The 3*d* electrons are localized and 4*s* electrons are shown schematically in top panel of Fig. 2.5. We fill the bands with electrons from the bottom. In Ni, the 3*d* band is not completely filled up; one electron is missing from the 3*d* band. Thus the Fermi level occurs in the 3*d* band as illustrated in the middle panel. In Cu, the 3*d* band is filled up as $3d^{10}$. Then the electrons are filling up the empty 4*s* band above 3*d* band as illustrated in the bottom panel. Therefore the Fermi level occurs in the 4*s* level. Suppose the photoelectron EDC's are reflecting the DOS curve. The expected EDC's are as shown in Fig. 2.6. This is what is experimentally observed. In the argument given above, the DOS curve is fixed and the number of electrons is changed to predict the actually observed spectra. This model is called the rigid band model.

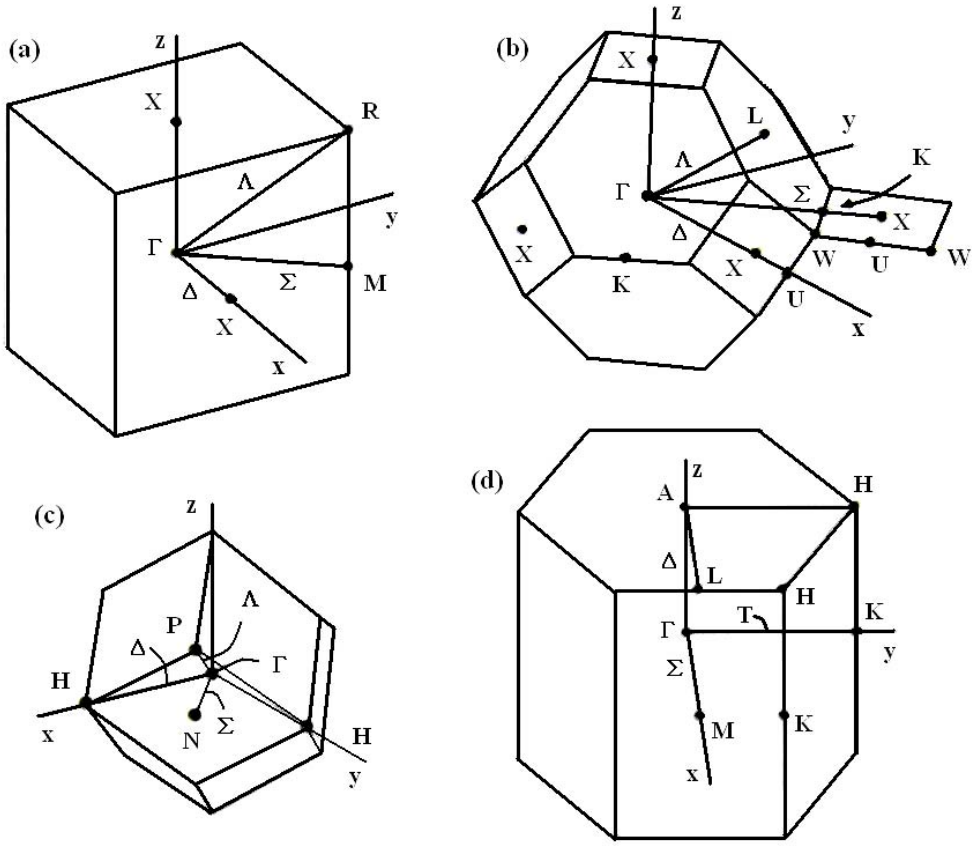

Fig. 2.1 Four examples of the first Brillouin zone. (a) represents sc lattice, (b) fcc lattice, (c) bcc lattice and (d) hcp lattice. See text for various notations in each figure.

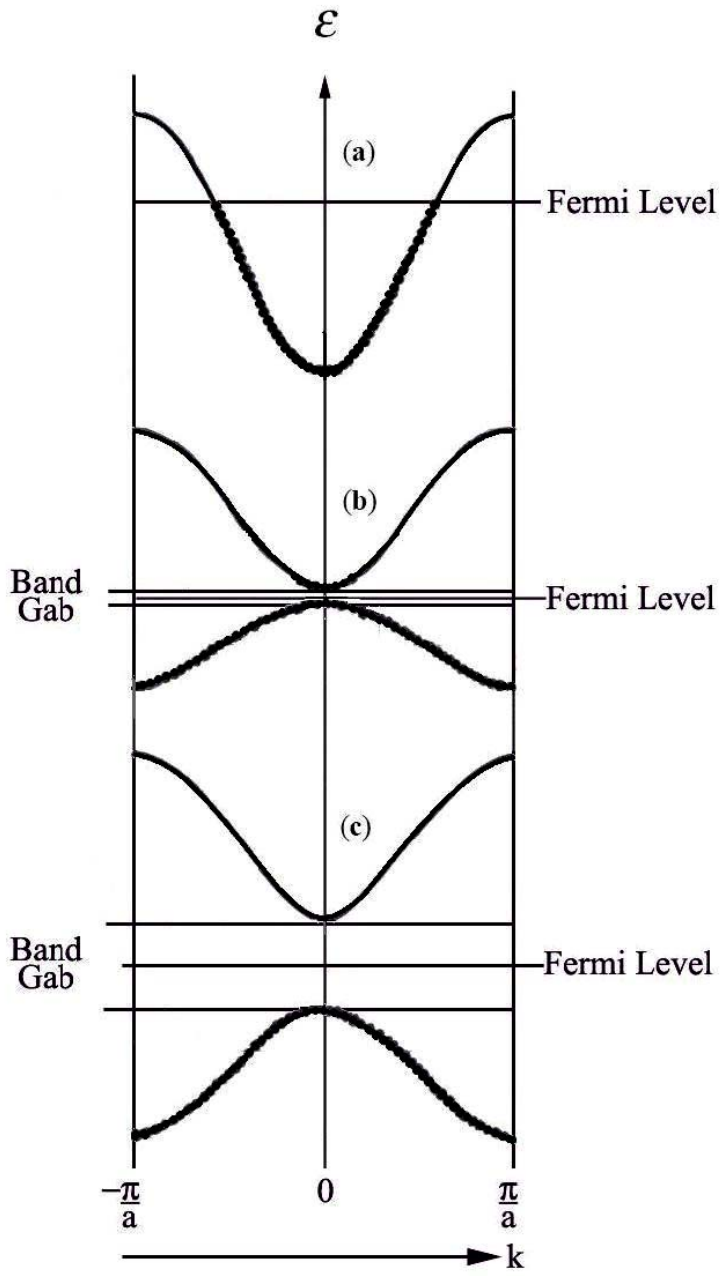

Fig. 2.2 Three types of solids such as (a) Metal, (b) Semiconductor and (c) Insulator. Dots represent the occupation of the bands.

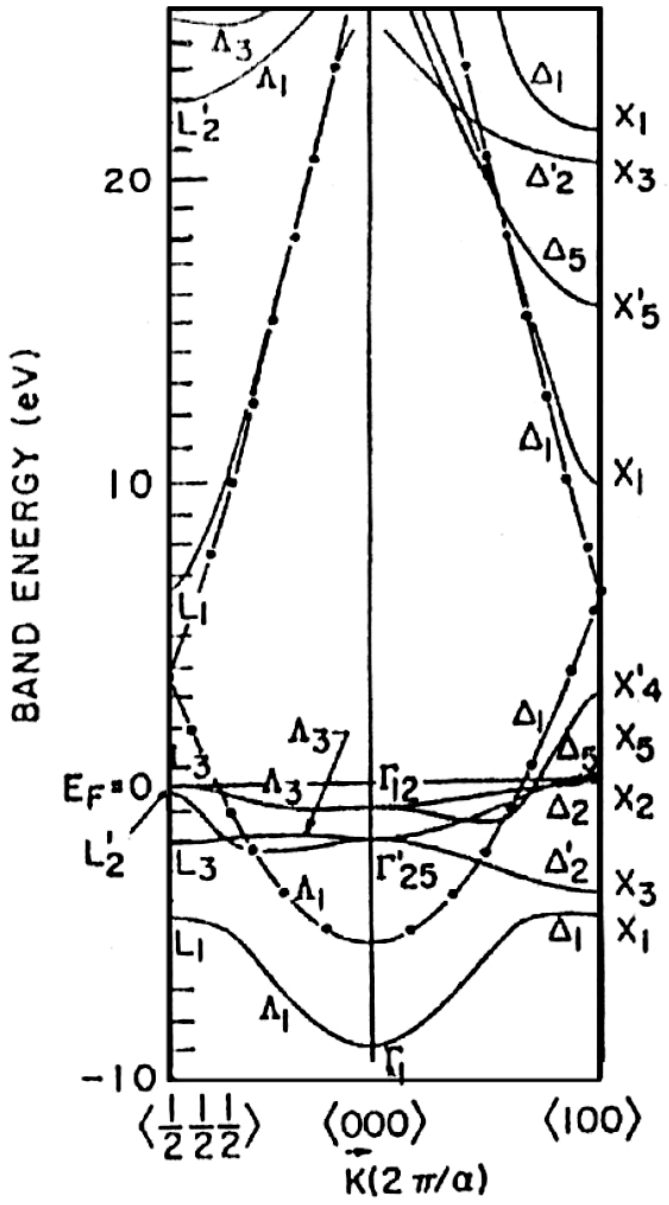

Fig. 2.3 The calculated energy band structure of Ni (Moruzzi *et al*., 1978).

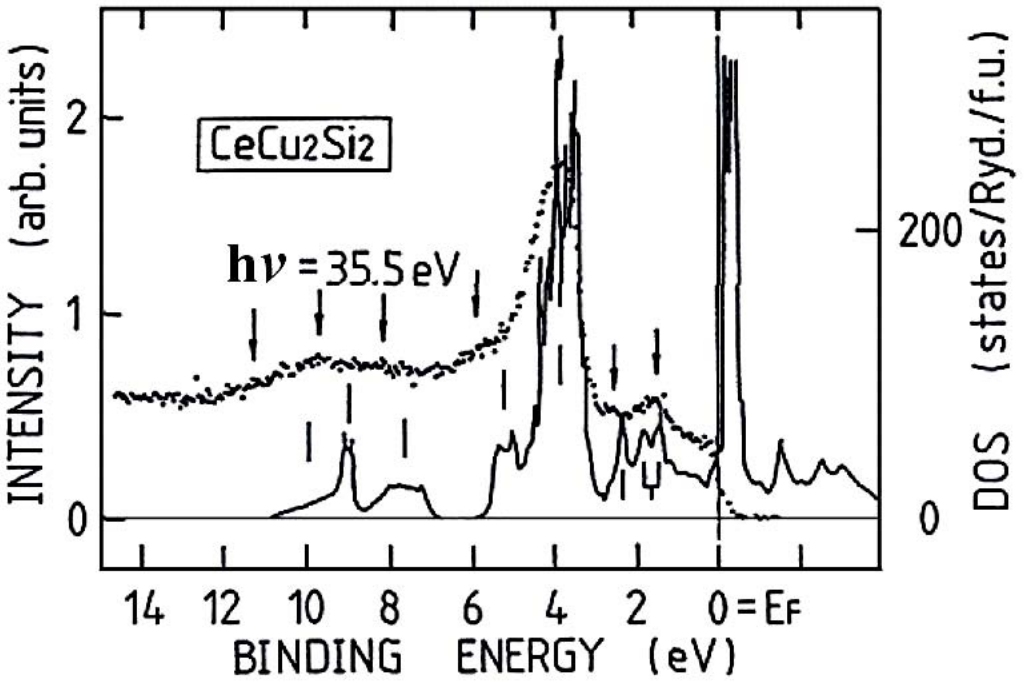

Fig. 2.4 Comparison of the calculated density of state (DOS) curve with the measured energy distribution curve (EDC) for $Ce_2Cu_2Si_2$. Features in the DOS curve are shown by vertical bars and those in the EDC by arrows. The energy of excitation light is 35.5 eV (Soda *et al*., 1988).

On the basis of the energy-band picture, the deviation is explicable by the exchange splitting between the up-spin band and the down-spin band. This is shown in Fig. 2.7. The magnetic moment is determined by the difference of the number of down-spin electrons and that of up-spin electrons. The value of J is independent of μ_B . Thus resulting net number of the difference take values different from an integer and then the concomitant magnetic moments can take values different from integral multiples of μ_B . In ferromagnetic Ni, the number of down-spin electrons is 4.4 on average and the number of up-spin electron is 5.

When we make alloys by adding Cu to Ni, the vacancies in the down-spin band are filled with electrons and the 3d band is completely filled up in the alloy with 40% Ni and 60% Cu. Experimentally, ferromagnetism is found to disappear at this concentration. In this explanation, the rigid band model used in that the addition of Cu to Ni does not change the shape of the DOS curve. The rigid bands split by the exchange interaction are schematically shown in Fig. 2.7.

Connolly (1967) calculated DOS of nickel. He calculated the potential within the frame work of the unrestricted Hartree-Fock scheme in which the exchange terms were approximated by a local potential. The augmented-plane-wave was used to find the eigen values of the approximated Hamiltonian. The results are in Fig. 2.9. The data is old but by the middle of 1960's, the accuracy of the energy-band calculation increased tremendously. This is because the advanced calculation methods had been invented on one hand and the progress of computer technology had been quite fast. If we find the $V(\mathbf{r})$, the energy-band is calculated without any serious difficulty. The self-consistency was achieved by iteration.

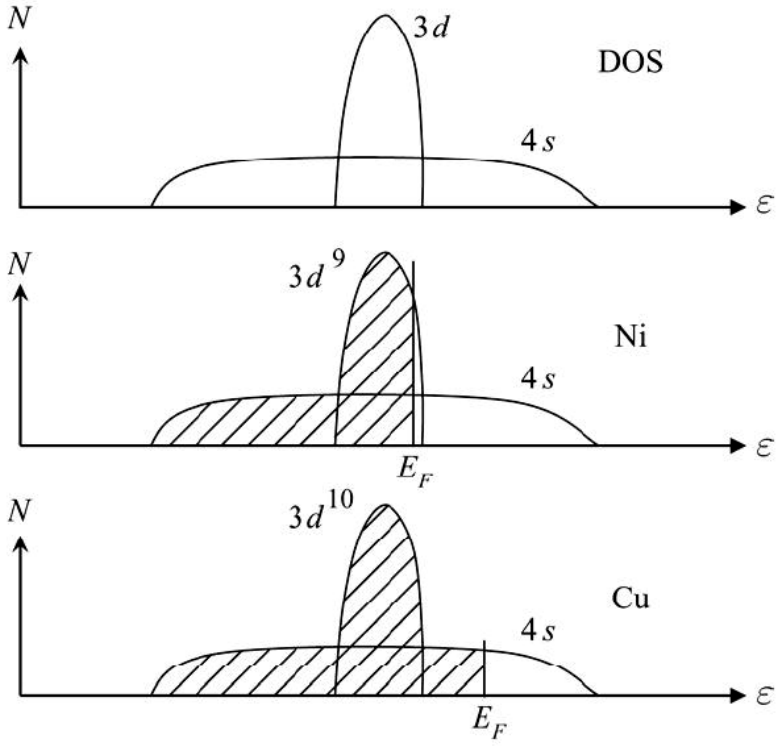

Fig. 2.5 Rigid band model for Ni and Cu. Hatched areas exhibit the bands filled with electrons (Wiwat Wongkokua, 2004).

Table 2.1 Comparison of calculated μ_B and DOS (Connolly, 1967).

	Calculated Values	Experiment Values
μ_B /atom	0.62	0.606
DOS at the Fermi Surface	2.7	3.1

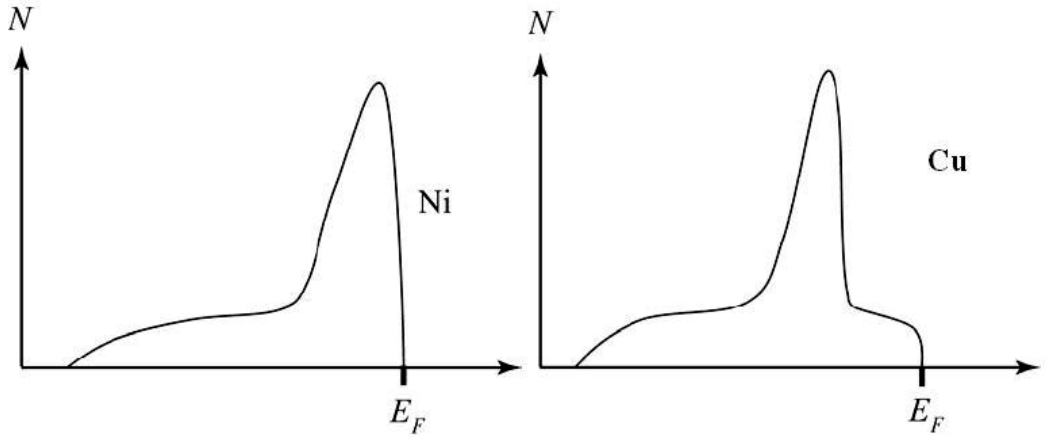

Fig. 2.6 Photoelectron EDC curves expected from DOS curve in Fig.2.5 (Wiwat Wongkokua, 2004).

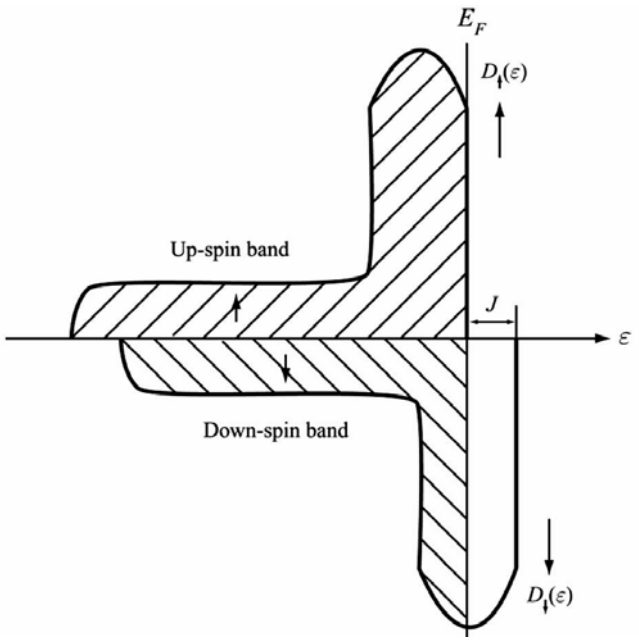

Fig. 2.7 Schematic illustration of the DOS curves of a ferromagnetic transition metal. Down-spin band is shifted from the up-spin band by the amount of the exchange energy, J. E_F : the Fermi level (Wiwat Wongkokua, 2004).

In practice, averaged free-electron exchange potential $V_{ex} = -6(6\rho/8\pi)^{1/3}$, was used, where ρ is the electron density. Connolly determined $V(\mathbf{r})$ completely self-consistently including the exchange interaction. No parameter obtained experimentally was used concerning magnetization. Calculated μ_B and DOS are shown in Table 2.1. Agreement between the calculated results and the experimental data is good.

The calculation of the energy-bands were also made by Wakoh and Yamashita (1964) as well as Weling and Callaway (1982). Basic features are almost the same as those shown in Fig. 2.8. The DOS curves show the aspect that the 3*d* band with the high DOS is embedded in the wide sp band. The 3d level splits into two sublevels called *dε* and *dγ* in the cubic electrostatic field. Thus, it is interesting to find the contributions of the two kinds of electrons. The results of such calculations are shown in Fig. 2.9. In the figure, the upper panel shows the total DOS curve. The lower panel shows the partial DOS curves for *d*ε and *d*γ electrons. The calculation was carried out for the paramagnetic state. Therefore the DOS curve shown in the upper panel is to be compared with of the DOS curves shown in Fig. 2.8 or the average of the two by letting *J* to be zero. The agreement between data shown in Fig. 2.8 and Fig. 2.9 is good. From the partial DOS curves shown in the lower panel, we know that the first peak and the third peak arise from the *dε* states. In the same way, we understand that the second peak arises from the *dγ* state We have mentioned that the narrow 3*d* band is embedded in the wide weak 4*s* band. The calculated DOS curves support this view. It is interesting to see this situation in the calculated energy-band-dispersion curves. Fig. 2.10 shows the energy-band-dispersion curves, the *E*-**k** curves, calculated by Connolly (1967). The panel (a) on the left-hand side shows the *E*-**k** curves. Full lines

correspond to the up-spin band. Broken lines correspond to the down-spin band. They are designated with Greek letters α and β, respectively. The numbers given to the curves distinguish different bands. The bands are calculated in the panel (a), the bands indicated with arrows are similar to the curves of wave-vector dependence of the energy of a free electron as

$$E(\mathbf{k}) = \frac{\hbar^2}{2m}\mathbf{k}^2 \tag{2.24}$$

The parabolic curve has a large gap slightly above the center of the Δ axis. The occurrence of the gap is interpreted as illustrated in the panel (b) on the right hand side. The gap is caused by the splitting of the parabolic band. In the panel (b), the parts of the *E*-**k** curves not split are shown with broken lines. The longer parabola arises from nearly-free electrons and the band with less dispersion in the 3*d* band. The 3*d* band crosses the nearly-free-electron band and degenerate state occurs at the cross point. Because of the perturbation due to the electron-electron interaction the degeneracy is lifted and the band splits. The 3*d* bands have dispersion larger than those expected from the atomic energy levels. This is caused by the mixing of the nearly-free-electron states.

From the consideration described above the 3*d* band of Ni must show the spin polarization. Experimentally, spin-resolved photoemission data shows the existence of the exchange split 3*d* band (Kisker, Schröder, Gudat and Campagna, 1985). Prior to the experiments by Kisker *et al*.; Himpsel, Knapp and Eastman (1979); Eberhardt and Plummer (1980) measured the energy-band dispersion of Ni by high resolution angle-resolved photoemission, *E*-**k** curves, and found the fine structure of EDC's in which

some peaks exist in pairs. An important way for investigating the validity of the energy-band calculation is to compare the calculated results with those of photoemission. The partial DOS with specific orbital symmetry, $\rho_l(\varepsilon_B)$ is proportional to the photoemission intensity, $N(\varepsilon_B)$ as

$$N(\varepsilon_B) = A\rho_l(\varepsilon_B) \tag{2.25}$$

Here, A is constant. Also the binding energy of a peak observed in angle-resolved EDC represents the energy difference between two different energy-bands.

The validity of the results of the energy-band calculation is judged by comparing them with the experimentally decide E-**k** curves. As will be described in Section of photoemission, the dispersion curves are obtained by angle-resolved photoemission. As is obvious, the overall width of the 3*d* band shown in Fig. 2.10 does not coincide with the result of the angle-resolved photoemission. The width of the 3*d* band in Fig. 2.10 is about 4.3 eV which is about 4.1 times as large as that found in Fig. 2.11. Although old energy-band calculation can explains the shape of the Fermi surface obtained by the measurements of de Haas-van Alfen effects, it cannot explain the overall energy-band shape.

We find from comparison of the calculated DOS curves with photoelectron EDC's that the calculated DOS curves do not agree with the photoemission data. The DOS curves in Fig. 2.8 and Fig. 2.9 indicate that the width of the main 3*d* band is about 4.5 eV. The width of the 3*d* band shown in Fig. 2.11 is much narrower than this value (Kinoshita *et al*., 1993). The data shown in Fig. 2.11 is for the spin polarization of the two-hole-bound-state. It should be remarked that the fine structures as found in Fig. 2.8

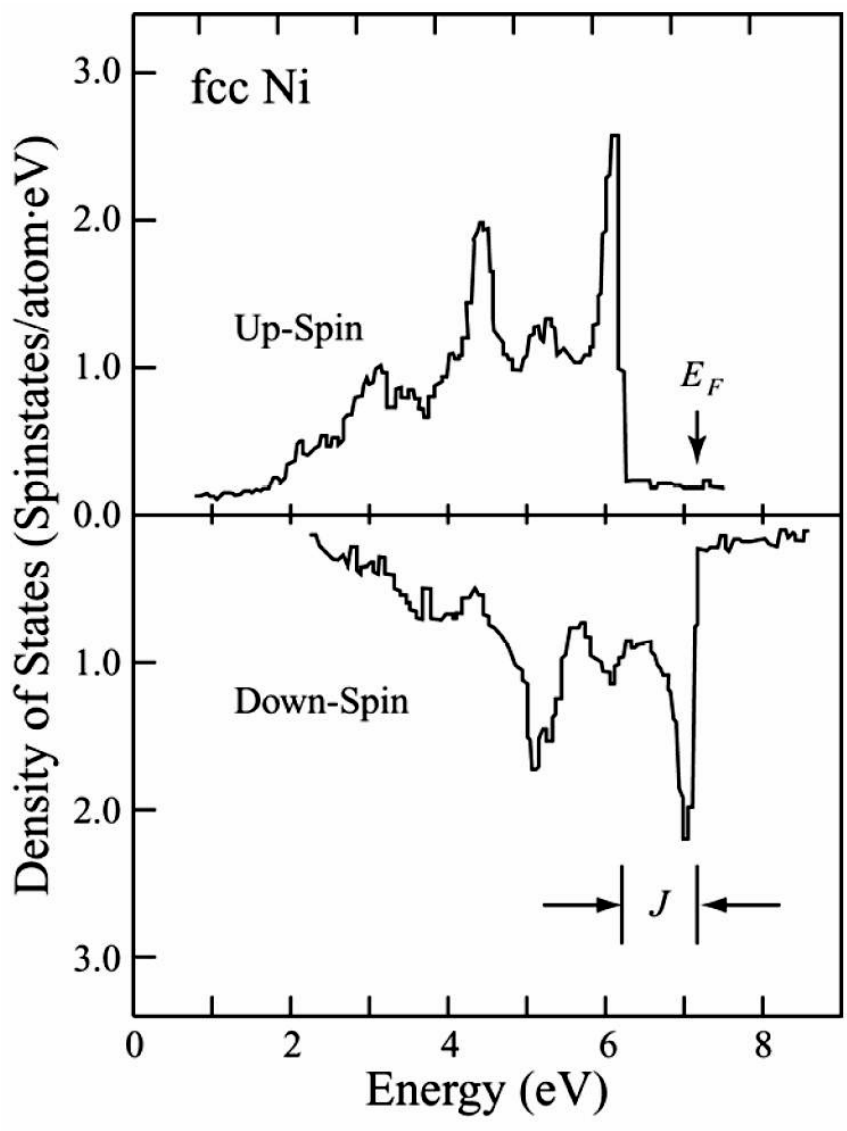

Fig. 2.8 DOS of fcc Ni. Upper panel represent DOS for up-spin electrons, lower panel DOS for down-spin electrons and E_F Location of the Fermi level (Connolly, 1967).

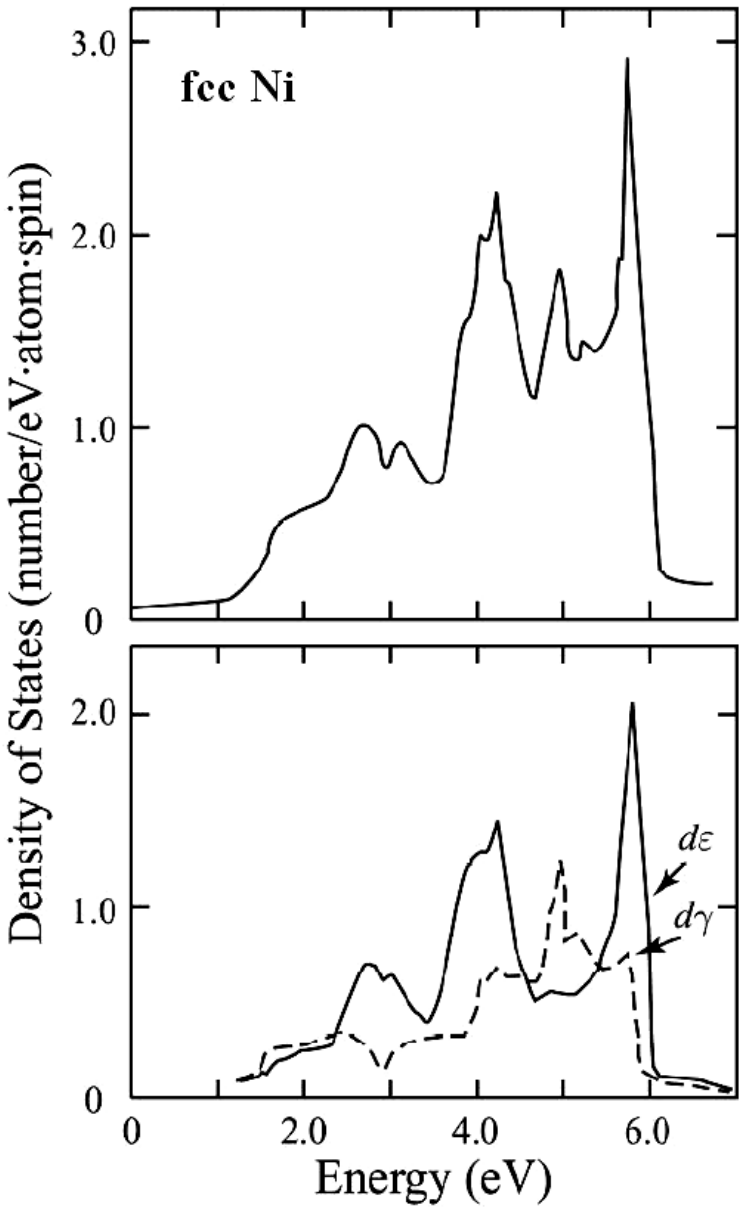

Fig. 2.9 DOS curves of paramagnetic Ni. Upper panel represents total DOS. Lower panel partial DOS for *dε* electrons (full line) and that for *dγ* electrons (broken line), (Wakoh and Yamashita, 1964).

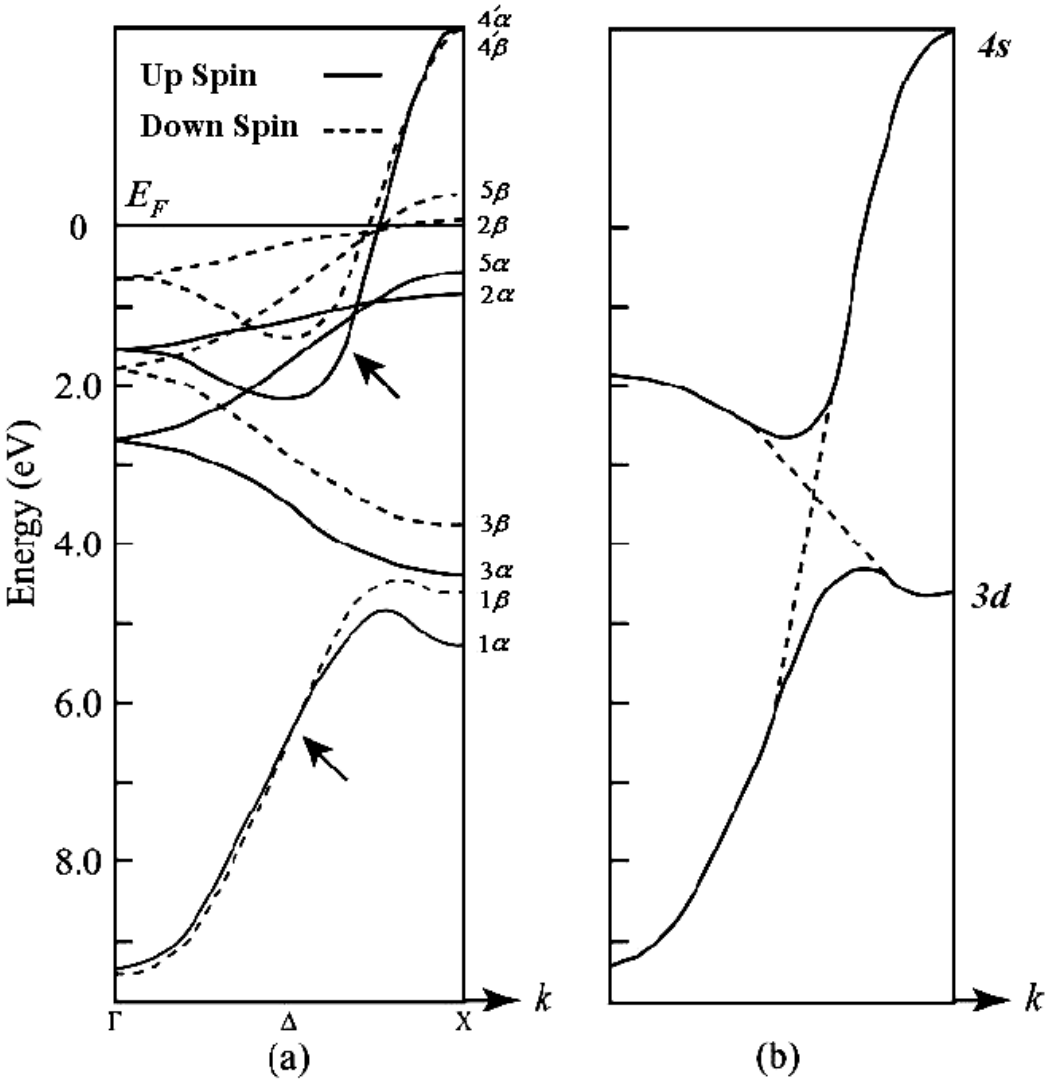

Fig. 2.10 Panel (a) shows energy-band dispersion of Ni. Full line represents up-spin band (α) and broken line down-spin band (β). Numbers label the different bands. Panel (b) shows splitting of the 3*d* and 4*s* band by mixing (Wakoh, 1965).

and Fig. 2.9 are not found. One of the reasons for this is the low experimental resolution, phonon broadening, and lifetime broadening. However, it is plausible some intrinsic discrepancy exists. The width of the experimental main 3*d* band is about 2 eV. A broad band occurring at 6.3 eV is caused by the two-hole-bound state which does not appear in the energy-band.

The calculation of energy was made for good symmetry points in the Brillouin zone. The 20 energy values were to be calculated. The numbers of parameters appearing in the expressions were altogether 14. In practice, the parameters were determined, so that the calculated energy fit the various values of energy at the symmetry points in the Brillouin zone obtained by angle-resolved photoemission. The energy values used are tabulated in Table 2.2 (Eberhardt and Plummer, 1980). The energy values for other **k** values were determined by the interpolation method. The functions expressing the dispersion of the energy band are analytically expressed using trigonometric functions and the spherical Bessel functions. The results are those shown in Fig. 2.12.

The energy-bands illustrated in Fig. 2.12 were calculated so that they reflect the results of angle-resolved photoemission. This is quite evident that the calculated bands reproduce the results of the angle-resolved photoemission. In addition to the photoemission data, the calculated energy-bands should agree with the shape of the Fermi surface obtained by de Haas-van Alphen experiments. For realizing this, the parameters used in the calculation were slightly adjusted further. The results of the calculation reproduced the experimental shape of the Fermi surface.

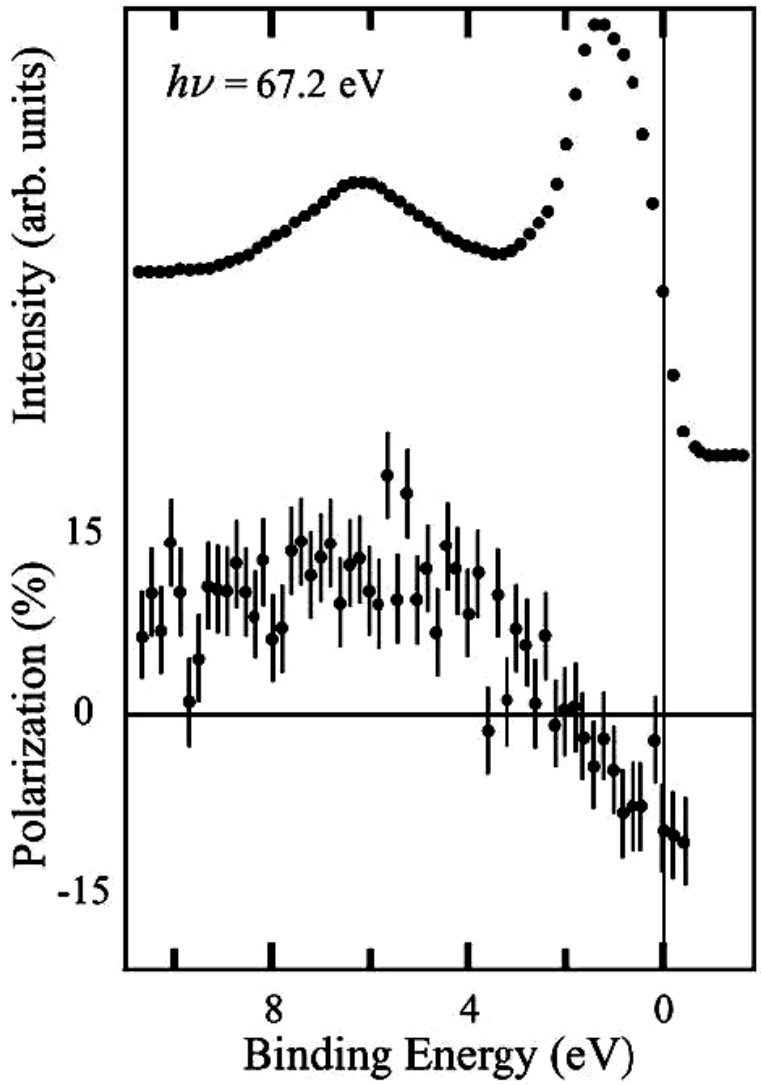

Fig. 2.11 Binding energy dependence of spin polarization of photoelectrons and the pertinent EDC. Upper curve depicts EDC and lower figure spin polarization (Kinoshita *et al.*, 1993).

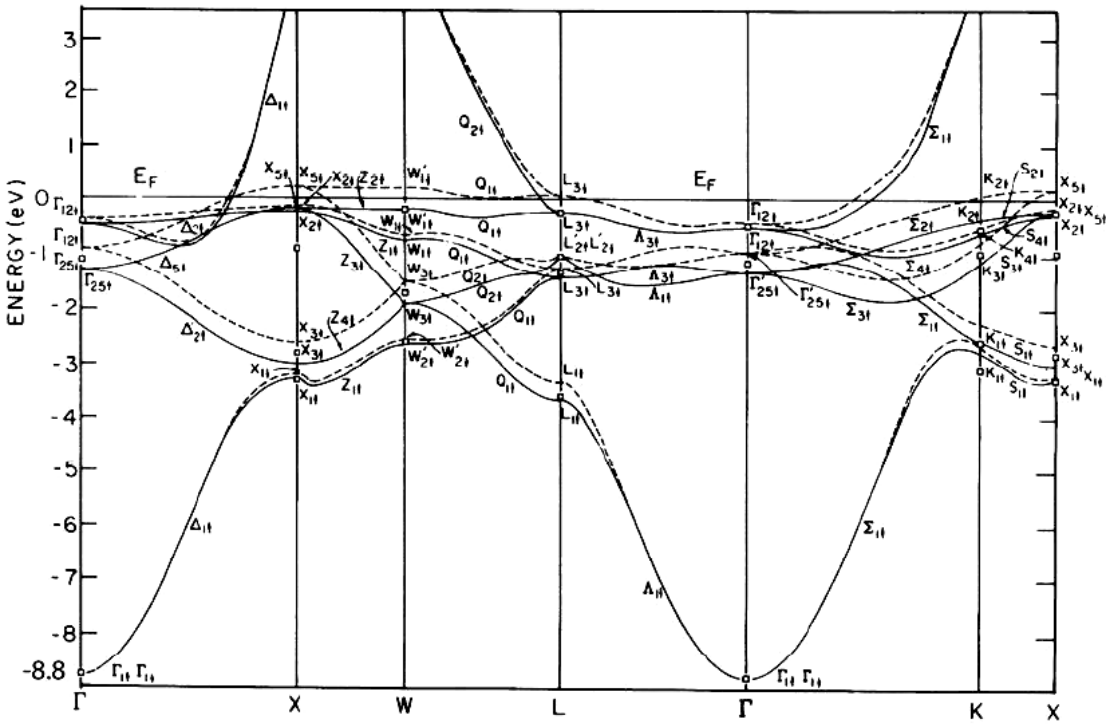

Fig. 2.12 Empirical-band structure of nickel along some symmetry lines. The solid Lines indicate spin-up states, the dashed lines spin-down states. The experimental values are given by squares. The zero of energy is the experimental Fermi energy. The Fermi energy is E_F = 0.0548 eV (Weling and Callaway, 1982).

Table 2.2 The energy levels at symmetry points as determined by Eberhardt and Plummer (1980) (units are electron volts).

	Experiment[a]		Theory[c]		Fit[d]	
Symmetry	average[b]	spin-up	average	average	spin-up	spin-down
Γ_1	-8.8±0.2		-8.93		-8.8	-8.8
$\Gamma_{25'}$	-1.1±0.2		-2.04		-1.3	-0.9
Γ_{12}	-0.4±0.1		-0.92		-0.45	-0.35
X_1	-3.3±0.2		-4.31	-3.24	-3.2789	-3.1942
X_3	-2.8±0.2		-3.81		-3.0000	-2.6000
X_2	-0.85±0.1		-0.81	-0.16*	-0.2079	-0.1079
X_5			0.02	0.05	-0.1500	0.2500
L_1	-3.6±0.2		-4.63	-3.50	-3.6638	-3.3413
L_{31}	-1.3±0.1		-2.07		-1.4035	-1.2045
$L_{2'}$	-1.0±0.2		-0.40		-1.0000	-1.0000
L_{32}		-0.2±0.1	-0.17	-0.06*	-0.2016	0.0994
$W_{2'}$	-2.6±0.2		-3.59		-2.6422	-2.5583
W_3	-1.7±0.2		-2.77		-1.8937	-1.5067
W_1	-0.65±0.1		-1.00		-0.6998	-0.6000
$W_{1'}$		-0.15±0.1	0.02		-0.1500	0.2500
K_1	-3.1±0.2		-3.66	-2.70	-2.7549	-2.6549
K_1	-2.55±0.1		-3.45	-2.40	-2.5787	-2.2119
K_3	-0.9±0.2		-1.81		-1.0916	-0.7088
K_4	-0.45±0.1		-0.77	-0.50*	-0.5492	-0.4492
K_2			-0.25	-0.09	-0.2881	0.1119

[a]W. Eberhardt and E. W. Plummer, Phys. Rev. B 21, 3245 1980). The experimental Fermi energy was chosen as zero of energy.

[b]Average over the spin directions.

[c]C. S. Wag and J. Callaway, Phys. Rev. B 9, 4897 (1974).

[d]For the sake of clarity we only indicate the values found for the energy levels which have not been used for the fit. The values followed by an asterisk are the readjusted input values. The fit accurately reproduced the experimental data which were used as input. The values are given relative to the experiment Fermi energy as for the column based on experiment.

2.2 Surface Electronic States

2.2.1 Surface and Bulk States

The energy state, which is not introduced by the adsorbtion of foreign atoms but is inherent to the clean surface, is called the intrinsic surface state. Since atoms on the surface are arranged with two dimensional symmetry, the intrinsic surface state forms two dimensional energy bands and the bands have dispersion. The wave vectors have components parallel to the surface only. If foreign atoms are adsorbed on the surface, the electronic state of the surface is altered. If a kind of foreign atom forms a monolayer, then this foreign atom layer gives rise to a two dimensional energy band system. In this case, the theoretical treatment of the surface is practically the same as that of the intrinsic surface state. If the concentration of the adsorbed atoms or molecules is low and they are dispersed on the surface, their energy states are similar to those of the isolated atoms or molecules.

In more rigorous consideration, we should remind of a simple but important fact. In the three dimensional energy band approximation made before, we assume the Born-von-Karlmann boundary condition, in each of the three dimensional direction, x, y and z. In the layers near the surface, the Born-von-Karlmann boundary condition does not hold in the direction normal to the surface. This is obvious, since the crystal terminates at the surface.

Suppose the crystal surface is located at the plane, $z = 0$, and the bulk crystal exists in the region, $z < 0$. It is not unreasonable to assume that infinite arrays of atoms exists in the plane, $z = 0$ in the x and y directions. In these arrays, atoms are symmetrically aligned forming the two dimensional crystal. The potential of electrons in the surface layer has the two dimensional symmetry. Thus, one-electron state forms

the two dimensional energy bands, since the Born-von-Karlmann boundary condition holds in the two dimensional direction parallels to the surface.

The two dimensional energy bands can be calculated in manners similar to those for the three dimensional energy bands. Before describing the practical two dimensional energy bands, we consider the surface state using a simple qualitative model below.

A schematic illustration of the electron states and wave functions near the vacuum-crystal interface are given in Figs. 2.13 and 2.14. Fig. 2.13 shows the electron wave function in the z direction (the $\mathbf{k}_{\perp}$ direction) (Feuerbacher and Willis, 1976). There, $\varepsilon_v$represents the vacuum level. Note that $\varepsilon = 0$ at ε_v. Outside the crystal, electrons with energy positive magnitudes of energy can exist. Their states are those of free electrons. Inside the crystal, the electronic states are the energy band states. As we have already seen in Fig. 2.3, the energy levels are discrete for given $\mathbf{k}$. Thus a free electron state outside the crystal cannot always connect the band state inside the crystal. In some cases, the free electron states and the bands states connects smoothly, as shown in curve (e). From other view point, any energy band wave functions above ε_v are connected to the free electron wave function.

On the other hand, even if a free electron is injected on the crystal surface, the state cannot be connected to the band state unless the energy is the same. The injected electron state is evanescent toward the bulk solid. The electronic state is confined in the surface layer, as shown in curve (d). Although this state is a sort of the intrinsic state, it is called the evanescent state, since the state takes various energies continuously and distinguished from the intrinsic surface state for $\varepsilon < \varepsilon_v$ that takes the

energy limited by the two dimensional energy band dispersion. If an electronic transition occurs to the bulk band state or the evanescent state at $\varepsilon > \varepsilon_v$, the excited electron can come out of the crystal.

Below ε_v, three kinds of states are possible to occur. One is the ordinary bulk band state, as shown in curve (c). Since the energy is negative, there is no state connecting to this state outside the crystal. The second one is the intrinsic surface state. The state is localized in the surface layer, as shown in curve (a). It is also possible that the bulk energy band state and the surface band state are hybridized. In this case, the wave function has the feature of both surface and bulk band states, as shown in curve (b). The state like this is referred to as the surface resonance state.

Then the question arises: how the three different states below ε_v ($\varepsilon < 0$) occur. A qualitative explanation is given in Fig. 2.14 (Feuerbacher and Willis, 1976). Fig. 2.14 shows the energy band dispersion and related wave functions schematically. The upper figures illustrate energy bands and lower figures eigenfunction. There z stands for the distance from the surface normal to the surface. $\mathbf{k}_\perp$ and $\mathbf{k}_\parallel$ represent the components of the wave vector, $\mathbf{k}$, normal and parallel to the surface, respectively. On the left-hand side, the energy band of the bulk state is indicated. In the left half of the figure, the dispersion along the direction of $\mathbf{k}$ normal to the surface is shown. If we plot energy levels versus $\mathbf{k}_\parallel$, we obtain similar dispersion. If we plot energy levels for general wave vectors versus their components parallel to the surface, $\mathbf{k}_\parallel$, we have dispersion curves with some width. This width comes from the band dispersion toward the direction perpendicular to the surface. In the Fig. 2.14, this width is depicted as hatched parts. Note that $\mathbf{k}$ is not a good quantum number at the surface

due to the lack of periodicity normal to it, while $\mathbf{k}_{\|}$ is. So, for each value of $\mathbf{k}_{\|}$ a range of states is possible for the different allowed values for **k**. For instance, if the energy levels are plotted for bulk state inside the solid, at $\mathbf{k}_{\|} = 0$ they show dispersion as a function of $\mathbf{k}_{\perp}$ and thus, the bands have widths. The widths of these bands give the quasi-continuum of allowed states at the surface as shown by hatched areas. The state density of these 'bulk' states seen at the surface is not the same as that in the volume. The wave function amplitude, as the lower diagram on the left can be different near the surface, leading to a different local DOS. The bulk energy band plotted versus $\mathbf{k}_{\|}$ is referred to as the bulk band projected to the surface.

If the surface energy level occurs in the band gap of the projected bulk band, the corresponding state is quite localized near the surface and the wave function decays very rapidly toward the interior of the solid as well as toward the vacuum area. The corresponding state is a bound state below the vacuum level. This is obvious, since no state is allowed in the gap in the bulk. The energy level corresponding to this state is experimentally observable. The state is illustrated in the middle part of Fig. 2.14. This is the intrinsic surface state.

If the surface level occurs in a part within the projected bulk band, the surface state and the bulk state mix together to form a state gradually evanescent toward the interior of the solid. This state is referred to as the surface resonance state. This state is illustrated on the right-hand side in Fig. 2.13. A sharp resonance will occur if the decay is forbidden by the symmetry. Otherwise it will be broadened owing to decreased amplitude of the wave function into the volume of the crystal.

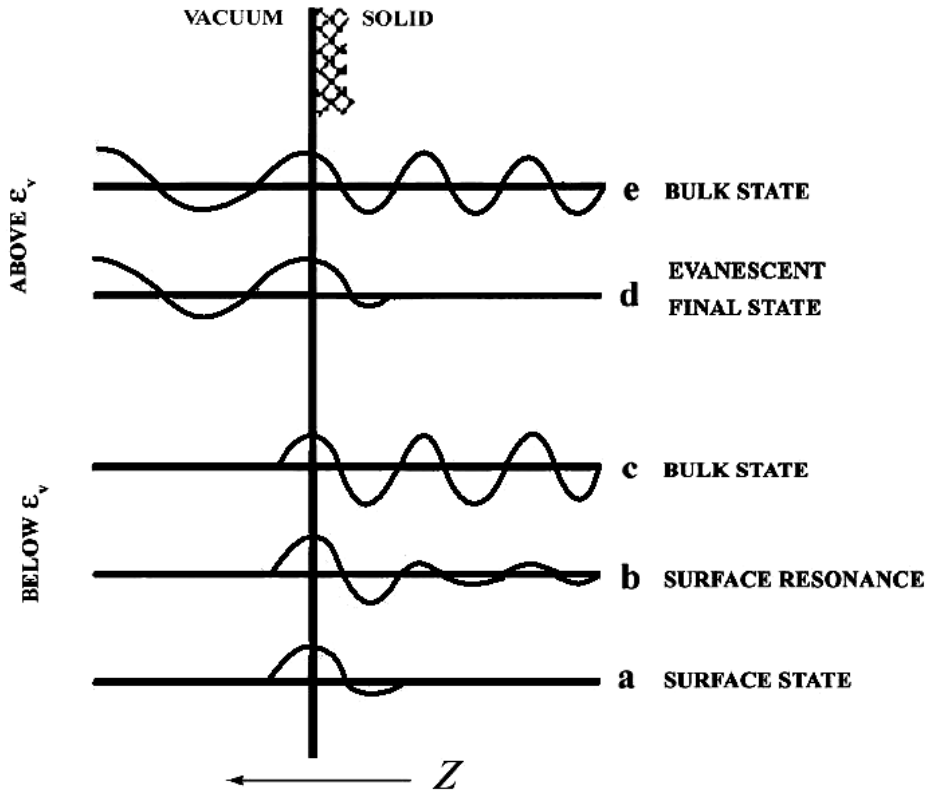

Fig. 2.13 Electronic wave function in the surface region

(Feuerbacher and Willis, 1976).

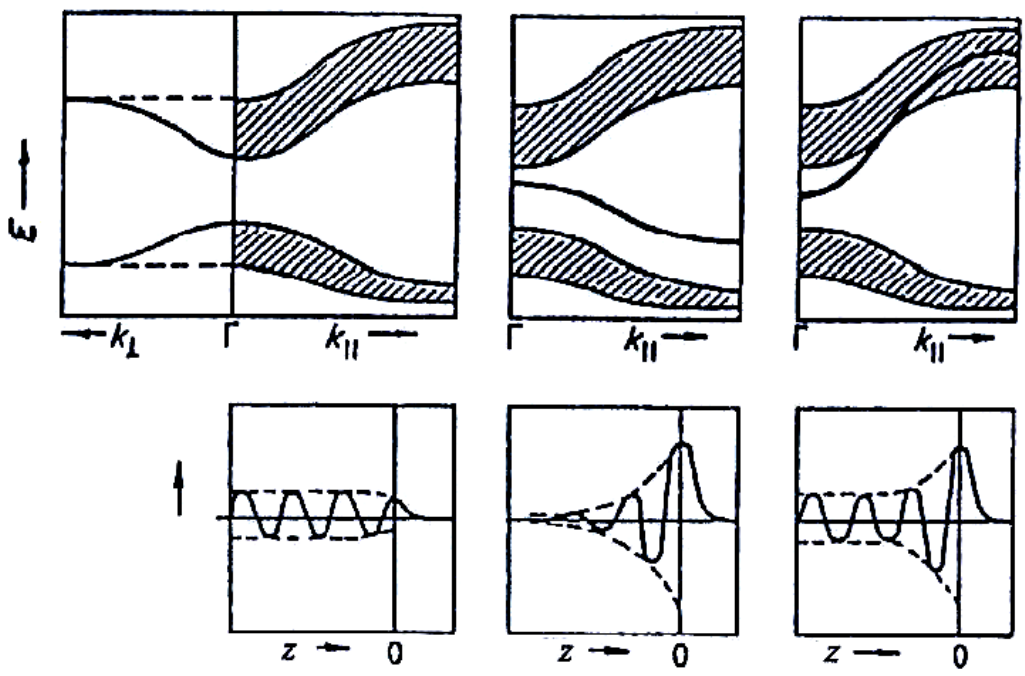

Fig. 2.14 Schematic illustration of the surface energy bands (upper panels) and the surface eigenfunctions (lower panels). The projected bulk bands (hatched part) are shown for comparison. Left represent bulk state, middle surface state and right surface resonanace. The surface occurs at $z = 0$ (Feuerbacher and Willis, 1976).

It has long been known that clean surfaces of single crystals metal reconstruct, *i.e*., the atoms in the surface layer adopt an arrangement which is not the same as a simple truncation of the bulk structure. Such reconstruction leads to change in the surface lattice that accompanies a change in the surface band structure, leading to reduction of the DOS at the Fermi level. Particularly, this is the case in a surface state that can drive the surface reconstruction.

2.3 Photoemission Spectroscopy

In this thesis, the photoemission spectroscopy technique has been used for the investigation of the electronic structure of Ni(111) surface. In this section, the fundamentals of photoemission are briefly overviewed. Experimental details will be described in the next chapter.

Photoemission is widely used in the study of electronic structure of solids. It utilizes the photoelectric effect in which an electron is ejected from the occupied electron levels of the sample. In a photoemission experiment, the kinetic energy of the photoelectrons usually varies from a few electron volts up to a few hundred electron volts, depending on the photon energy used. This results in the surface sensitivity of the technique, as the inelastic mean free path of a typical photoelectron in the solid is in the range of 5-30 Å. This means that UHV is necessary to maintain a surface of adsorbates during the time scale of measurement.

Photoemission intensity gives us the information of the density of states as

$$n(\varepsilon_B, \nu) \propto \sigma(\nu) D(\varepsilon_B) \tag{2.26}$$

Here, σ (v) is the excitation cross section at photon energy, hv. $D(\varepsilon_B)$ is DOS and ε_B is the binding energy which will be defined later. Useful information is the energy band dispersion curve expressed as

$$\varepsilon_\alpha(\mathbf{k}_\alpha) \text{ versus } \mathbf{k}_\alpha \tag{2.27}$$

Here, ε_α ($\mathbf{k}_\alpha$) is the energy band along a good symmetry line in the Brillouin zone. The process of obtaining the energy band dispersion curves by photoemission is often referred to as the band mapping. Angle-resolved photoemission measurements made in the energy band mapping. The energy band mapping can be made in the spin resolved mode. However, this is not in the scope of the present thesis and its principle is not described here. Since photoelectrons have a small but tunable escape depth, it is possible to see the surface and adsorbate state as well as bulk states.

2.3.1 Basic Principle

Photoemission is the phenomenon that electrons are emitted out of matter that is exposed to light. The electrons are called *photoelectrons*. Outside the solid, electrons are easy to handle and observe. Kinetic energy, momentum and spin are measured and analyzed. For implementing these, emission angle (θ_e) and azimuthal angle (ϕ_e) of electron emission are measured as shown in Fig. 2.15. From the properties of the photoelectrons in vacuum (kinetic energies and momentum), one can retrieve the properties of electrons inside the system investigated as will be described below.

(1) Energy distribution curve (EDC)

Regarding the photoemission spectrum described in equation (2.26), we practically measure the spectrum called the energy distribution curve (EDC). EDC is the number of primary photoelectrons, $n(\varepsilon_u, \nu)d\varepsilon$, emitted per unit time by excitation with monochromatic light with photon energy ($h\nu$). Thus, EDC is expressed as

$$n(\varepsilon_u, \nu)d\varepsilon = \frac{N(\varepsilon_u, \nu)d\varepsilon d\nu}{I_0(\nu)d\nu} \tag{2.28}$$

$$n(\varepsilon_u, \nu) = \frac{N(\varepsilon_u, \nu)}{I_0(\nu)} \tag{2.29}$$

Here, $N(\varepsilon_u, \nu)d\varepsilon\, d\nu$, is the number of excited primary photoelectrons and $I_0(\nu)\, d\nu$ is the light intensity. If we define the binding energy as

$$\varepsilon_B = h\nu - \varepsilon_u \tag{2.30}$$

EDC is also expressed in terms of the binding energy as

$$n(\varepsilon_B, \nu)d\varepsilon = \frac{N(\varepsilon_B, \nu)d\varepsilon d\nu}{I_0(\nu)d\nu} \tag{2.31}$$

$$n(\varepsilon_B, \nu) = \frac{N(\varepsilon_B, \nu)}{I_0(\nu)} \tag{2.32}$$

The number of photoelectrons per unit time is equivalent to photocurrents, J. Also, we measure the photocurrent in a solid angle, $d\Omega$, defined by the detector system. Thus, what we measure practically is

$$N(\varepsilon_u, \nu, \theta, \phi)d\varepsilon d\nu \frac{d\Omega}{4\pi} \tag{2.33}$$

In the actual spectrometer, we have broadening of the measured spectra owing to the overall energy resolution. Suppose the smearing of the real spectrum by resolution is given by the window function, $W(\varepsilon)$, the spectra we observe is deformed as

$$N(\varepsilon_u, \nu, \theta, \phi) = \frac{\int_{-\infty}^{\infty} N(u, \nu, \theta, \phi) W(u - \varepsilon) du}{\int_{-\infty}^{\infty} W(u) du} \tag{2.34}$$

If we know $W(\varepsilon)$ correctly, we can deconvolute $\overline{N}(\varepsilon)$ to obtain $N(\varepsilon)$.

(2) Binding energy

We have to establish the idea with which useful pieces of information can be drawn out through the analysis of the photoemission phenomena. Many early theoretical investigations targeted this analysis.

First, consider the system consisting of N electrons. Suppose its energy is $E_g(N)$. There is a photon with an energy, $h\nu$, enter. We regard the system of N electrons and a photon to be the initial state. In the final state of the photoexcitation, the photon disappears and an electron with a kinetic energy, ε_u, and the (N-1) electron system with an energy of $E_f(N-1)$ are left. The electron with ε_u is the photoelectron. From the energy conservation, we have

$$E_g(N) + h\nu = E_f(N-1) + \varepsilon_u \tag{2.35}$$

or,

$$h\nu - \varepsilon_u = E_f(N-1) - E_g(N) \tag{2.36}$$

From equation (2.30) can be written as

$$\varepsilon_B = E_f(N-1) - E_g(N) \tag{2.37}$$

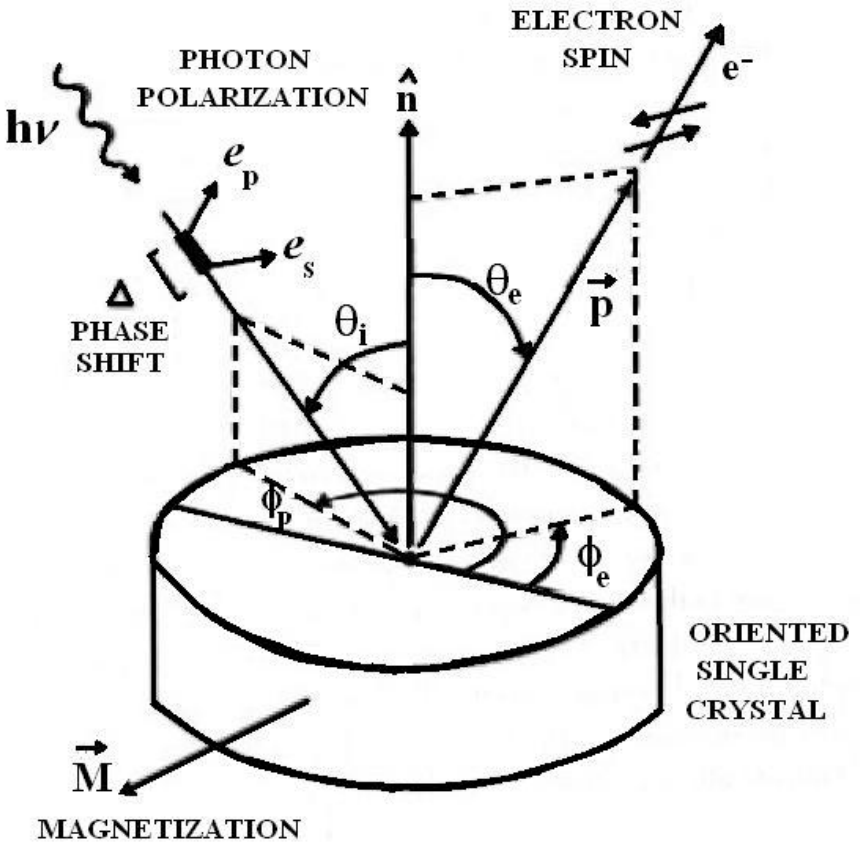

Fig. 2.15 Schematic diagram of spin and angle-resolved photoemission. This diagram is to show all the angular parameters. θ_i is the polar angle of photon incidence (incident angle). θ_e is the polar angle of photoelectron emission. ϕ_p and ϕ_e are azimuthal angles of light incidence and photoelectron emission, respectively. **p** is the momentum of the photoelectron. e_s (s-polarization) and e_p (p-polarization) are electric vector components of excitation light parallel and normal to the plane of incidence, respectively.

Since $0 > E_f(N-1) > E_g(N)$, we see $\varepsilon_B > 0$. We have to relate ε_u with a quantity measurable in the space outside the sample (vacuum). Another issue we have to make is to find the meaning of the right-hand side of equation (2.35).

(3) Relaxation

We know that a sample and a photon exist in the initial state of photoemission and the photon disappears and a photoelectron comes out of the sample in the final state, as mentioned already. Thus, we have to find what happens in the intermediate state in the sample, which appears to be a black box. Many pieces of theoretical work have been carried out to give the answer to this. None of the work seems to have been successful. Instead, the assumption of the three step process proposed empirically has been successful (Berglund and Spicer, 1964; Spicer and Krolikovski, 1969).

Suppose we can separate the energy of an electron to come out of the sample after the excitation from the energy of remaining (N-1) electrons. It is not absurd to assume the energy, ε_g, of the excited electron to leave the sample is given as

$$E_g(N) = \varepsilon_g + E_g(N-1) \tag{2.38}$$

From equations (2.37) and (2.38), we have

$$\varepsilon_B = E_f(N-1) - E_g(N-1) - \varepsilon_g \tag{2.39}$$

Generally, $E_f(N-1)$ is not equal to $E_g(N-1)$. It is the energy of the photoproduced hole. Let $E_f(N-1)$, the hole energy, be written as

$$E_f(N-1) = E_g(N-1) + E_R \tag{2.40}$$

E_R is the energy of the many electron interaction of the hole generated by the photoexcitation with the surrounding medium. This energy often called the relaxation energy. The binding energy, ε_B, given in equation (2.39) is written as

$$\varepsilon_B = E_R - \varepsilon_g \tag{2.41}$$

In some cases, E_R is negligible. In these cases, one electron approximation is valid as in the case of the energy band approximation. There we have

$$\varepsilon_B = -\varepsilon_g \tag{2.42}$$

In a case like this, the binding energy defined in equation (2.30) gives us the negative of the initial one electron energy of the photoelectron. Remember $\varepsilon_B > 0$, $\varepsilon_g < 0$.

2.3.2 The Three-step Process

In the analyses of EDC's, we usually postulate the three-step model, although this model has not yet been verified theoretically from the first principle. As mentioned before, the theoretical treatments of the photoemission processes from this stand point have not been successful. However by experience, we know that the three-step model explains observed data quite well. In the three-step model, the photoemission in a solid material is regarded to occur as a result of following three consecutive partial processes:

1) Optical excitation of electrons inside the solid

2) Transport of the excited electrons to the surface

3) Transmission of photoelectrons through the surface into vacuum.

In order to see the consequences of the three-step process, we have to carry out some simple calculations. We consider the following simplified model, although the simplification does not make the general validity of the model lost. We consider that the first step of photoemission occurs as shown in Fig. 2.16. There, excitation light with energy $h\nu$ and intensity $I_0(\nu)$ per unit beam cross section falls normally on a sample of a prism shape with a square surface. The cross section of the sample is S. We assume that light penetrates toward the z direction from $z = 0$. The sample surface is at $z = 0$.

First, suppose photoelectrons are generated at a small portion, $dzdS$, around a point in a slab with a thickness of dz located at z. The photoelectrons migrate toward any directions in space. We consider the photoelectrons propagating toward the direction, (θ,ϕ). Here we must emphasize that the three-step process postulates the photoelectron production to be a localized process. In the complete many electrons viewpoint, we cannot specify where the photoelectron is produced.

In the first step, we assume that the number of photoelectrons generated in the small slab $dzdS$ is equal to that of photons absorbed in this slab. Then the number of photoelectrons, dN , generated in the small slab is equal to

$$dI = I_o(\nu)dS \cdot \eta(\nu)\exp(-\eta(\nu)z)dz \tag{2.43}$$

Here, $\eta(\nu)$ is the absorption coefficient. The fraction of photoelectrons migrating in the direction (θ,ϕ) is given as

$$dN(\theta,\phi) = \frac{dI \sin\theta\, d\theta d\phi}{4\pi}$$

$$= \frac{I_0 dS\eta \exp(-\eta z)dz \sin\theta\, d\theta d\phi}{4\pi} \tag{2.44}$$

Photoelectrons are scattered while they are traveling to the surface. If the scattering is elastic, the process gives rise to the photoelectron diffraction. If the scattering is inelastic, photoelectrons lose a part of energies they possess and they are not primary electrons with the original kinetic energy, ε_u. In the second process of the three steps, we treat the survival of the primary electron using the mean free path for the scattering. In other words, complicated details of the scattering are renormalized into one parameter, the mean free path, l. The fraction of electrons to survive without being scattered in a migration distance of d is expressed as exp(-d/l). Therefore, the number of primary photoelectrons arriving at the surface in the direction, (θ,ϕ), from a small slab $dzdS$ at z is given as

$$= dN(\theta,\phi)\exp(\frac{-z}{l\cos\theta})$$

$$= \frac{I_0 dS\eta \exp\left\{-\left(\eta+\frac{1}{l\cos\theta}\right)z\right\}dz\sin\theta d\theta d\phi}{4\pi} \qquad (2.45)$$

It should be remarked that the light penetration depth is much smaller than the size of the sample cross section. Therefore, in the integration of equation (2.45), we ignore the dependence of θ and ϕ on z and integration on θ and ϕ can be carried out from $\theta = 0$ to $\pi/2$ and from $\phi = 0$ to 2π, respectively.

First we perform the integration on z, from $z = 0$ to ∞. The result is given as

$$dN_\Omega = \frac{I_0 dS\left\{\frac{\eta l\cos\theta}{\eta l\cos\theta+1}\right\}\cdot\sin\theta d\theta d\phi}{4\pi} \qquad (2.46)$$

If we integrate equation (2.46) over S, we obtain the number of primary photoelectrons reaching the surface as

$$N_\Omega = \frac{I_0 d\Omega \eta l \cos\theta}{4\pi(\eta l \cos\theta + 1)} \tag{2.47}$$

$$d\Omega \equiv \sin\theta d\theta d\phi \tag{2.48}$$

Apart from the treatment of 4π, N_Ω present the case of the angle-resolved photoemission. Since the absorption coefficient of a solid material in the vacuum ultraviolet (VUV) and soft X-ray (SX) region is less than 10^{-5} cm and the mean free path in a solid material is around 10^{-7} cm, $\eta l\cos\theta < 10^{-2} (<<1)$. Then we have

$$N_\Omega = \frac{I_0 d\Omega \eta l \cos\theta}{4\pi} \tag{2.49}$$

Thus the number of primary photoelectrons reaching the surface is proportional to the absorption coefficient η. If we integrate equation (2.46) over θ and ϕ, we have

$$dN = \frac{I_0 dS\left\{1 - \frac{1}{\eta l}\ln(1+\eta l)\right\}}{2} \tag{2.50}$$

Since ηl is very small as compared with 1, equation (2.50) becomes

$$dN = \frac{I_0 dS \eta l}{4} \tag{2.51}$$

Integration over S, we have

$$N = \frac{I_0 S \eta l}{4} \tag{2.52}$$

In the third step, we have to consider the escape of primary photoelectrons from the surface. In the three-step model, we assume the probability of primary

photoelectrons to leave the surface $T(\varepsilon_u)$. With this escape probability, the number of primary photoelectron leaving the surface is given as

$$N = \frac{1}{4} I_0 S \eta l T(\varepsilon_u) \tag{2.53}$$

From equation (2.49), the angle-resolved case

$$N_\Omega = \frac{1}{4\pi} I_0 d\Omega \eta l \cos\theta T(\varepsilon_u) \tag{2.54}$$

Spicer and coworkers (Berglund and Spicer, 1964; Spicer and Krolikovski, 1969) suggested that the escape function is given as

$$T(\varepsilon_u) = \frac{1}{2}\left\{1 - \left(\frac{\chi}{\varepsilon_u}\right)^{3/2}\right\} \qquad \text{for } \varepsilon_u > \chi \tag{2.55}$$

$$= 0 \qquad \text{for } \varepsilon_u < \chi$$

Here, χ is the work function of the sample. The shape of the escape function is presented in Fig. 2.17

It should be remarked that we are concerned with an isotropic medium and essentially the directional average. Otherwise, $T(\varepsilon_u)$ is dependent on θ and ϕ. Fig. 2.17 shows $T(\varepsilon_u)$ versus ε_u / χ. For kinetic energies below about 7χ, $T(\varepsilon_u)$ changes steeply as ε_u changes. Therefore, EDC can be modified considerably by $T(\varepsilon_u)$, if EDC is recorded over an appreciable range of ε_u. The modification occurs in a way that the photoelectron intensity decreases monotonically as the kinetic energy is decreased. Suppose χ = 2.0 eV. Then, $T(\varepsilon_u)$ modifies the photoelectron intensity by 25% for scanning from 4 eV to 3 eV, 14% from 15 eV to 10 eV, and 7% from 30 eV to 20 eV.

In PES experiments using synchrotron radiation, energies of excitation light are usually selected above 15 eV. If the excitation energy range is selected properly, $T(\varepsilon_u)$ does not modify EDC seriously.

In many cases, the absolute values of photoemission intensities are not important in the data analyses. Therefore, we make a simplifying assumption on $T(\varepsilon_u)$ based on the discussion described above. The assumption is as follows:

$$T(\varepsilon_u) = 1 \qquad \text{for } \varepsilon_u > \chi \tag{2.56}$$

$$= 0 \qquad \text{for } \varepsilon_u < 0$$

Then, for $\varepsilon_u > \chi$, equations (2.53) and (2.54) are given as

$$N = \frac{1}{4} I \eta l \tag{2.57}$$

$$N_\Omega = \frac{d\Omega}{4\pi} I \eta l_\theta \tag{2.58}$$

Here, we put $I_0 S \equiv I$ and $l \cos\theta \equiv I_0$

In case of a number of isolated absorption centers, η is written as

$$\eta = N_0 \sigma. \tag{2.59}$$

Here, N_0 is the density of the absorption centers. σ is the absorption cross section. In solids, the optical absorption occurs often cooperatively by many atoms. However, we formally assume that equation (2.54) holds even in solids. In this case, N_0 represents the density of absorption centers, atoms or molecules in the solid. By comparing equations (2.32), (2.58), (2.59), EDC is given as

$$n(\varepsilon_B, \nu) = A \sigma(\varepsilon_B, \nu) l (h\nu - \varepsilon_B) \tag{2.60}$$

2.3.3 Cross Section

According to equation (2.60), we know EDC expresses the spectrum of the transition cross section σ ($\varepsilon_{B,}$ ν) . Therefore, we have to analyze σ ($\varepsilon_{B,}$ ν) in a more detail. Apart from unimportant factor, which can be renormalized into the factor, A, the transition cross section is written as

$$\sigma(\varepsilon_B,\nu) = \left|\langle \psi_f \left| \mathbf{T} \right| \psi_g \rangle\right|^2 \delta(E_f - E_g - h\nu)\delta(E_f(n-1) - E_g - \varepsilon_B) \qquad (2.61)$$

where ψ_f and ψ_g are the many electron eigenfunctions describing the final and initial states, respectively. **T** is the transition matrix expressed as

$$\mathbf{T} = V_T + V_T \frac{1}{h\nu + E_g - H_0 - V_T + iO^+} V_T \qquad (2.62)$$

V_T is the perturbation potential to cause the transition. V_T includes both optical and Auger transitions. In the present work, we are not dealing with the Auger transition, which is important in the resonant photoemission. In the case like this, the V_T is simplified to be

$$V_T = p_e \qquad (2.63)$$

where, p_e is the operator for the optical dipole transition.

Before we discuss the transition probability, equation (2.61), we better look into the assumption we made in the three-step process leading to the energy relation equations (2.38) and (2.39). The fundamental relation equation (2.35) or (2.36) is correct, since it mentions the energy conservation. The relation equation given as (2.38) is not quite so obvious. Since the hamiltonian given in equation (2.6) is correct, its solution obtained by the Hartree-Fock approximation is best approximate solution unless the

electron under consideration is not very much localized. The many electron state is expressed as a Slater determinant. The one electron energy, ε_g, as expressed as in equation (2.38) is given by the Koopmans theorem (Kittel, 1967; Seitz, 1940). The Koopmans theorem states that the Hartree-Fock energy of the electron in the n state is just the negative of the energy required to remove the electron in the state n from the solid, provided that the Hartree-Fock functions are extended functions of the Bloch type and that the electronic system is very large.

Because the electron charge is spread throughout the entire crystal, the Hartree-Fock functions will be essentially identical for the problem with or without an electron in the state *n*. This is the basic assumption. Thus, Koopmans theorem indicates that the relation equation (2.40) is valid. A rigorous treatment is found in a textbook on the excitons by Knox (1963).

The fundamental assumption made in the Koopmans theorem is implicitly used in the three-step model. In the integration over *dS* leading to equation (2.47), we assume that all points in the thin slab are equivalent. This is equivalent to the fundamental assumption in Koopman's theorem. When we consider the excitation cross section, we consider that the many electron eigenfunctions, ψ_f and ψ_g are written by Slater determinants. We assume that each electronic state is described by an ideal Hartree-Fock solution. Practically we use the approximation such as the energy band or the completely localized functions as in the case of the 4f electron.

If we use the Slater determinants as the many electron functions, we may write the Slater determinants in the form of expression as

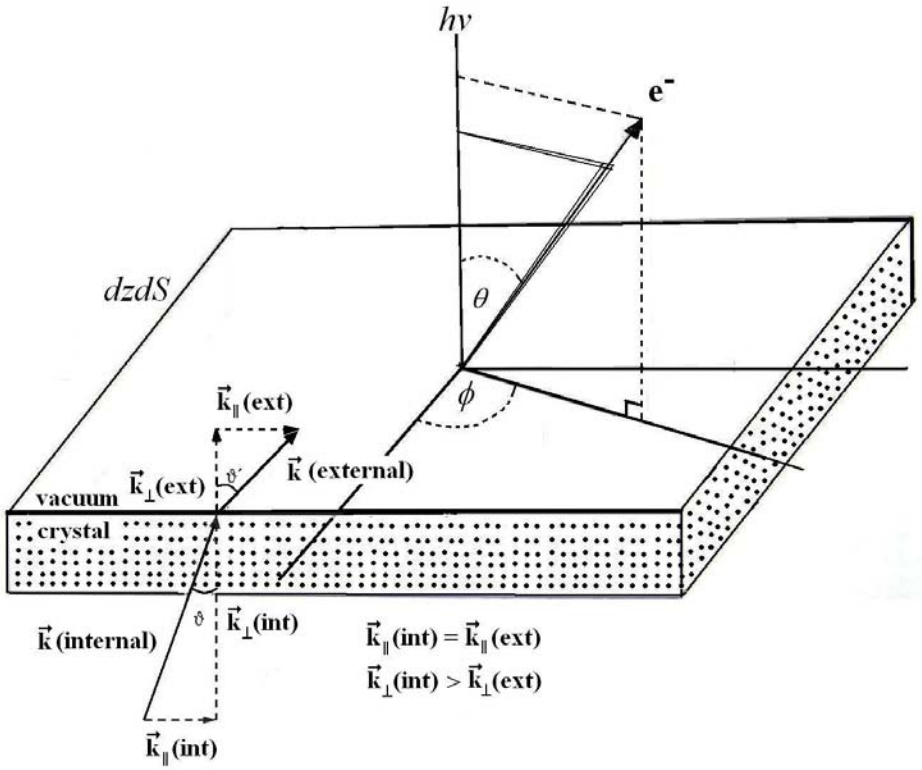

Fig. 2.16 Schematic illustration of the generation of photoelectrons. Excitation light with energy *hv* falls normally on the sample with the surface area, *S*. Photoelectrons generated in a small portion, *dz dS*, at *z* from the surface and progressing toward the direction (θ,ϕ) are considered. The sample surface is at $z = 0$. Excitation light propagates toward $z > 0$.

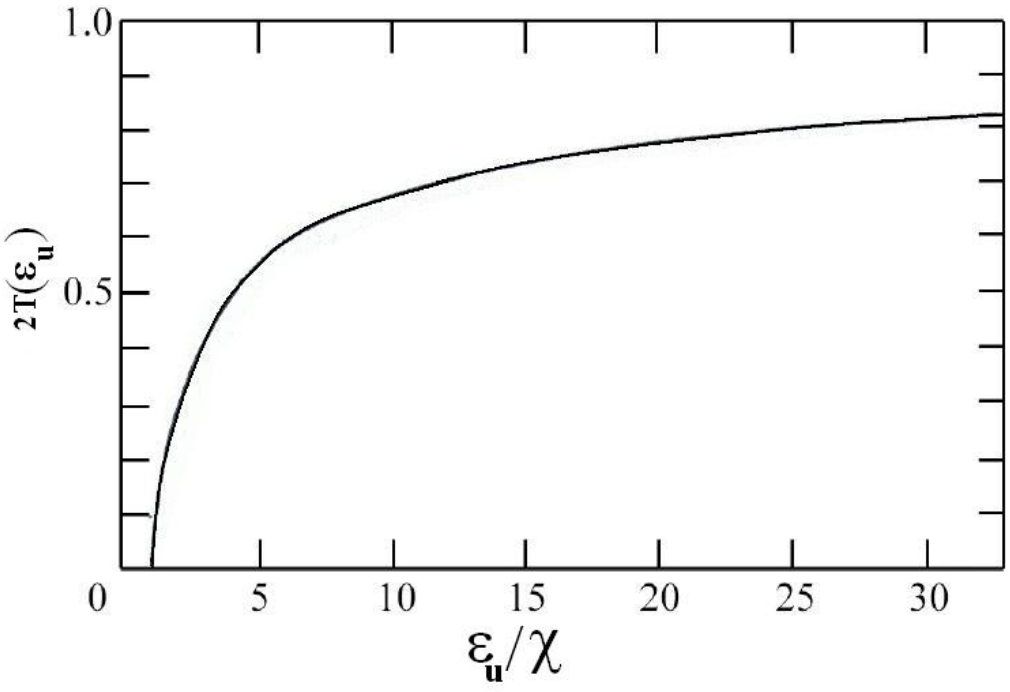

Fig. 2.17 Escape function versus ε_u/χ. ε_u : Kinetic energy; χ : Work function (Berglund and Spicer, 1964).

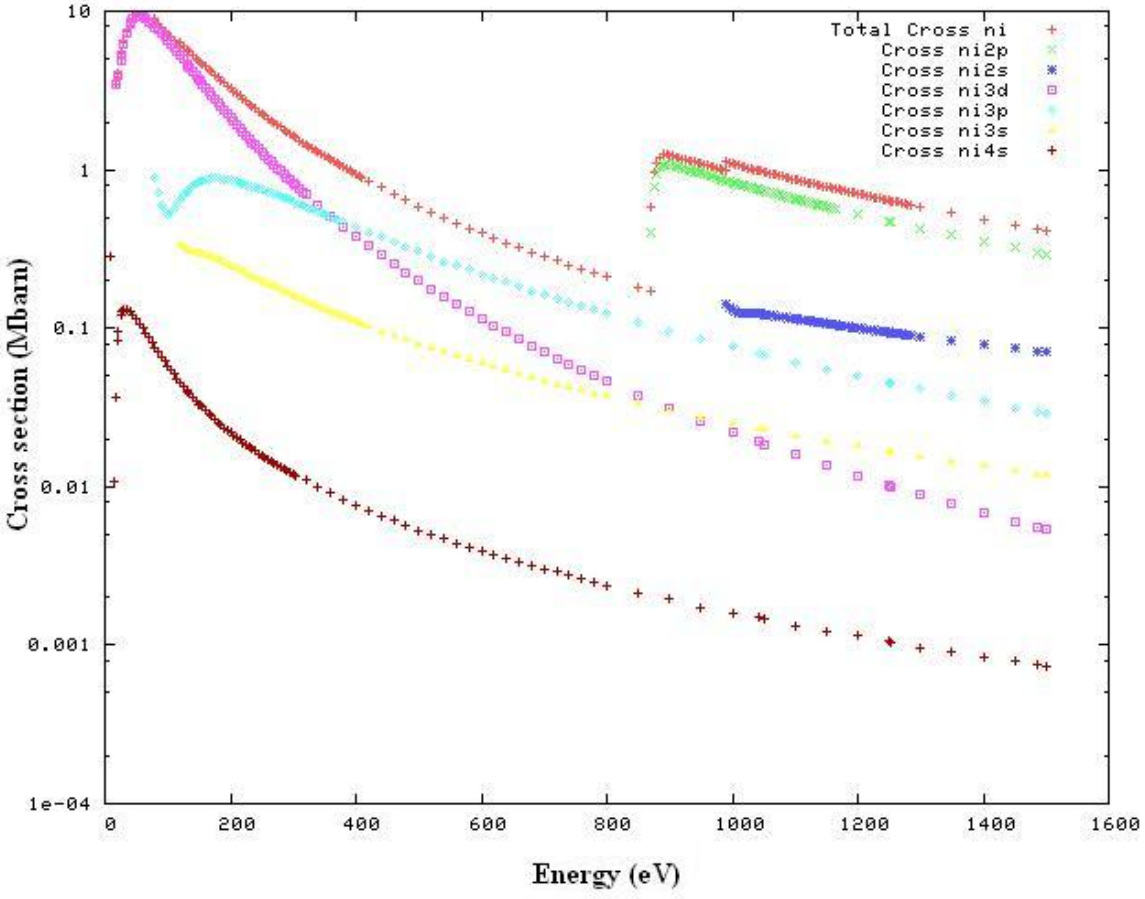

Fig. 2.18 Atomic subshell photoionization cross section of Ni for 0-1500 eV(Yeh and Lindau, www, 1985).

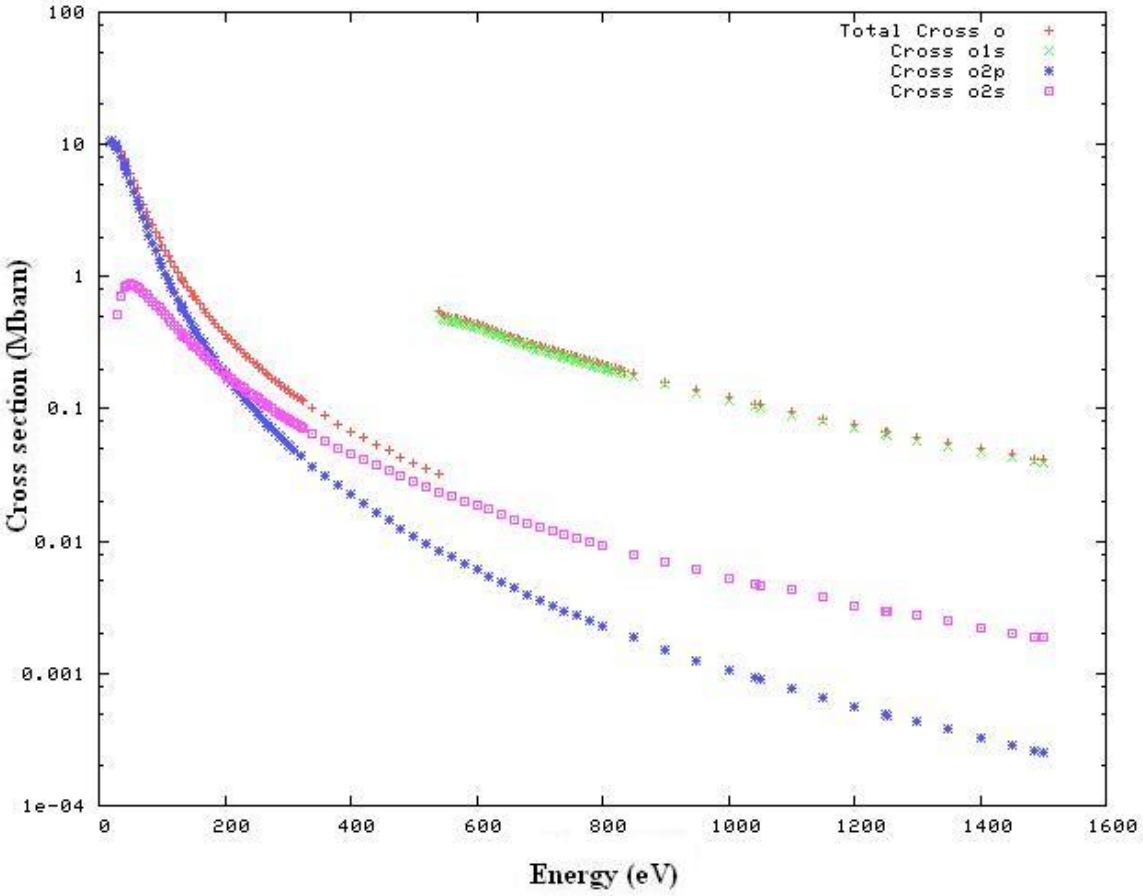

Fig 2.19 Atomic subshell photoionization cross section of O for 0-1500 eV(Yeh and Lindau, www, 1985).

$$|\psi_f\rangle = \sum_f |f_i\rangle |\psi_{fi}(N-1)\rangle \tag{2.64}$$

$$|\psi_g\rangle = \sum_i |g_i\rangle |\psi_{gi}(N-1)\rangle \tag{2.65}$$

Note that the matrix equation $|\psi_{fi}(N-1)\rangle$ and $|\psi_{gi}(N-1)\rangle$ include signs for expansion. We select the one electron final state experimentally. If we write the selected function as $|f\rangle$, the final state may be written as

$$|\psi_f\rangle = |f\rangle |\psi_f(N-1)\rangle \tag{2.66}$$

Using equations (2.65) and (2.66), excitation cross section in equation (2.61) is written as

$$\sigma(\varepsilon_B, \nu) = A\sum_i \left|\langle\psi_f(N-1)|\psi_{gi}(N-1)\rangle\right|^2 \left|\langle f|p_e|g_i\rangle\right|^2$$
$$\delta(E_g - E_f - h\nu)\times\delta(\varepsilon_B - h\nu + \varepsilon_u) \tag{2.67}$$

Here $|g_i\rangle$ and $|f\rangle$ represent the Hartree-Fock one-electron functions. Particularly, $|g_i\rangle$ represents the one-electron orbital of the electron to be excited. If the Koopmans theorem holds and the following relation is valid:

$$\left|\langle\psi_f(N-1)|\psi_{gi}(N-1)\rangle\right|^2 = 1 \tag{2.68}$$

then, the transition cross section is given by the one electron functions as

$$\sigma(\varepsilon_B, \nu) = A\sum_i \left|\langle f|p_e|g_i\rangle\right|^2 \delta(\varepsilon_f - \varepsilon_g - h\nu)\delta(\varepsilon_f + \varepsilon_B - h\nu) \tag{2.69}$$

The meaning of the condition given by equation (2.68) is clear: When an electron is removed from the system and brought into an excited orbit, the remaining (N-1) electron system is unchanged.

In case of the energy band approximation is good, equation (2.69) is written as

$$\sigma(\varepsilon_B,\nu)=A\sum_{\alpha,\mathbf{k},\mathbf{K}}\left|\langle h\nu-\varepsilon_B,\mathbf{k}'|p_e|\alpha,\mathbf{k}\rangle\right|^2\delta(\mathbf{k}'-\mathbf{k}-\mathbf{K})\delta(-\varepsilon_{\alpha,\mathbf{k}}-\varepsilon_B)$$

$$=A\sum_{\alpha,\mathbf{k},\mathbf{K}}\left|\langle h\nu-\varepsilon_B,\mathbf{k}+\mathbf{K}|p_e|\alpha,\mathbf{k}\rangle\right|^2\delta(-\varepsilon_{\alpha,\mathbf{k}}-\varepsilon_B) \tag{2.70}$$

The δ function on **k** is brought about by the momentum conservation inherent in the transition matrix element. α distinguishes the energy bands. The partial DOS, $\rho^{(l)}$ and DOS, ρ, based on the energy band approximation are given, respectively, as

$$\rho^{(l)}(\varepsilon_B)=\sum_{\alpha,\mathbf{k}}\delta\left(-\varepsilon^{(l)}_{\alpha,\mathbf{k}}-\varepsilon_B\right)$$

$$\rho(\varepsilon_B)=\sum_l\rho^{(l)}(\varepsilon_B)$$

$$=\sum_{\alpha,\mathbf{k}}\delta(-\varepsilon_{\alpha,\mathbf{k}}-\varepsilon_B) \tag{2.71}$$

Here, l distinguishes the orbital symmetry of the states. Since the transition moment appearing in equation (2.70) is a slowly varying function of ε_B, we replace it with the average that is dependent on the symmetry parameter, l, as

$$\sigma(\varepsilon_B,\nu)=A\sum_l M_l(\nu)\rho^{(l)}(\varepsilon_B) \tag{2.72}$$

As the conclusion, EDC in the energy band approximation is given as

$$n(\varepsilon_B,\nu)=A\sum_{\alpha,\mathbf{k},\mathbf{K}}\left|\langle h\nu-\varepsilon_B,\mathbf{k}+\mathbf{K}|p_e|\alpha,\mathbf{k}\rangle\right|^2\delta(-\varepsilon_{\alpha,\mathbf{k}}-\varepsilon_B) \tag{2.73}$$

2.3.4 Electron Escape Depth

In the expression of EDC, a quasi-constant factor, *l*, is included. We have defined this parameter as the mean free path. In case of EDC, this parameter is referred to as the escape depth. The definition of the escape is given in section 2.32. The number, *N*, of primary of electrons survive after travelling the distance, *d*, is given by

$$N = N_0 e^{-d/l} \tag{2.74}$$

Here, *l* is the mean free path and thus the escape depth.

The escape depth of the electron, *l*, is determined by electron-electron interaction at the energy of interest. In the present case, the photoelectron kinetic energy, ε_u, is in the range: ε_u =10-1000 eV. The Born approximation shows that the cross-section for electron-electron scattering σ_{sc} is given by

$$\frac{d\sigma_{sc}}{d\Omega d\varepsilon_u} \propto \frac{\hbar^2}{(\pi e a_0)^2}\frac{1}{k^2}\mathrm{Im}\left[\frac{1}{\varepsilon(k,\varepsilon_u)}\right] \tag{2.75}$$

Thus $1/l$ is essentially determined by the dielectric function, $\varepsilon(k, \varepsilon_u)$, which is dependent on materials. Here, ε_u is the electron energy and □k is its momentum. This material effect on the escape depth will be observed when the kinetic energy is comparable to the binding energy of a valence electron of ~10 eV. Whereas, for the ε_u > 10 eV, the electron in solids can be described by a free-electron gas because the binding properties are no longer important. In this case, the inverse escape depth is described by the mean electron-electron distance r_s which is roughly equal for all materials. Then one obtain (Hüfner, 1996),

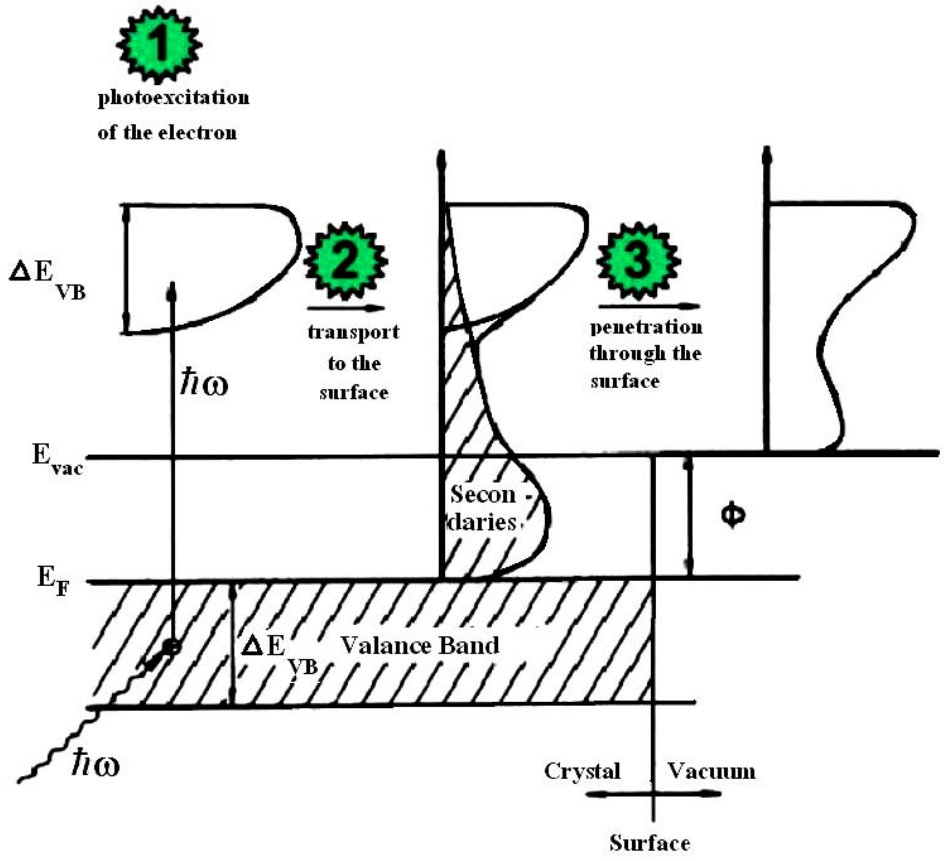

Fig. 2.20 The three-step model of photoemission: (1) photoexcitation of electrons; (2) travel to the surface with concomitant production of secondary (shaded); (3) penetration through the surface (barrier) and escape into the vacuum (Hüfner, 1996).

$$l^{-1} \cong \sqrt{3}\frac{a_0 R}{E_k} r_s^{-3/2} \ln\left[\left(\frac{4}{9\pi}\right)^{2/3} \frac{\varepsilon_u}{R} r_s^2\right] \tag{2.76}$$

where, a_0 = 0.529 Å, R = 13.6 eV, and r_s is measured in units of Bohr radius a_0. This gives us the escape depth as function of kinetic energy, which is called "universal curve", shown in Fig. 2.21. Suppose the kinetic energy of a photoelectron is not much different from the photon energy, $h\nu$. Then around the photon energies of $h\nu$ = 50-100 eV, the universal curve takes its minimum of ~5 Å. Hence the photoemission spectra taken at $h\nu$ = 50-100 eV are most surface-sensitive.

2.3.5 Measurement of EDC's

So far, we have been considering photoelectrons in the sample. Their kinetic energies are representatively expressed as, ε_u. Now we have to relate ε_u to the kinetic energies observed outside the sample. This is not obvious as we mentioned earlier. For instance, the concept shown in Figs. 2.13 and 2.14 must be treated rigorously theoretically.

After simplifying assumption as the three step model to regard the photoelectron to be retarded by the field of the electron affinity when leaves the surface and jump deep into the vacuum. When the electron enters the spectrometer system, the electron sees another retardation or acceleration field. From the consideration of the contact potential, it is verified that the electron enters the spectrometer system with a kinetic energy of ε_k' given as

$$\varepsilon_k' = \varepsilon_u - \chi_s \tag{2.77}$$

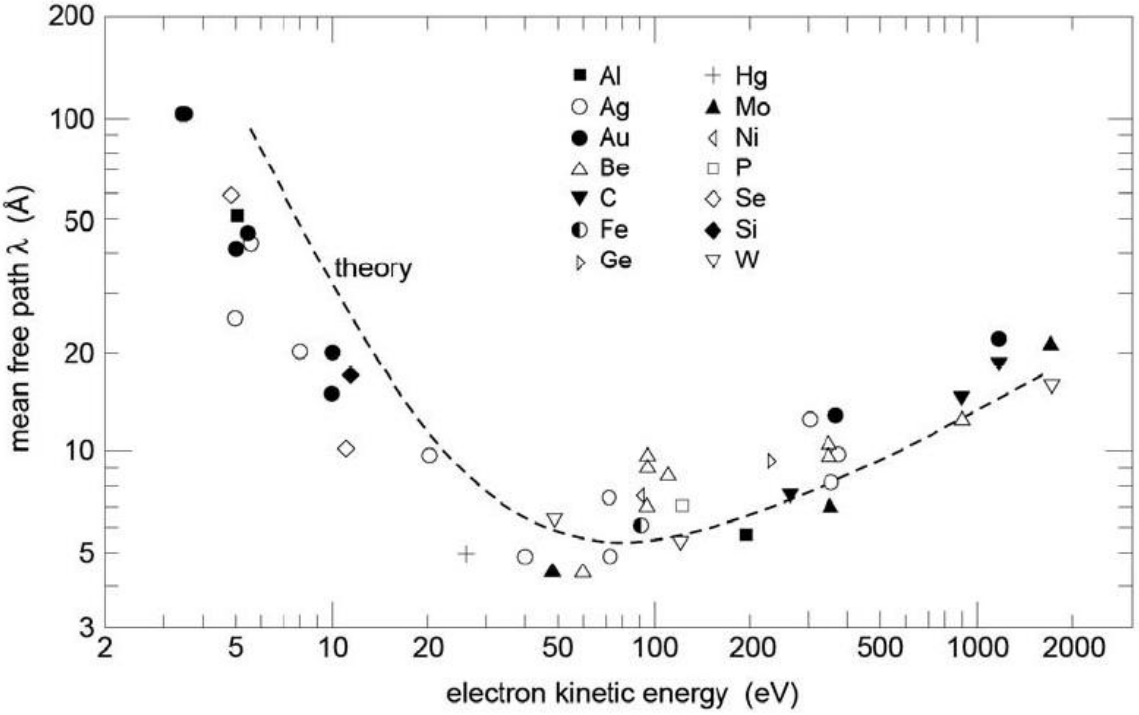

Fig. 2.21 The mean free path or escape depth of the electrons in solid. The open and close symbols represent experimental measurements and the dashed curve a calculation (Hüfner, 1996).

where, χ_s is the work function of the spectrometer entrance point. However, the kinetic energy, ε_k , of a photoelectron is assumed just to be

$$\varepsilon_k = \varepsilon_u - \chi \tag{2.78}$$

where, χ is the work function of the sample.

Electron emitted from a sample as it is irradiated with monochromatic light are collected with an electron lens, transferred to an energy analyzer and detected with an electron multiplier. As an electron jumps into an electron multiplier, the number of electrons emerging in the output of the electron multiplier is multiplied by a factor of 10^6 and pulse with measurable currents appears. A preamplifier reduces the impedance; a linear amplifier amplifies the pulse heights in an appropriate range; a counter counts the number of pulse per second. If the rate meter is inserted in a manner shown in Fig. 2.22, the number of pulse per unit time can be monitored. The number of pulses per unit time is stored in a microcomputer. Energy analyzers are usually of the electrostatic type, where electrons are either deflected or repelled by the electric field. Commonly used one is made of an electrostatic condenser, in which electrons passing though the space between electrodes are deflected by the electrostatic field of condenser. There, only electrons with specific kinetic energy can pass though slits after moving along the trajectory determined by the field strength. By changing the field strength, electrons are selected according to their kinetic energy. This process is called as the energy analysis. The energy analysis is made by sweeping the voltage applied to the electron lens or to the condenser. The computer controls the action of the whole system including the wavelength scanning of a monochrometer.

Since we are dealing with Ni sample, the energy states of which are described well with the energy band picture, we obtain the relation

$$\left.\begin{aligned} h\nu &= \varepsilon_u + \varepsilon_B \\ &= \varepsilon_u - \varepsilon_g \end{aligned}\right\} \tag{2.79}$$

The relation equation (2.79) is easily derived from relations in equation (2.40) to (2.42). Equation (2.79) indicates the energy conservation of single one-electron as shown in Fig. 2.23.

What we measure, however, is not ε'_k but the kinetic energy, $\hat{\varepsilon}'_k$, which the photoelectron has in the field of the condenser. Usually, the photoelectron is retarded by the electron lens before it enters the entrance slit of the analyzer. The relation between ε'_k and $\hat{\varepsilon}'_k$ under the presence of a retardation voltage, V_R, is shown in Fig. 2.22. In Fig. 2.22, the electron lens are replaced by a retardation electrodes for simplicity. In the spherical electrostatic energy analyzer, the kinetic energy of photoelectron passing though the analyzer is proportional to the voltage, V_P, applied to the condenser. If the proportionality constant is referred to as α, the argument described above gives the binding energy as

$$\varepsilon_B = h\nu - \chi_s - eV_R - \alpha V_P \tag{2.80}$$

where χ_s is the work function of the entrance aperture of spectrometer. By the simple condition of the electron motion and the application of the Gauss theorem to the analyzer, it is proved the α is given as

$$\alpha = e\frac{r_1 r_2}{r_2^2 - r_1^2} \tag{2.81}$$

where, r_1 and r_2 are radii of inner and outer spheres, respectively.

If an EDC is measured on a metallic sample and a well defined Fermi edge is obtained at parameters (v_F, V_{RF}, V_{PF}), χ_s is given as

$$\chi_s = h\nu_F - eV_{RF} - \alpha V_{PF} \tag{2.82}$$

Since α is obtained by the calibration with monochromatic electron beams using the relation

$$\alpha\left(eV_P - eV_{PO}\right) = \hat{\varepsilon}'_k - \hat{\varepsilon}'_{ko} \tag{2.83}$$

we have all measurable quantities on the right-hand side of equation (2.82)

One important fact about the electrostatic energy analyzer is that the resolving power is independent of the kinetic energy. By the use of equation (2.81), it is easily shown that

$$\left|\frac{\hat{\varepsilon}'_k}{\Delta\varepsilon}\right| = \frac{R}{w} \tag{2.84}$$

where, R is the diameter of the electron trajectory in the analyzer. R is given as

$$R = r_1 + r_2 \tag{2.85}$$

Thus we have

$$\left|\frac{\hat{\varepsilon}'_k}{\Delta\varepsilon}\right| = \beta \tag{2.86}$$

where β is a constant determined by the shape and the size of the energy analyzer. In many cases, β is fixed to a value around 100. Equation (2.86) indicates that $\Delta\varepsilon$ is made small if we reduce $\hat{\varepsilon}'_k$ by large retardation.

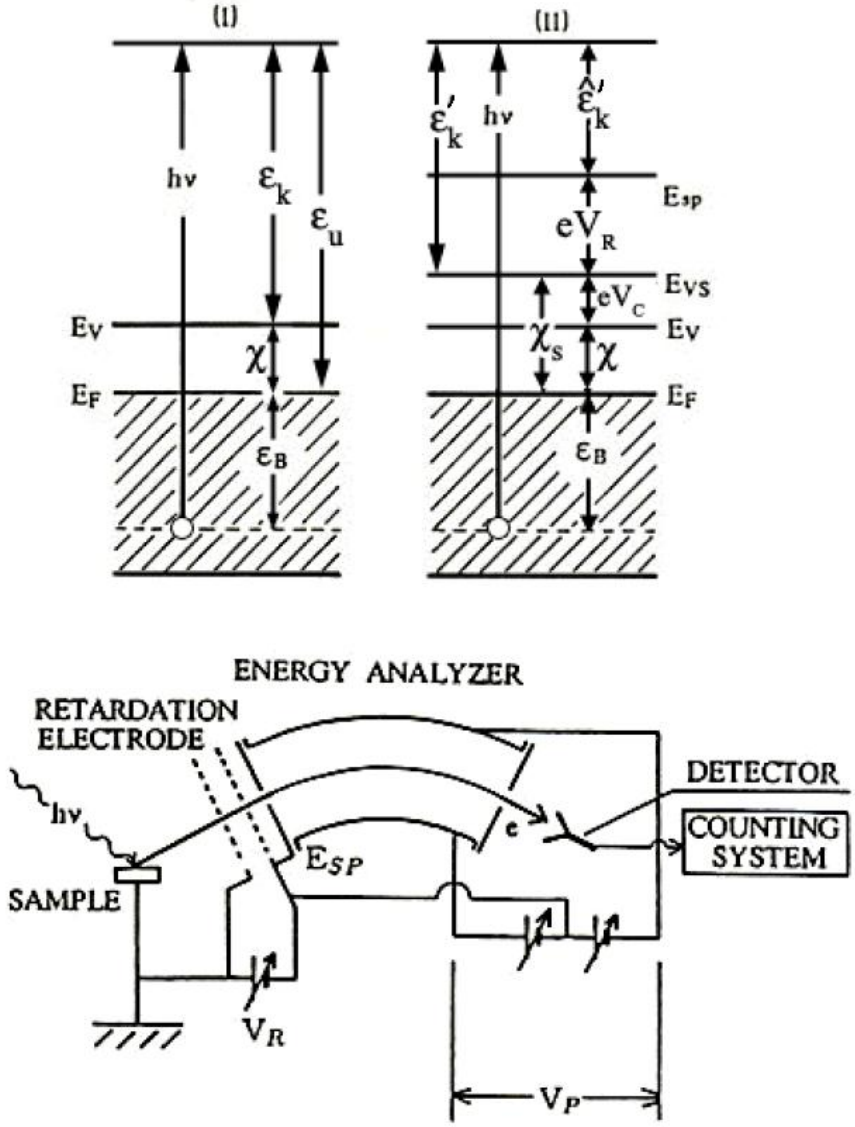

Fig. 2.22 Relation between the kinetic energy of a photoelectron in vacuum and that in the field of an electrostatic energy analyzer. (I): Energy in a sample. (II): Energy in an experiment arrangement. The part of an electron lens is illustrated as retardation electrodes (Ishii, 1989).

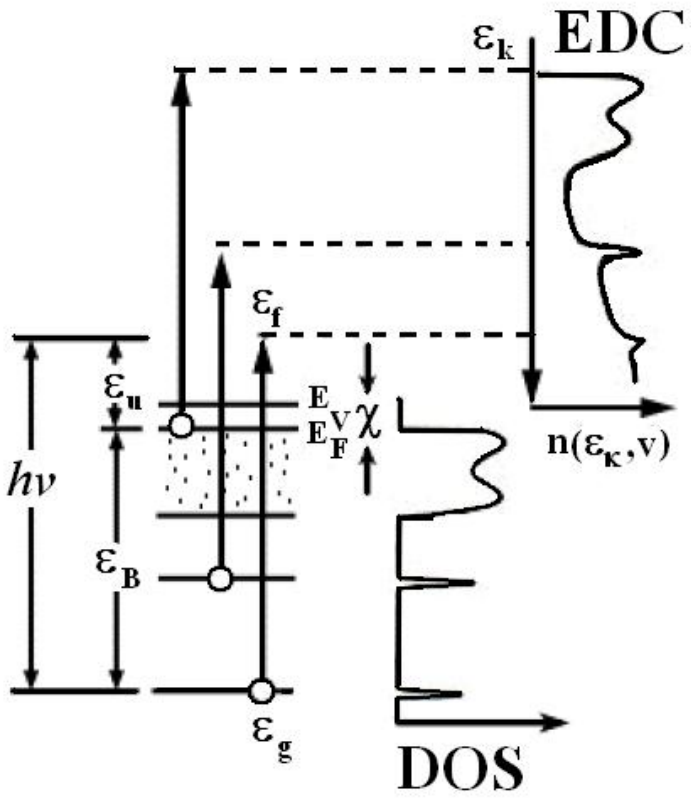

Fig. 2.23 Schematic illustration of photoelectron EDC, corresponding energy levels and the DOS curve. ε_f, ε_g, E_V and E_F are the energies for the final state, the initial state, vacuum level and Fermi level, respectively (Ishii, 1989).

2.3.6 Angle-Resolved Photoemission Spectroscopy (ARPES)

In angle-resolved photoemission, the number of emitted photoelectrons emitted in the direction (θ, ϕ), the polar and azimuthal angles, with respect to the normal to the sample surface and kinetic energy, ε_k , are analyzed. The photoelectrons are generated by monochromatic light of energy hv. The energy distribution curve in Fig. 2.23 shows that the primary photoelectrons are observed on the high-energy side of the energy distribution. Somehow they reflect their initial quantum state inside the solid at the detector in vacuum. The most prominent features are the peak of secondary electrons at low kinetic energy, which is due to cascade process created by the primary electrons. In the intermediate energy range, structures due to Auger electrons are observed.

The quantities we measure reflect the state of the electrons in the solid. If we measure the kinetic energy of a photoelectron and its emission direction, we can assign the momentum it has in the vacuum. Let the momentum be **p**. The problem is to obtain the photoelectron momentum inside the sample. From the equation (2.78), we have

$$\varepsilon_u = \varepsilon_k + \chi \tag{2.87}$$

Then the question is whether the electron is deflected when it passes through the surface. The practical assumption we may set up is that only the component of the momentum parallel , $\mathbf{p}_{\|}$, to the surface is conserved:

$$\mathbf{p}_{\|} = \hbar \mathbf{k}_{\|} \tag{2.88}$$

Thus, by measuring **p**, we obtain $\mathbf{p}_{\|}$ and $\mathbf{k}_{\|}$ from equation (2.88). Since $\mathbf{k}_{\|}$ is the wave vector of the photoelectron, then it is the momentum, $\mathbf{k}'_{\|}$, of the electron in the final state of the transition.

If we use equation (2.79) for the energy band case and the momentum conservation, we have

$$\varepsilon_{ck'} = \varepsilon_{vk} + h\nu \tag{2.89}$$

$$\mathbf{k}' = \mathbf{k} + \mathrm{K} \tag{2.90}$$

Here **K** is a reciprocal lattice vector. It should be point out that the EDC expressed as by equation (2.70) is further resolved as

$$n(\varepsilon_B, \mathbf{k}, \nu) = A\sum_{v} \left|\langle c, \mathbf{k}' | p_e | v, \mathbf{k}\rangle\right|^2 \delta(\varepsilon_{c\mathbf{k}'} - \varepsilon_{v\mathbf{k}} - h\nu) \tag{2.91}$$

$$\delta(\mathbf{k}' - \mathbf{k} - \mathrm{K})\delta(-\varepsilon_{v\mathbf{k}} - \varepsilon_B)$$

The constraints given in equations (2.89) and (2.90) are the bases for obtaining the energy band dispersion from ARPES.

Before we consider the practical procedure for drawing *E*-**k** curves, we have to a few important criterions.

1) **k** is originally defined in the reciprocal lattice space, but in practical, it is obtained in the coordinate system in real space. The factor exp(i**k**·**r**) in the Bloch function connects **k** and **r**.

2) The probability for the umklapp process must be small. Otherwise, electrons which are emitted in a specific direction has not unique **k**. Suppose, for

instance, photoelectrons with high energies just as the XPS case. Then, in the first Brillouin zone, there are many equi-energy surfaces $\varepsilon_{c,\mathbf{k}'}$ which have the same energy as ($\varepsilon_{v,\mathbf{k}} + h\nu$). Thus there are many cross lines between the equi-energy surfaces $\varepsilon_{c,\mathbf{k}'}$ and the equi-energy surfaces $\varepsilon_{v,\mathbf{k}}$. If we draw vectors from the original to these cross lines, we obtain wave vector $\mathbf{k}'$ satisfying the energy conservation given by equation (2.89). If we add various $\mathbf{K}$ to the vectors obtained above, we have the wave vectors $\mathbf{k}'$ satisfying both the energy and the momentum conservation. Since we have many equi-energy surfaces and $\mathbf{K}$, we may have different final state $\mathbf{k}'$ vectors occurring near the same direction. With a finite angular and energy resolution, different $\mathbf{k}'$ vectors being oriented comparatively closely cannot be resolved. Since there are many $\mathbf{K}$ involved in excitations by x-ray, XPS is practically angle-integrated photoemission. For small excitation energies, the transition matrix element occurring in equation (2.73) is small for the transitions in which $\mathbf{K}$ is not vanishing. If $\mathbf{K} = 0$, the number of $\mathbf{k}$ satisfying both equations (2.89) and (2.90) is limited, and ARPES makes sense. If we ignore the umklapp process, we have

$$k_{//} = \frac{1}{\hbar}\sqrt{2m\varepsilon_u}\,\sin\theta$$

$$= \left(0.51\,\text{Å}^{-1}\right)\sqrt{\varepsilon_u\,(\text{eV})}\sin\theta \qquad (2.92)$$

where θ is the polar angle determining the direction of the photoelectron. Since ε_B is equal to $-\varepsilon_{v,\mathbf{k}}$, we have from equations (2.78) and (2.89)

$$\varepsilon_{v,\mathbf{k}} = \varepsilon_u + \chi - h\nu \qquad (2.93)$$

If we plot $\varepsilon_{v,\boldsymbol{k}}$ obtained from equation (1.100) versus $\mathbf{k}_{\|}$ obtained from equation (2.92), we obtain the dispersion of the energy band as

$$\varepsilon_{v,\mathbf{k}} = \varepsilon_{v}\left(\mathbf{k}_{\|}\right) \tag{2.94}$$

In the case of materials with the two dimensional symmetry, $\mathbf{k}_{\perp}$ is not a good quantum number and the results obtained as equation (2.94) are the goal of the experiments.

ARPES is quite useful for the two dimensional energy band. On the other hand, the dispersion of the three dimensional band cannot be obtained without making further assumptions, since the component of **k** normal to the crystal surface is not known from experimentally observed momentum, **p**, of the photoelectron in the free space. A model that proved to work well empirically is to adopt the energy free electron approximation for the excited photoelectron. Then, the kinetic energy is given as

$$\varepsilon_{u} = \frac{(\hbar k)^2}{2m} - E_0 \tag{2.95}$$

where $-E_0$ is the potential energy of the interior of the crystal referenced to the Fermi level. If we rewrite equation (2.95) using the measurable energy, we have

$$\frac{(\hbar k)^2}{2m} = \varepsilon_{k} - \left(E_0 + \chi\right) \tag{2.96}$$

$$= \varepsilon_{u} + V_0 \tag{2.97}$$

where V_0 is the crystal potential referenced to the vacuum level. Fig. 2.24 schematically illustrates the dispersion of the energy band in the approximation described above. The band above the vacuum level is approximated by the nearly free electron band. If we find photoelectron with a kinetic energy $p^2/2m$, this is equal to $\varepsilon_{\mathbf{k}}$; the electron is in the nearly free electron level given by equations (2.95) and (2.97). In this model, combining equations (2.92) and (2.96), we have

$$\mathbf{k}_{\perp} = \frac{1}{\hbar}\sqrt{2m\left(\varepsilon_k \cos^2\theta + V_0\right)} \tag{2.98}$$

$$= \left(0.51 \overset{\circ}{\mathrm{A}}^{-1}\right)\sqrt{\left(\varepsilon_k \cos^2\theta + V_0\right)} \tag{2.99}$$

Using equations (2.92), (2.93) and (2.99), we now have $\mathbf{k}_{||}$, $\mathbf{k}_{\perp}$, and $\varepsilon_{v,\mathbf{k}}$ expressed in terms of measurable quantities. Thus, if we find V_o appropriately, we can depict the dispersion curve

$$\varepsilon_B = \varepsilon_v(\mathbf{k}) \tag{2.100}$$

In the energy band calculation, the dispersion relation is usually calculated along an axis with specific symmetry. It is rather complicated to select θ and hv to obtain $\mathbf{k}$ with specific symmetry. A few methods have been developed so far, but we do not discuss them any further here.

If synchrotron radiation is used as excitation light, the excitation energy is tunable and this is conveniently utilized to obtain the dispersion curve. In this method, only photoelectrons emitted normal to the crystal surface are collected. Then, $\mathbf{k}_{||} = 0$ and $\theta = 0$, and we have, from equations (2.98) and (2.99)

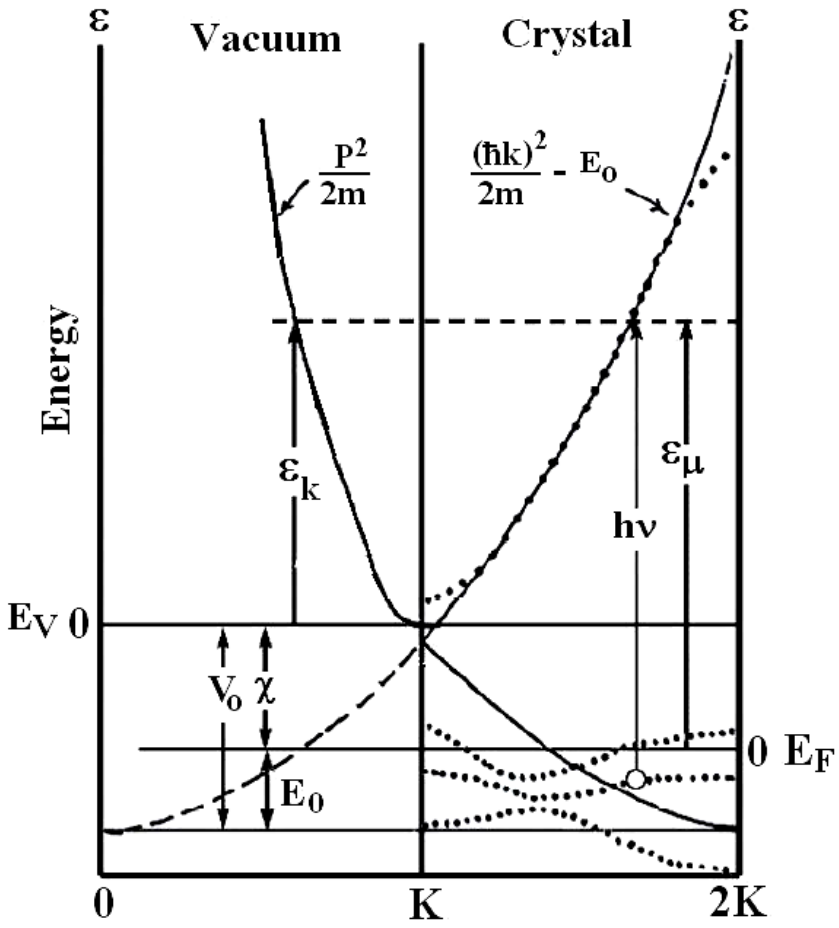

Fig. 2.24 Energy dispersion in the nearly free electron model for photoelectrons in ARPES. The right half represents the energy levels in a crystal. Curves illustrated by dots are energy-bands. Full lines are energy-band for the nearly free electron model. The left half represents the energy levels outside the crystal. **K** is a reciprocal lattice vector. $h\nu$: Photon energy. χ: work function. ε_u: Kinetic energy in the crystal. ε_k: Kinetic energy is a free space. E_F: The Fermi level. E_V: Vacuum level. V_0: Crystal potential (Ishii, 1989).

$$k_{\perp} = \frac{1}{\hbar}\sqrt{2m(\varepsilon_k + V_o)} \tag{2.101}$$

$$= \left(0.51 \text{Å}^{-1}\right)\sqrt{(\varepsilon_k + V_o)} \tag{2.102}$$

If a sample is cut so that an important symmetry axis of the crystal lies along the direction normal to the crystal surface, $\mathbf{k}_{\perp}$ give **k** along this symmetry axis. If the energy of excitation light is changed, ε_k changes. Thus using equation (2.93), $\varepsilon_{v,\mathbf{k}}$ is obtained. On the other hand, **k** is obtained from equation (2.101). Thus we obtain the dispersion relation given as equation (2.100).

2.3.7 Parity Determination

ARPES measurements can determine not only the dispersions but also the symmetry of surface states with respect to the mirror axes of a surface Brillouin zone (SBZ), which is another important physical property of a surface state. It is due to the well known symmetry selection rule of a dipole transition, where the transition probability is proportional to $\langle f|\mathbf{A}\cdot\mathbf{p}|g\rangle$, where $|g\rangle$ and $\langle f|$ are the initial and final states wave function, respectively. **A** is the vector potential of incident photon and **p** is the momentum operator.

Here we have to point that the transition moment is also expressed as $\langle f|\mathrm{E}\cdot\mathbf{r}|g\rangle^2$ in which **E** is the electric vector of excitation light. Furthermore **A** is parallel to **E**. The parity of **r** can be assigned easily. $\langle f|\mathbf{A}\cdot\mathbf{p}|g\rangle^2$ is equivalent to $\langle f|\mathrm{E}\cdot\mathbf{r}|g\rangle^2$ other than an unimportant factor including energies as far as the parity

problem is concerned. Also, the small escape depth is important for the concept described above. Furthermore, it is **E** that is incident on a material. **A** is defined as **H** = rot **A**. In spite of the situation described above, we will discuss the parity of the transition moment in term of **A**·**p** in an abstract way in what follows.

The symmetry of an initial state with a definite symmetry can be selected by the symmetry of **A** as well as those of $\langle f | \mathbf{p}$; if **A** is even for a given mirror plane only even symmetry of $\langle f | \mathbf{p} | g \rangle$ is excited and vice versa. To secure definite symmetry for **A**, it is needed to use linearly polarized light and particular geometrical conditions for the measurements. The former is made possible by using the synchrotron radiation as the photon source in ARPES. Synchrotron radiation is inherently polarized. The latter, the geometrical set-up is as follows.

In order to determine the symmetries, two difference measurement geometries, denote as $\mathbf{A}_+$ and $\mathbf{A}_\pm$, are used (Fig. 2.25). In the former geometry $\mathbf{A}_+$, the detector is arranged so that photoelectron emission always occurs in the plane defined by the surface normal $\hat{n}$ of the sample and the incident light whose polar angle θ_i from surface normal is fixed. In the present work, the angle is selected as 20^o. Since the linear-polarization vector **E** thus the vector potential **A** of incident synchrotron radiation is always in the plane of emission in this geometry, only the electronic states with even symmetry are excited for a scan along a mirror axis. If not specified in this thesis, a ARPES scan was done in this geometry.

On the other hand, in the latter geometry, $\mathbf{A}_\pm$, the emission is kept in the plane, which contains $\hat{n}$ and is perpendicular to the plane defined for $\mathbf{A}_+$ geometry. If θ_i is zero in this symmetry, **E**(**A**) is always orthogonal to the plane of emission, thus only

the odd-symmetry states can be excited. However, since the actual measurement situation made this condition impossible, θ_i was fixed at 20^o and both even-and odd-symmetry states are excited in the geometry $\mathbf{A}_{\pm}$. Finally through the comparison of spectra taken along a mirror symmetric axis in these two different geometries, we can determine the symmetries of each surface state.

For this experiment, we use synchrotron radiation, which is linearly polarized light. We can identify the initial state symmetry by employing polarized radiation and the dipole selection rule. If **A** is parallel to the crystal surface, the initial state with only odd symmetry will be excited. This can be achieved by an incident angle of light of 20° respect to the surface normal. The polarized light in this case is called s-polarized light. Otherwise, if **A** is perpendicular to the surface by an incident angle of 60°, the initial state with even or odd symmetry will be excited. This means that the initial state is excited with sp-polarized light. The dipole selection rule in normal emission mode is summarized in Table 2.3

2.4 Computational electronic structure calculation

A numerical calculation helps us analyzing the experimental results. According to the advance of computer technology, first-principle methods have been performed to calculate the electronic structure of materials. Although first-principle methods are based on many assumptions to solve Schrödinger equation, there are two categories; one is cluster method calculating the electronic structure in a part of crystal and the other is band method calculating that in a whole crystal. Each method has a different advantage based on a periodicity of crystal potential and a basis of wave function.

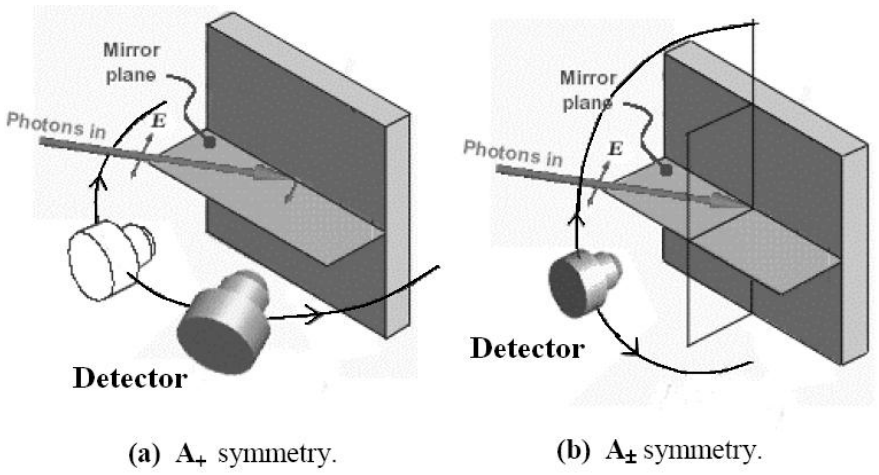

(a) A_+ symmetry. (b) $A_\pm$ symmetry.

Fig. 2.25 Schematic illustration of the ARPES measurement geometries with polarized light.

Table 2.3 Dipole selection rule using linear polarized light coming to single crystal surface. (Hermanson, 1977).

Normal emission (nonrelativistic)				
Crystal plane	Final state	Allowed initial state		
(100)	Δ_1	$\mathbf{A} \parallel [001]$	$\mathbf{A} \parallel [010]$	$\mathbf{A} \parallel [100]$
		Δ_5	Δ_5	Δ_1
(110)	Σ_1	$\mathbf{A} \parallel [001]$	$\mathbf{A} \parallel [0\bar{1}0]$	$\mathbf{A} \parallel [110]$
		Σ_3	Σ_4	Σ_1
(111)	Λ_1	$\mathbf{A} \parallel [\bar{1}10]$	$\mathbf{A} \parallel [\bar{1}\,\bar{1}2]$	$\mathbf{A} \parallel [111]$
		Λ_3	Λ_3	Λ_1

2.4.1 Cluster model

Cluster methods are useful to calculate the electronic structure in a cluster separated from a crystal. The electronic structure of the cluster can be calculated on the basis of molecular orbital or linear combination of atomic orbitals (LCAO). This method has an advantage on the calculation on localized wave functions in symmetry-breaking crystals, since no periodic potential is assumed. Especially, molecular-orbital calculation provides information on chemical bonding between atomic orbitals (See Appendix A).

In this thesis, the discrete-variational (DV) Xα molecular-orbital method based on the self-consistent Hartree-Fock-Slater model is applied to calculate the surface and interface electronic structures (Adachi, Tsukada and Satoko, 1978). Numerical basis functions are utilized in this calculation. Self-consistent iteration process is illustrated in Fig. 2.26.

In 1951, α parameter was introduced by J. C. Slater as an adjustable parameter for exchange-correlation energy (Xα potential) in the transition-metal calculation. Later, α parameter for exchange potential was found to be 2/3 = 0.666666 on the basis of local density approximation (LDA). In the present DV-Xα method, α parameter is fixed at 0.7, since correlation potential is considered as 0.0333333.

2.4.2 Band model

Band methods are useful to calculate the electronic structure in a whole crystal. This method has an advantage on the calculation of the energy-band structure of a perfect crystal. The basis of wave function such as a plane wave is applied in the calculation. Density functional theory (DFT) is one of the most widely used methods

for"*ab initio*" calculations (Argaman, www, 1999). A detailed energy-band theory is already described in Section 2.1.1 and fundamental formulae of DFT are summarized in Appendix B.

In this thesis, the energy-band calculation using the Vienna *ab-initio* simulation package is performed to calculate the surface and interface energy-band structures (Kresse and Hafner, 1993).

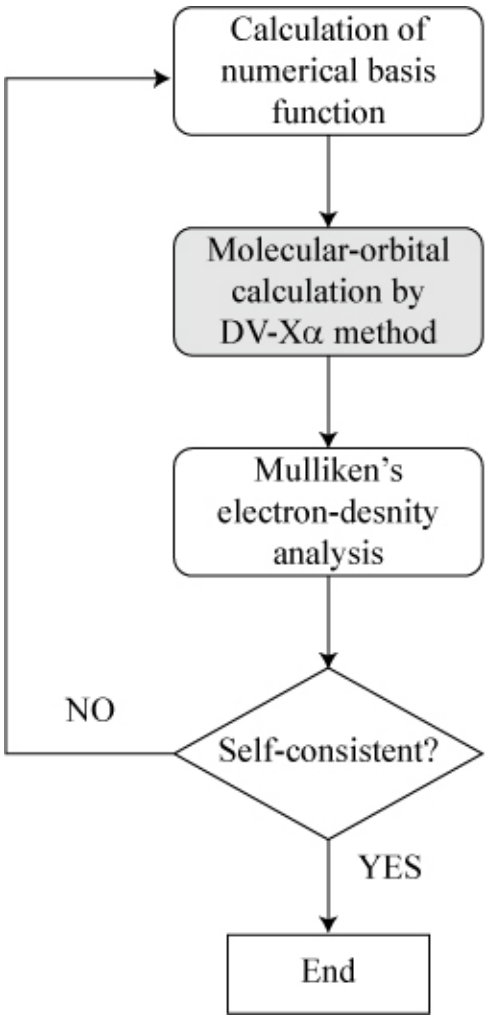

Fig. 2.26 Iteration process of DV- Xα method (Adachi, Tsukada and Satoko, 1978).

CHAPTER III

EXPERIMENTAL

This chapter describes the experimental instruments and procedures used in this thesis work. First, the experimental instruments are described. Explanations are made on the element located along the beamline. Then, the preparation of the sample and practical experimental procedure are mention. Finally, the detail of estimation the amount of oxygen on the surface is described.

3.1 Experimental Instruments

The experiment was performed in the BL-4 of the Siam Photon Source of the National Synchrotron Research Center of Thailand that was constructed for solid state spectroscopic research and related phenomena. The beamline delivers photons with energy between 20 eV and 240 eV. The detailed descriptions of the beamline were reported elsewhere (Prayoon Songsiriritthigul, Weerapong Pairsuwan, T. Ishii and A. Kakizaki, 2003; Prayoon Songsiriritthigul *et al*., 2004). The experimental station includes a multi-UHV-chamber system, as shown in Fig. 3.1. The essential part of the multi-UHV-chamber system is the sample transfer system, which consists of grips, mechanical hands, transfer rods and linear and radial sample transporters. With the transfer system, samples can be transferred among different UHV chambers providing the possibility for *in-situ* studies. The VG R2D2 radial sample transporter has six

connecting ports, allowing up to six UHV chambers to be connected. Currently, four ports are used to connect with the old photoemission system, an additional XPS system, a metal MBE system and a load-lock system. Between the photoemission system and the radial transporter, the VG DB2DD linear sample transporter is used to provide sufficient working space. The vacuum environment of each system can be isolated by closing the gate valves, which are installed between each system and the radial transporter (Nakajima *et al*., 2007). Samples may be introduced into the multi-UHV-chamber system without breaking UHV conditions via two different directions, i.e. via the load-lock chamber connected to the radial transporter or via the load-lock chamber of the XPS system.

One of all, a multi-UHV-chamber system of the BL4 is a photoemission system shown in Fig. 3.2. Both angle-resolved and angle-integral photoemission experiments can be performed. The photoemission system consists of two main ultra-high vacuum (UHV) chambers, *i.e*., a preparation and analysis chambers. The monochromatized light beam, small spot, is focused on the sample surface. The way of light is pass from entrance slit of a monochromator with a toroidal mirror. The monochromator is of a vertical dispersion type and equipped with plane gratings of non-linear groove spacing. By using three gratings with average groove spacings of 300 lines/mm, 600 lines/mm, and 1200 lines/mm, optical measurements can be carried out over the range from $h\nu$ = 20 eV to 240 eV. An intermediate slit and a focusing mirror are installed between the incident slit and the grating. A rear mirror focuses monochromatized light to the photoemission chamber.

Angle-integrated energy distribution curves (EDC's) of photoelectrons and Auger electrons were measured with a Thermo VG Scientific CLAM2 energy

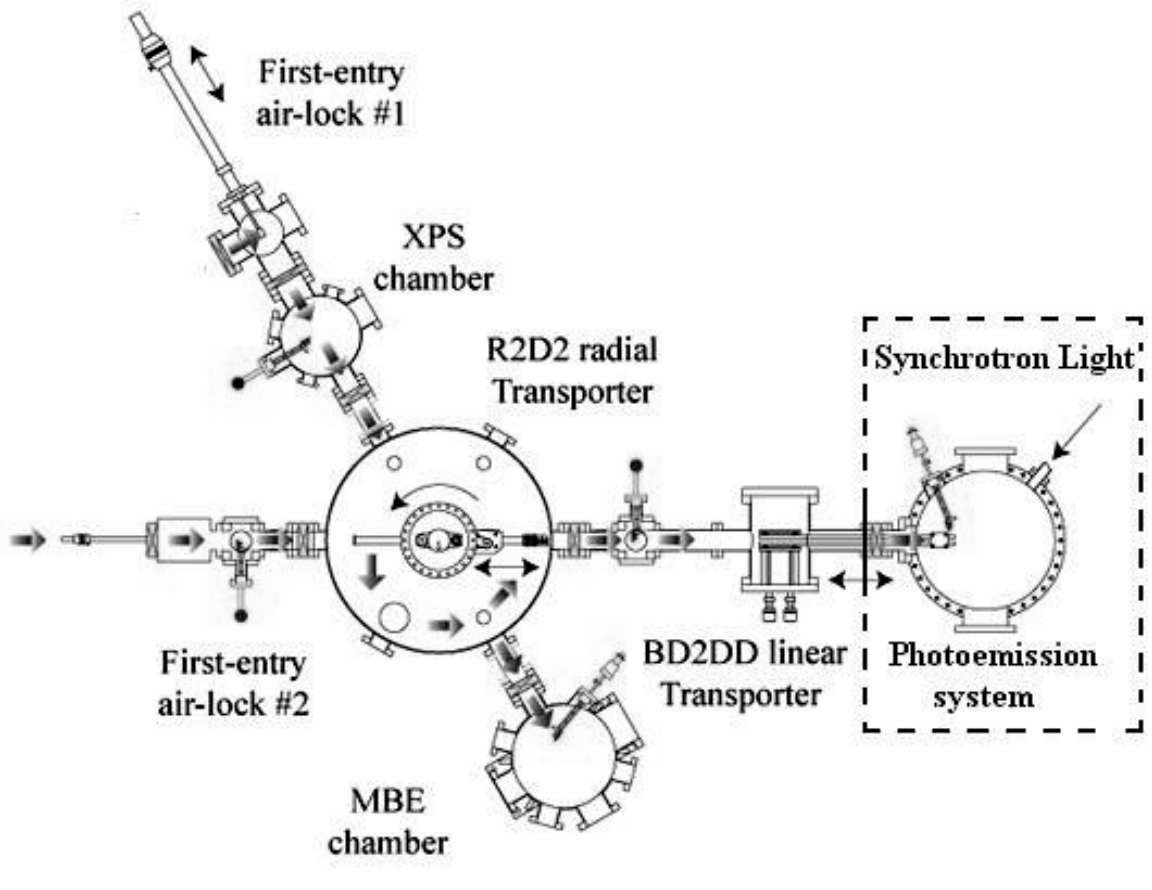

Fig. 3.1 Schematic diagram of the new experimental station of the BL4 beamline at Siam Photon Laboratory (www, 2006).

analyzer. For angle-resolved EDC measurements, a hemispherical analyzer of a different type is also installed in the analyzer chamber. The angle-resolved EDC's will be reported in this thesis.

3.1.1 UltraHigh Vacuum System

The UHV system used in the experiments was equipped with a rotary pumps turbomolecular pumps and ion pump combined titanium sublimation. The rotary pump is used for rough evacuation of the system. It reduces the system pressure sufficiently to allow the turbomolecular pump to operate and follow with ion pump. Photoemission measurements have to be performed in a UHV environment. With modern vacuum technology, a proper-designed vacuum system can reach vacuum pressure in a range of 10^{-11} mbar or better. Only such a low pressure will convince that a surface stays clean for a time long enough to do some experiments. Table 3.1 shows a time to get a monolayer on the surface. According to this table, the vacuum at the order of 10^{-11} mbar is needed for surface study.

A vacuum chamber is made by stainless steels (commercial 304 or 316LN). These materials have a strong hardness, high cleanliness, low-magnetic permeability, and high melting point (Thermo Vacuum Generators catalogue, www, 2006). The vacuum system must not only be pumped properly but it must be free of true and virtual leaks. The latter rise from gases, especially water, adsorbed by the internal chamber walls and instruments.

At room temperature these will slowly be desorbed resulting in a large virtual leak which can continue for years. These are eliminated for at least one day by baking

Fig. 3.2 Photoemission system at the experimental station of the BL-4 beamline.

the whole system, typically at 150-200°C. Baking of the systems is essential to remove adsorbed gas molecules on the interior surface vacuum chamber and the surface of tools in the vacuum system. For baking, whole vacuum chambers were contained in a box, the walls of which are made of thermal insulators and heating elements were contained in this oven-like shroud as illustrated in Fig. 3.3. It is essential to leave the whole chamber at the required temperature for sufficiently long time even after the temperature is reached over all internal surfaces. By doing this, we can avoid condensation of residual gas molecules in cooler regions. Following baking, degassing of the sample and filament parts is needed. The heating of the sample is made by electron bombardment of the sample holder for a short time. This procedure is often referred to a flash baking. Degassing of filaments is performed just by flowing current on filaments.

After UHV is achieved, the analysis of residual gases shows that they consist of gases that are not main atmospheric constituents. The dominant residuals are usually H_2, H_2O, CO and CO_2. Generally, two kind of total pressure gauge are used. Penning gauge detects an ion current ionized by strong magnetic and electric field in a part of chamber. Pirani gauge measures a current of the heat wire, because temperature of the wire decreases as a function of the number of scattering atom on the wire. Penning gauge and pirani gauge are used to be for high vacuum and low vacuum, respectively. The more sophisticated gauge is called the ion gauge which works using filament to ionize atoms. It is used for the measurement of UHV only. We measure a partial pressure in the chamber by using “Residual gas analyzer” (RGA) to check vacuum leak and quality of introducing gas.

Photoemission system is of two chambers vacuum-isolated by a gate valve as illustrated in Fig. 3.4. The availability of the preparation system allows *in-situ* analysis of samples treated in the preparation system. UHV environment is essential as photoemission is a surface sensitive technique. Two ion pumps and two titanium sublimation pumps are used to obtain UHV in the preparation and analysis chambers with typical based vacuum pressure of ~2×10^{-10} mbar. A turbo-molecular pump is used for extra pumping during cleaning surface of samples and for loading samples into the analysis chamber. The analysis chamber is connected to the end of the BL4 via a line-of-sight valve. This provides possibility to disconnect the experimental station from the beamline without breaking the UHV condition.

Table 3.1 Pressure ranges used in vacuum (Thermo Vacuum Generators catalogue, www, 2006).

	Rough Vacuum	Medium Vacuum	High Vacuum	Ultra high Vacuum
Pressure range in mbar	10^{3} ~1	1~10^{-3}	10^{-3}~10^{-7}	< 10^{-7}
Particle number in cm^{-3}	10^{23} ~10^{20}	10^{20} ~10^{13}	10^{13} ~10^{9}	< 10^{9}
Mean free pass in cm	< 10^{-2}	10^{-2}~10	10~10^{5}	>10^{5}
Monolayer time in sec.	< 10^{-5}	10^{-5} ~10^{-2}	10^{-2} ~100	>100

Fig. 3.3 Baking of the photoemission system by thermal insulators box.

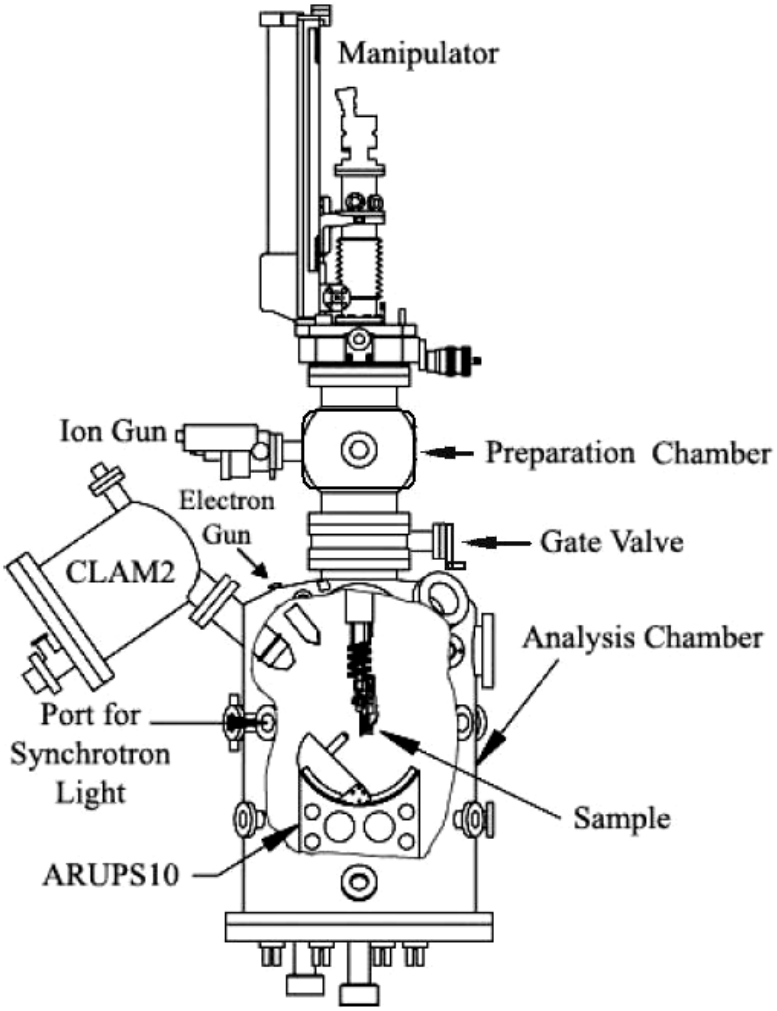

Fig. 3.4 Schematic diagram of the photoemission system. CLAM2 and ARUPS10 energy analyzers are the main instruments.

3.1.2 Sample Holder and Manipulator.

The sample holder system was attached to the bottom of manipulator arm. It was made from molybdenum and designed as compact as possible to hold Ni. The manipulator consists of a three-axis positioning XYZ translation, the polar rotation (θ) of the sample, and a sample stage capable of azimuthal rotation (φ) of the sample. Normally manipulator is used to position and align the sample with respect to the angle of the incidence of excitation light and the angle of emission of photoelectron. The manipulator is also equipped with heating and cooling facilities to control the temperature of the sample. Heating of sample can be done by electron bombardment. Electrons from the filament impinge the sample and activate the impurity removing from the surface of the sample. The sample temperature was measure by thermocouple and a pyrometer. Molybdenum was chosen as the materials of sample holder. The reason is that their thermal conductivity is low. This is important to avoid heat conduction away from the sample when the sample is flash heated. The sample holder and manipulator is shown in Fig. 3.5. However, we should be degassed the sample holder at high temperature, 800-900°C, before load to the UHV system.

3.1.3 Low Energy Electron Diffraction (LEED)

Low energy electron diffraction (LEED) is the oldest diffraction technique applied to the study of surfaces dating back to Davisson and Germer's experiments of electron scattering from nickel (Davisson and Germer, 1927). Today LEED is used in one of two basic ways. Its most common use is as a tool to study the structural arrangement of atoms within the surface unit cell (Ertl and Kuppers, 1985). With the introduction of higher quality electron sources and electron detectors, LEED is now also used as a quantitative probe of surface long-range order and 2-dimensional phase transition.

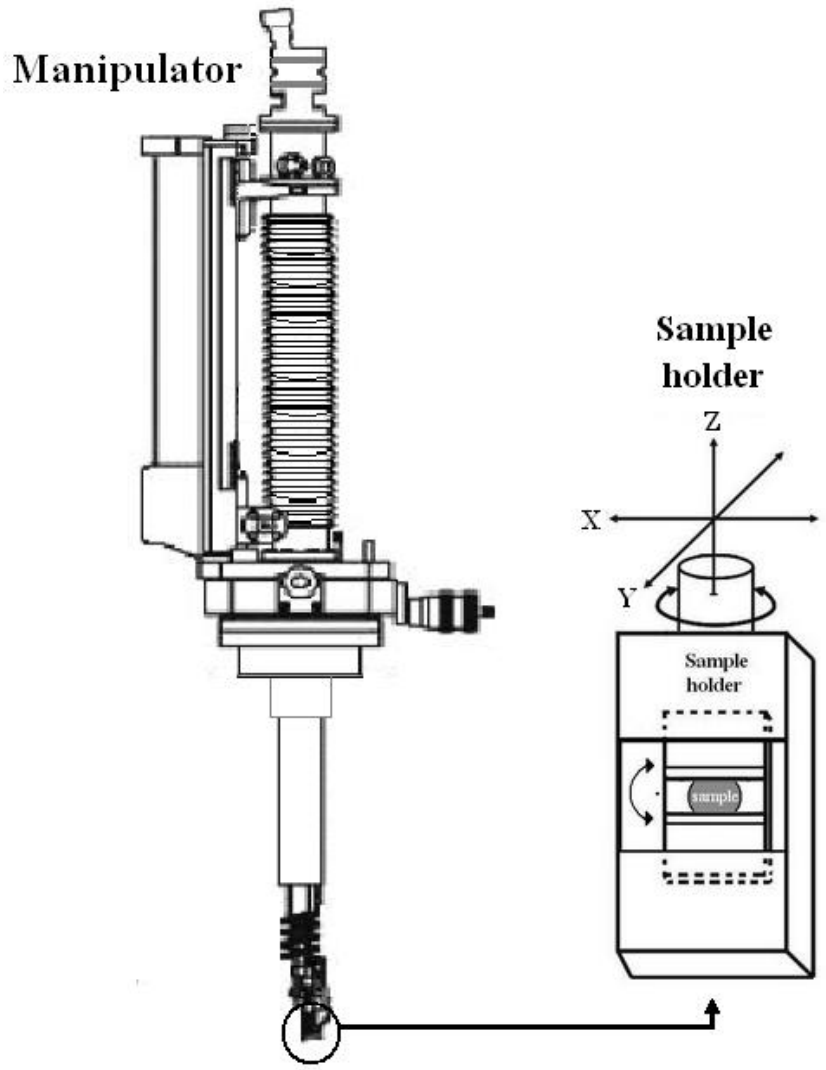

Fig. 3.5 Schematic diagram of the sample holder and manipulator

The surface sensitivity of LEED is derived from the strong interaction of medium to low energy electrons with the conduction electron in the solid. To see this consider an electron of energy as it passes through a solid. A schematic plot of mean free path and electron energy is shown in Fig. 3.6. For most materials, mean free path reaches a minimum of about 20 Å near 100 eV (Quinn, 1962). This means that an electron beam with this energy will be severely attenuated by the time it has passed through only a few crystal planes (the spacing between planes is 3 Å). The surface sensitivity of the electrons is now obvious. An electron of energy that passes through the solid and is subsequently detected at the same energy must have been scattered from the top few layers of the solid. The probability that this electron came from deeper in the bulk is very low since it would most likely have suffered an inelastic scattering event before reaching the detector. Experimentally, the detector energy resolution need only be a few eV to successfully discriminate electrons originating in the surface layers from those originating in the bulk. This is because energy losses of 10 to 100 eV are typical after an electron traverses a single mean free path.

An electron beam incidents on a solid, with primary energy will produce a distribution of electrons near the surface due to elastic and inelastic collisions with electrons in the solid. Some of these electrons will be backscattered from the surface. A typical energy spectrum for these backscattered electrons is given in Fig. 3.7. The broad peak below 50-100 eV is due to electrons that have suffered many losses due to single particle interactions with electrons in the bulk as well as those ejected from valance states. These electrons are referred to as the true secondaries. At higher energies, small fluctuations in the secondary electron spectrum appear. These electrons are the Auger electrons produced during the de-excitation of ionized core

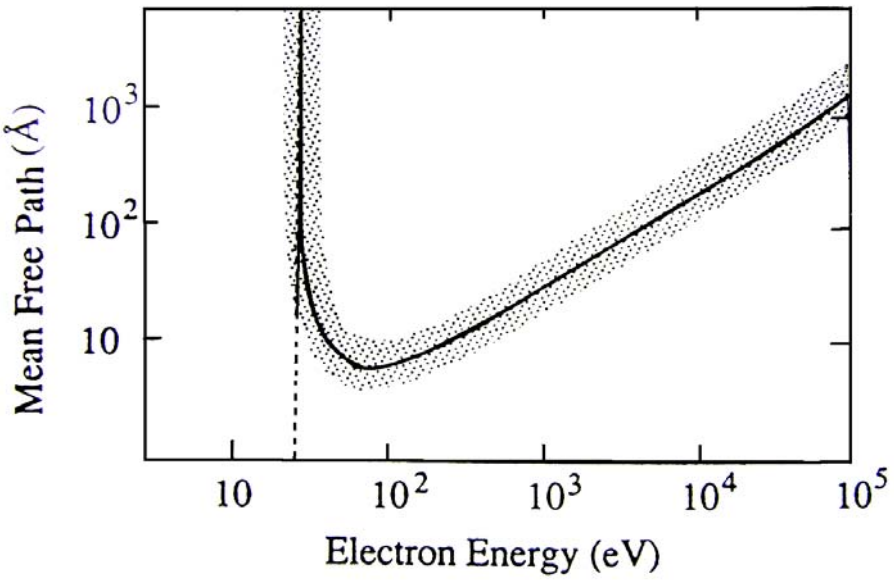

Fig. 3.6 A schematic plot of mean free path and electron energy(Quinn, 1962).

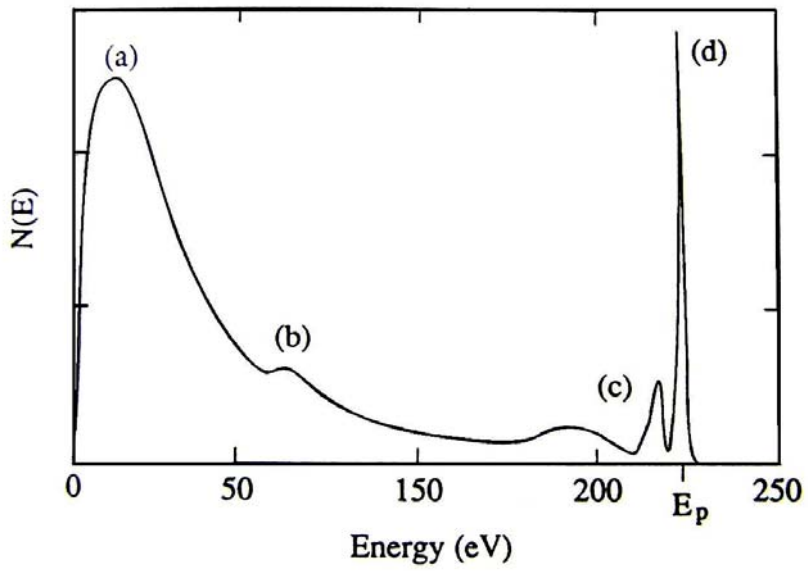

Fig. 3.7 The energy distribution of emitted electrons from a target bombarded by electrons with primary energy E_p. (a) the true secondary electron peak; (b) Auger electrons shown in an exaggerated scale; (c) plasmon and interband losses; (d) elastic scattered electron (Rudburg, 1930).

holes caused by the incident electron beam. LEED used electrons with energies typically in the range of 20-500 eV. An electron with energy has a wavelength given by the de Broglie relation

$$\lambda(\text{Å}) = \frac{\text{h}}{\sqrt{2 \cdot KE \cdot m_e}} = \sqrt{\frac{150.4}{KE(\text{eV})}} \tag{3.1}$$

The wavelength given by equation (3.1) refers to the wavelength measured in vacuum. With incident energy from 30-300 eV, they have a wavelength given by the de Broglie relation which varies from 2.7 Å to 0.5 Å in this case. This first nicely into the range of distances between atoms in solids and can therefore strongly diffract from them. The recording and analysis of the diffraction pattern can tell us the arrangement of the atoms on the surface. The sharpness of the pattern is related to the extent of order of the atoms on the surface.

Fig. 3.8 shows a schematic diagram of the experimental setup for LEED measurements. The instrument is a Thermo VG Scientific RVL-900 rear view LEED incorporating the LEG24 high current miniature electron gun. The electron gun can be operated over the energy range from 5 to 100 V for LEED measurements. Electrons are thermally emitted from a hot tungsten filament. The electrons are focused by a small lens onto the sample surface, which is at the center of several concentric hemispherical grids. The sample diffracts the electron beam and generates diffracted electron beams from the surface. The diffracted electron beams hit a fluorescent screen and form some bright spots on the screen. The grid system is for focusing the diffracted electron beams. The diffraction pattern formed in this way is recorded by a CCD camera and used for the surface atomic structure analysis.

3.1.4 Auger Electron Spectroscopy (AES)

Auger electron spectroscopy (AES) was used in this work to examine some contaminate and impurities on the surface of nickel such as carbon and oxygen. AES is based on the Auger effect that discovered by L. Meitner and P. Auger in 1923. The origin and nature of the Auger process can be understood from the diagram of the electron energy level as shown in Fig. 3.9. Ionizing radiation ejects an electron from an atom in the solid, leaving a hole in one of the atomic core levels. An electron from a higher level shell quickly fills this core level and energy is released. This energy can leave the atom in the form of X-ray fluorescence, or there can be a competing process where another electron gains the energy and is ejected from the atom. This second ejected electron is the Auger electron and its energy depends on the energy of the atomic level involved in its production, not on the energy of the initial ionizing radiation. The energy of the Auger electron can therefore be used for element analysis. Only H and He do not give rise to Auger electrons as two electron shells are needed. Although Li has only one electron per atom in the *L* shell it can share its valence electron in a solid. The energy of Auger electron emitted from a solid surface is largely determined by the binding energies of the atomic energy levels in the participating atom. There are also contributions to the Auger electron binding energy from the screened Coulomb interaction of the final state holes, and relaxation of the surrounding electrons. This relaxation involves both the electrons in the atom itself and in the surrounding material.

The nomenclature used to describe an Auger transition is derived from X-ray terms. The inner electron shell being the K, and higher shells being L, M, N, O and V are used to denote valance states. For example the strong carbon KLL Auger feature

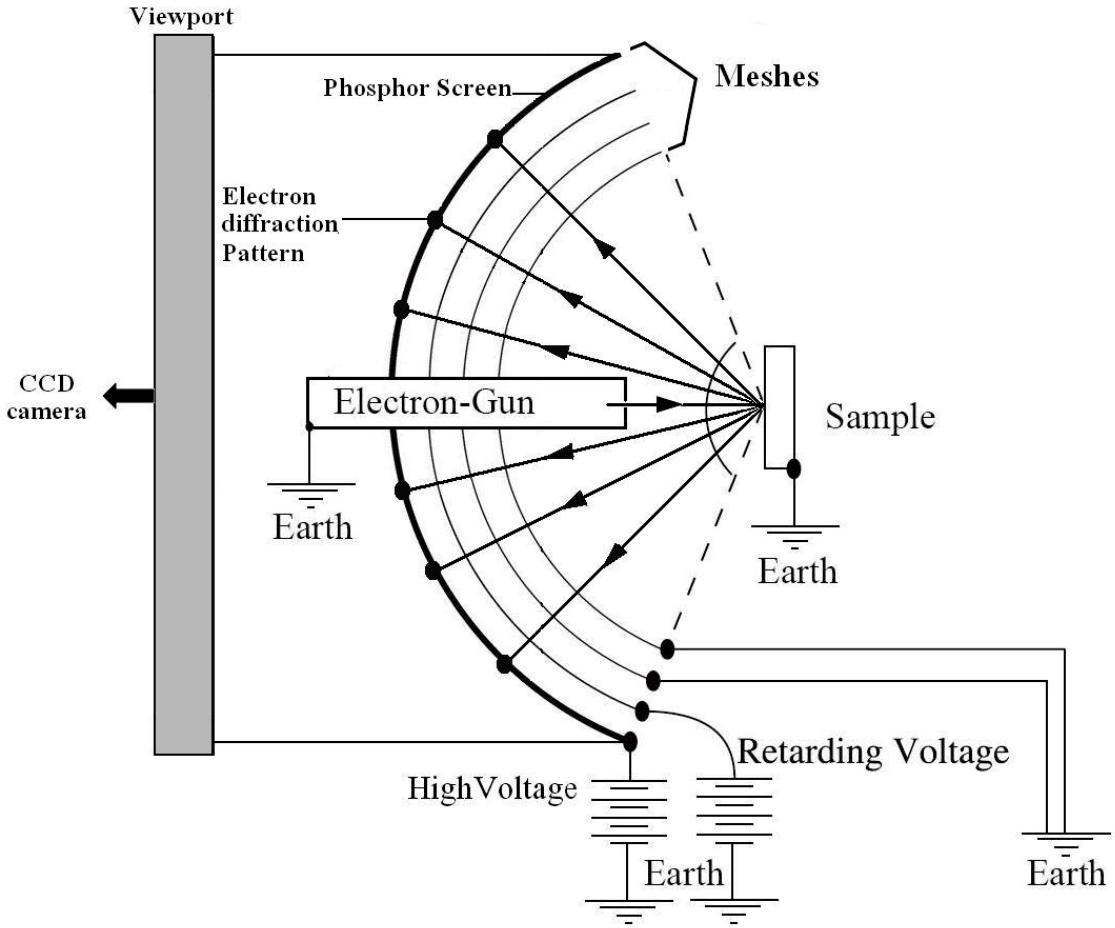

Fig. 3.8 Schematic diagram of rear view LEED setup.

around 273 eV is formed by an initial ionization of the inner K shell 1s electrons. The valance electrons of the carbon atom are in the two-L shells. One valence electron fills the K shell hole and the other ejected as an Auger electron. The carbon spectrum is very sensitive to the chemical environment and the density of states that the valence electrons occupy. The Auger transition nomenclature can be made more rigorous by including with the X-ray terms, the partial terms for the angular momentum. For s, p and d the terms 1, 2, 3, 4 and 5 are used, *e.g.* KL_1L_2.

The AES system consists of an ultrahigh vacuum system, an electron gun to bombard the sample surface and an electron energy analyzer to collect and analyze the secondary electron distribution. In this work we use a hemispherical analyzer as the electron energy analyzer. This analyzer consists of an input lens, and two concentric hemispheres forming a condenser-like structure. Electrons from the sample are focused by the input lens onto a slit at the entrance of the field of the hemispheres. A potential difference between the hemispheres is arranged to give a $1/r^2$ field, and electrons with the correct energy are focused into a slit at the exit of the hemispheres. The resolving power of the analyzer is determined by the slit size, the mid hemisphere radius, and the entrance angle. However, the resolving power of the total system can be changing the input lens retardation. This gives the hemispherical analyzer great flexibility and high-energy resolution.

Auger spectra are normally displayed in one of two ways. The direct spectra is the relation of ε versus $N(\varepsilon)$ where ε is the Auger electron energy. However, the derivative spectra, $d[N(\varepsilon)]/d\varepsilon$, as shown in Fig. 3.10 has been preferred. The direct Auger spectrum consists of weak emission band that overlaps a huge broad background band. Thus, the real emission band cannot be easily resolved. If the

derivative curve is plotted, the broad background band that obscures the Auger emission band is eliminated and the Auger band is clearly recognized as the derivative form.

3.1.5 Ion Gun

The ion gun is an instrument for the sample cleaning by ion sputtering technique. The EX03 from Thermo VG Scientific (U.K.) was used in this thesis work. The gases species can be used for this model of ion gun are Ar, Ne, Kr, and Xe. Ar gas was selected for the sample cleaning processes. The energy of the gun can be varied between 300 eV to 3 keV. The Ar gas can be fed into the ion gun via a high-precision leak valve. The working distance is 100 mm but it can be in the range of 50-200 mm. The operating pressure should be less than 1×10^{-5} mbar. A simple sketch of ion gun is shown in Fig. 3.11.

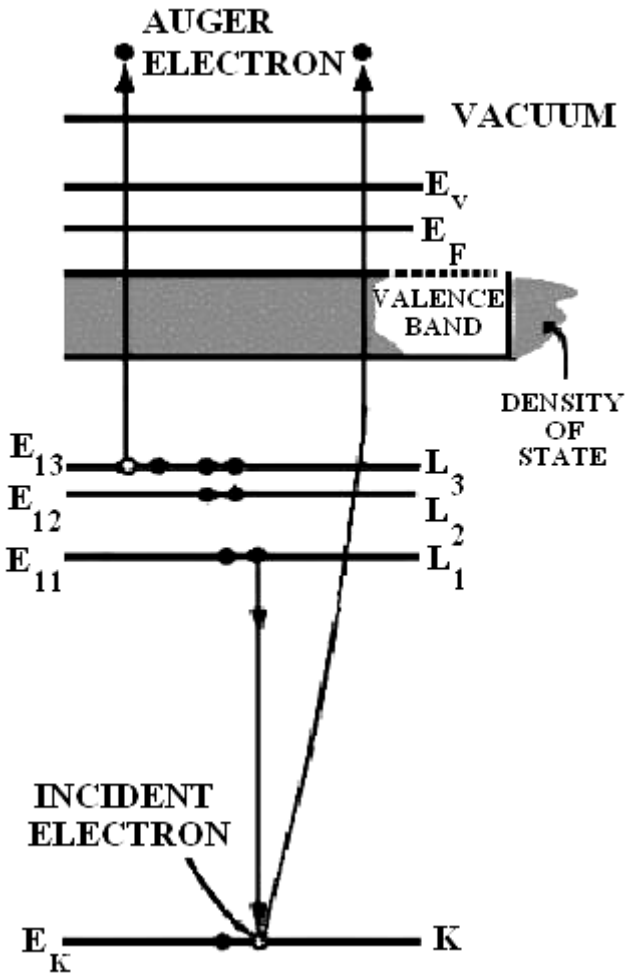

Fig. 3.9 Schematic energy level diagram illustrating the origin of the Auger effect. The Auger process in this figure is the KL_1L_3 process (Wild, 1981).

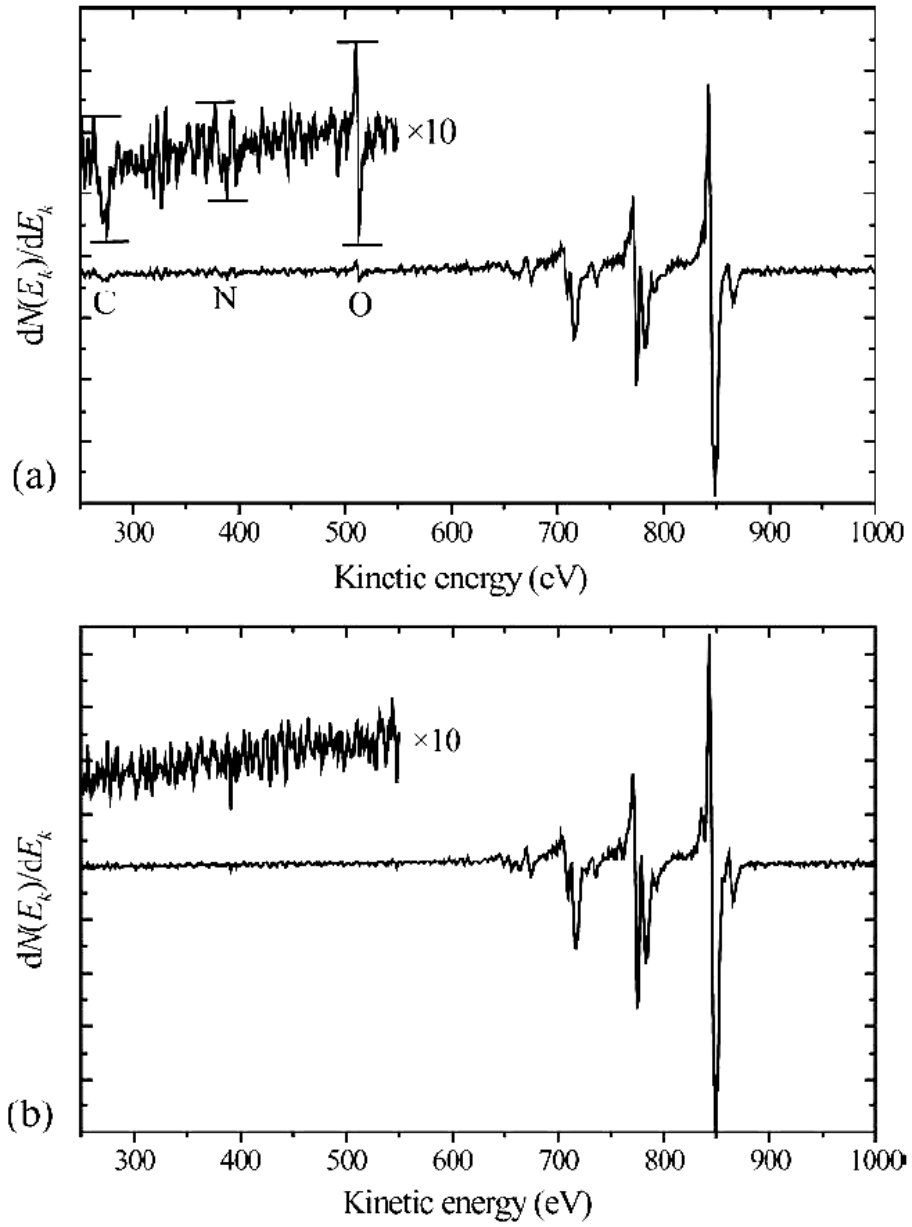

Fig. 3.10 Auger spectrum from *LVV* Ni in differential spectrum. (a) The upper graph represents the graph with contamination. (b) The lower graph is the graph from the clean Ni(111) structure.

3.1.6 Electron Gun

Electron guns are used as an electron source for the AES. The electron gun is LEG63 form Thermo VG Scientific (U.K.). The LEG63 is 5 keV electron source designed for pulse-counting AES. The gun consists of a filament, grid, lenses, apertures, and scanning quadrupoles. The spot size is less than 50 μm at 10 nA. The recommended working distance is 60 mm. For AES measurements, the sample is located just in front of the CLAM2 analyzer. A cone of Auger electrons emitted from the sample with appropriate kinetic energy pass through the entrance and exit slits of the analyzer when the potential difference is applied to the hemispheres. A channeltron located after the exit slit is used to detect the electrons. Electron-energy distributions can be obtained by slowly sweeping the analyzer deflection voltage of the hemispheres. A simple sketch of electron gun is shown in Fig. 3.12

3.1.7 Energy Analyzer

To analyze photoelectron, it is agreed among scientists in the filed of electron spectroscopy that a concentric hemispherical analyzer (CHA) is the most suitable type for photoemission studies. This type of analyzer provides important features such as high-energy resolution, high transmission and compatibility to UHV. In addition, an electron static lens can be integrated into the analyzer allowing longer working distances and controllable size of the analyzed area. The analysis chamber is provided with two CHA electron energy analyzers manufactured by Thermo VG Scientific (U.K.). The two analyzers are an ARUPS10 analyzer and a CLAM2 analyzer.

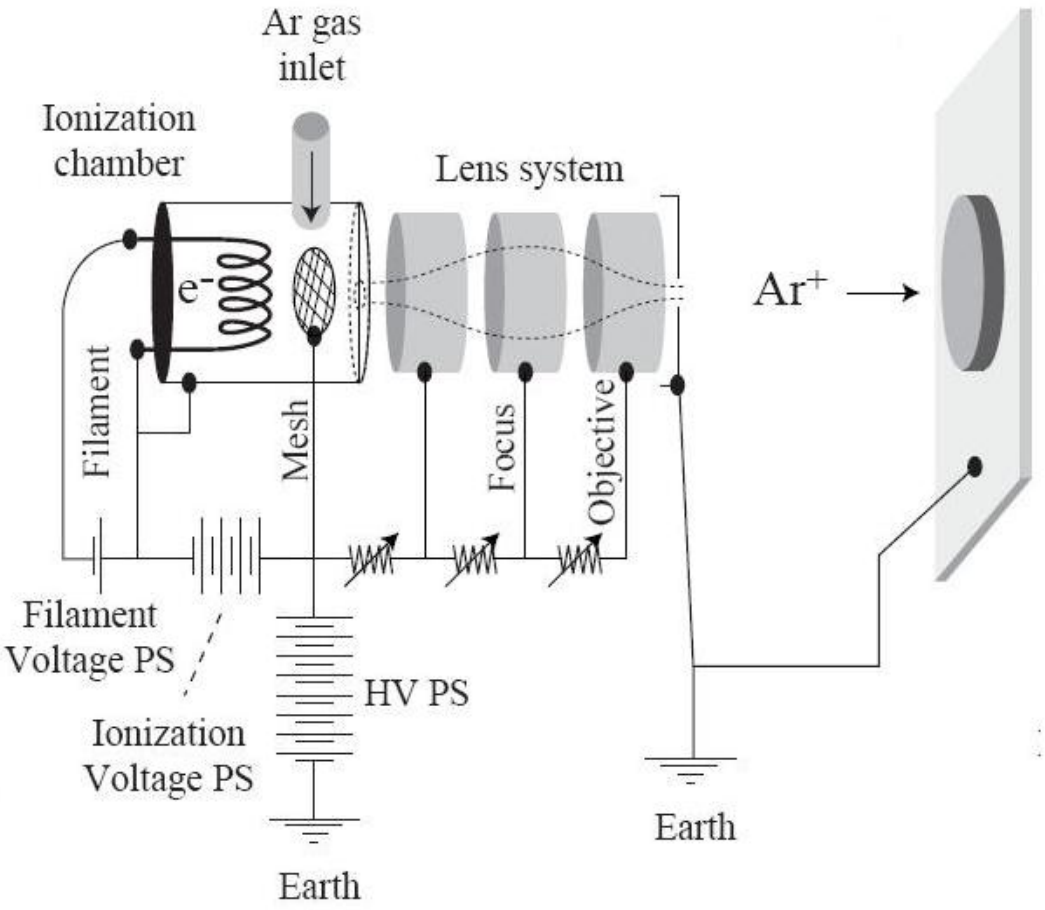

Fig. 3.11 Simple sketch of ion gun.

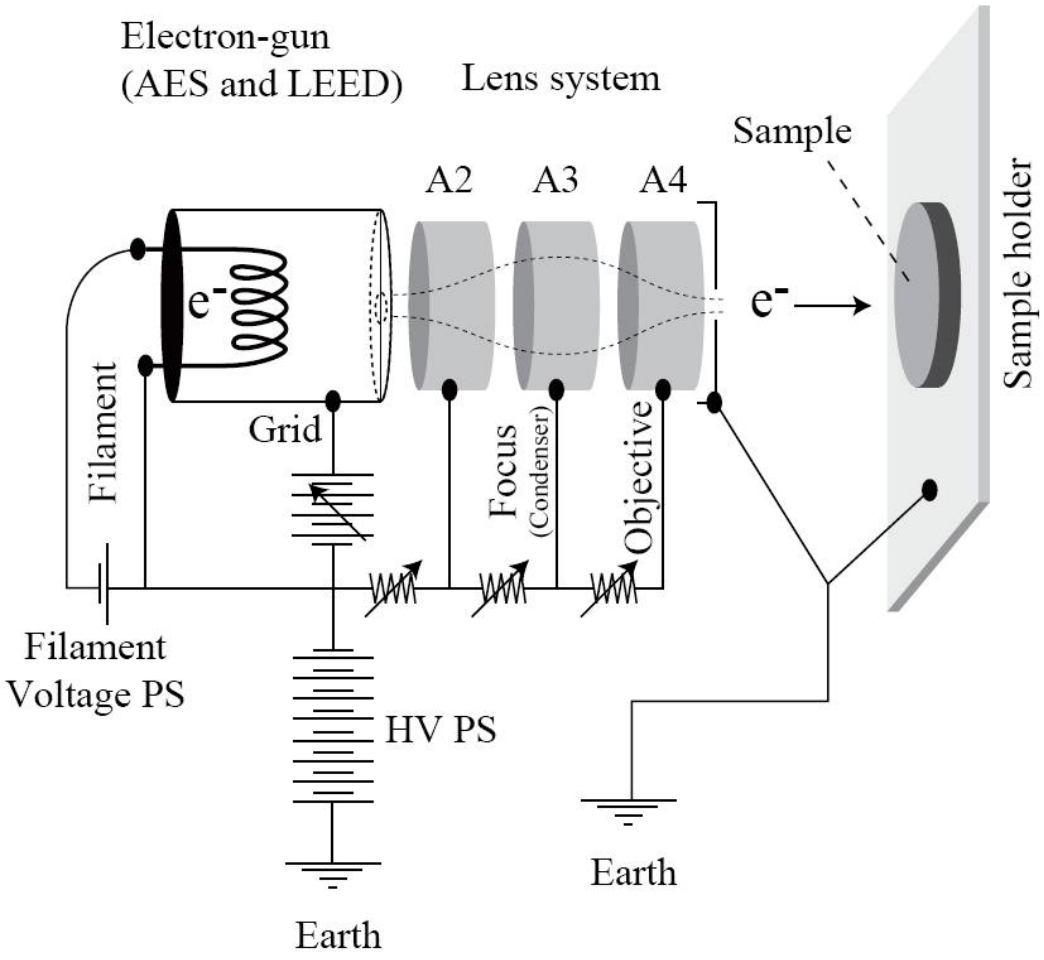

Fig. 3.12 Simple sketch of electron-gun.

3.1.7.1 ARPES Analyzer

ARUPS10 is a hemispherical analyzer with a mean radius of 75 mm. The analyzer is installed on a goniometer allowing the rotation of the analyzer around the sample position. Thus, the ARUPS10 analyzer is used for angle-resolved photoemission measurements. The specifications of the ARUPS10 analyzer are summarized in Table 3.2.

Table 3.2 Specifications of the ARUPS10 analyzer.

Analyzer	75 mm mean radius, hemispherical 180° with 30 mm hemisphere gap
Lens	Multi-element, electronically switchable acceptance angle from ±0.4° to ±2.00° (±0.2° with point source and lens switched off)
Detector	Multi-channel plate electron multiplier (MCP)
Goniometer	2-axis: 360° polar rotation, >90° azimuthal rotation, 0.1° vernier readouts
Energy Resolution	Variable from<10 meV to> 2eV
Chamber	5 mm thick μ -metal vacuum envelope

3.1.7.2 CLAM

CLAM2 analyzer is a concentric hemispherical energy analyzer with a mean radius of 100 mm. It is used for angle-integral photoemission measurements. The controller of the analyzer provides different mode of measurements. Thus, the CLAM2 analyzer is not only used for photoemission measurement but also AES measurements. The specifications of the CLAM2 analyzer are summarized in Table 3.3.

Table 3.3 Specifications of the CLAM2 analyzer.

Analyzer	hemispherical 150° with 100 mm mean radius
Lens	2 element transfer lens can be used in two distinct modes
Detector	Single channel electron multiplier
Slit size	0 to 4.0
Energy Resolution	CRR values: 1, 2, 4, 10, 40 and 100 CAE values: continuous 0-400 eV (manual) or 2, 5, 10, 20, 50, 100 and 200 eV (computer controlled)
Working distant	Flange to sample distance, 240 mm
Housing	μ-metal

Fig. 3.13 shows a schematic diagram of CLAM2. An electrostatic lens, which consist with two elements, is used to define the optics of electron emitted from the sample and be transported to the entrance slit of the analyzer. Before electrons entering the entrance slit, they experience a retarding or accelerating voltage to allow electrons with desired kinetic energy to pass through the analyzer and detected by the detector, which is located behind the exit slit. The resolution is defined by the pass energy. The electron-energy distributions are obtained by measuring the electron detected by the detector.

3.1.8 Light Source: Synchrotron Radiation Source

Synchrotron light is an electromagnetic wave emitted from relativistic charged particles moving with a curve motion. A synchrotron light consists of two main parts, *i.e.*, the injection system and storage ring. The synchrotron light source used in this thesis work is the Siam Photon Source (SPS) at the National Synchrotron Research Center (NSRC) of Thailand as shown in Fig. 3.14. The injection system produces a beam of electrons with energy up to 1.2 GeV and then injects into the storage ring. The machine parameters of the storage ring are shown in Table 3.3. The storage ring comprises of a series of magnet lattices which are designed to keep electrons circulating in the vacuum chambers of the storage ring. In the bending magnet, synchrotron light is emitted when electrons are experienced with the Lorentz force due to the presence of a dipole magnetic field perpendicular to the electron orbit.

Utilization of synchrotron in photoemission measurements expands the scope of many research fields. This is because of the special properties of synchrotron light.

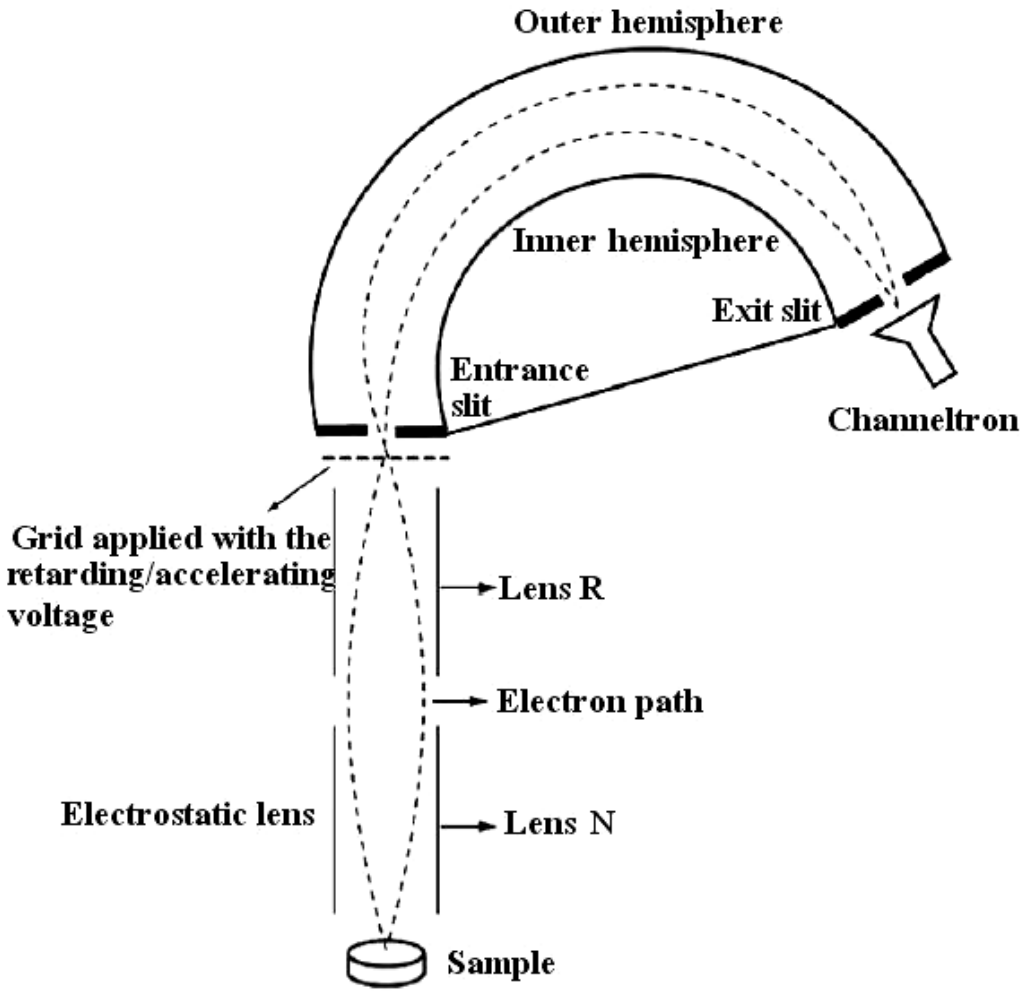

Fig. 3.13 Schematic diagram of CLAM2 with an electrostatic lens.

In the following, distinctive aspects of synchrotron radiation are described:

1) It is very intense light.
2) It has continuous spectrum extending over a wide spectral range. Synchrotron radiation from an undulator, however, has a spectrum comprising narrow bands with peaks at specific energies.
3) It is polarized light with its electric vector in the plane where the electron beam exists. In a specially designed undulator, circularly polarized light is generated. Synchrotron radiation emitted off the electron orbit plane is elliptically polarized.
4) It has a time structure of repeating short pulses.
5) It has low divergence. Synchrotron radiation emerging out of a small hole is confined in a narrow cone.
6) The spectrum of synchrotron radiation is accurately described by a theoretical formula.

Usefulness of property 1 is obvious. In the present work, property 2 is used for varying the excitation energy. This makes the bulk energy band mapping possible. Property 3 is used to observe the light polarization dependence of the excitation cross section. The incidence angle dependence of the excitation cross section is definitely determined by the use of this property. The parity dependence of the excitation cross section is also observed using this property. Property 5 is quite useful to produce a narrow beam of excitation light. This makes the energy band mapping be carried out with high spacial resolution. Properties 4 is not used in the present work. A quantitative description of synchrotron radiation with mathematical expressions is out of scope of the present work.

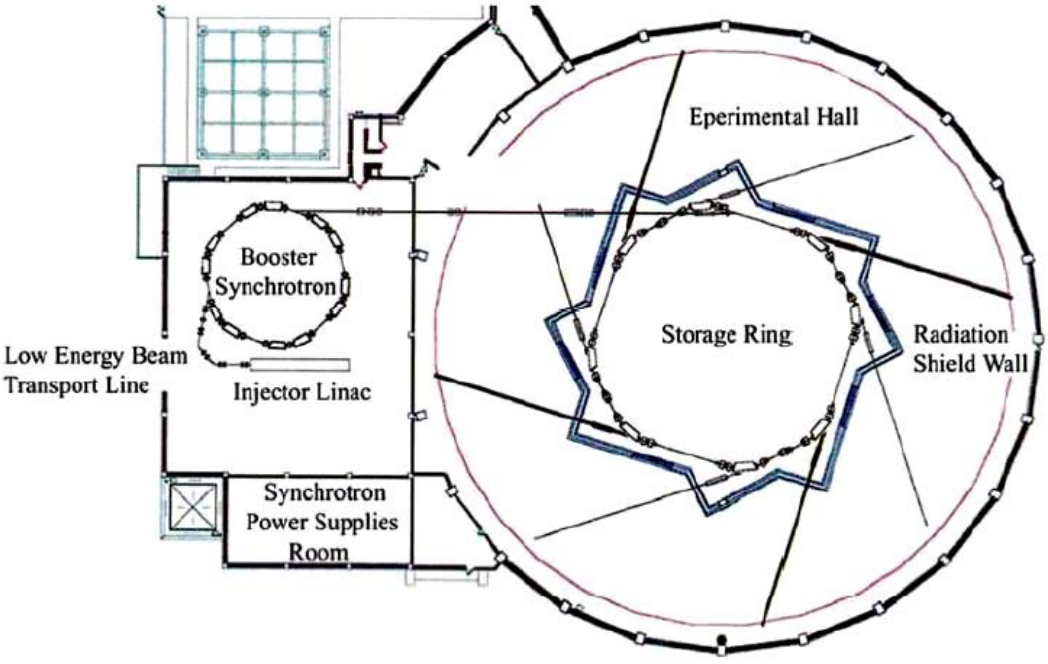

Fig. 3.14 The magnet arrangement of the storage ring of the Siam Photon Source.

Table 3.4 Some of the machine parameters of the storages ring of the SPS.

Parameters of storage ring	
Electron energy	1.0 GeV -1.2 GeV
Circumference	83.1 m
Stored beam current (nominal)	100.0 mA
Magnet lattice	Double Bend Achromat (DBA)
Super periodicity	4
Length of straight section	5.2 m × 4
Max RF voltage, V_{RF}	120 kV
RF frequency, f_{RF}	118 MHz
Harmonic number	32
Energy loss per turn	65.94 keV
Synchrotron oscillation frequency, f_s	13.5 kHz
Betatron tune, ν_x/ν_y	4.75/2.82

3.2 Optical Beamline

Photoemission measurements reported in this thesis were carried out at the BL-4 beamline at the Siam Photon Laboratory of NSRC. The beamline was developed for the investigation of electronic structures of solids using photoemission technique. The beamline employs a varied line-spacing plane grating (VLSPG) monochromator, which provides photons with energy between 20-240 eV (Prayoon Songsiriritthigul *et al.*, 2003; Prayoon Songsiriritthigul *et al*., 2004). The experimental station of the BL-4 beamline is a photoemission system which allows angle-resolved and angle-integral photoemission measurements to be carried out. The measurements can be performed using either synchrotron light or laboratory excitation sources.

The optical layout of the BL-4 beamline is illustrated in Fig. 3.15. The optical beamline consists of a pre-focusing toroidal mirror (M0), a VLSPG monochromator and a post focusing toroidal mirror (M2) (Prayoon Songsiriritthigul *et al.*, 2001). The beamline utilizes light from a BM4 bending magnet of the storage ring. Synchrotron light with acceptance angle of 5 mrad and 3 mrad for the horizontal and vertical directions respectively is used for the BL-4 beamline. The monochromator comprises of an entrance slit (S1), focusing mirror (M1), an aperture, three exchangeable VLSPG and an exit slit (S2). The three exchangeable gratings with the line density at the center of the grating of 300, 600 and 1200 lines/mm are used to provide photon energy ranges of 20-80, 40-120 eV and 80-240 eV respectively. The detailed specifications of the gratings are given in Table 3.5.

The advantage of this type of monochromator is that scanning of photon energy can simply be done by rotating the grating. For the whole photon energy range, the monochromatic light is focused virtually at the position of the exit slit, S2.

Thus, no movement of the exit slit along the optical axis is necessary when photon energy is changed. The post-focusing toroidal mirror M2 is used to re-focus the monochromatic light on the sample.

Table 3.5 Parameters of the gratings used in the BL-4 beamline.

Grating No.	N_0 (lines/mm)	Groove depth (nm)
VPG-1	300	43
VPG-2	600	22
VPG-3	1200	12

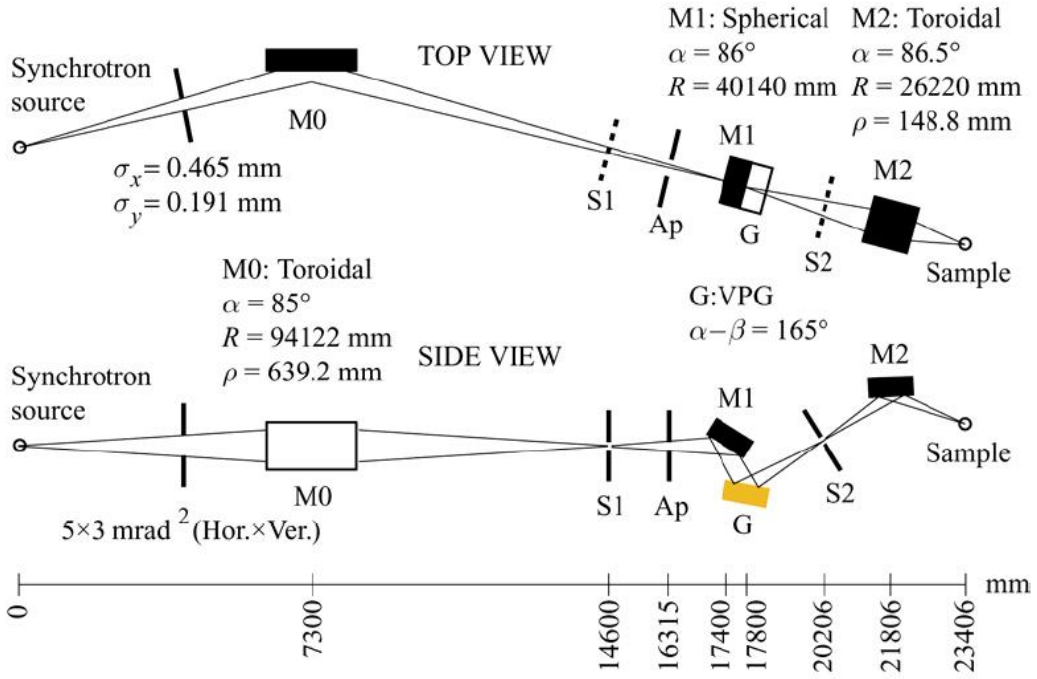

Fig. 3.15 The optical layout of the BL-4 beamline at the Siam Photon Laboratory.

3.3 Sample Preparation and Characterization

A sample used in this thesis work is a 10 mm disk of Ni(111) with 1 mm thick, which has been cut from a cylindrical rod of single crystal nickel with purity of 99.999%. The original rod was purchased from Goodfellow Cambridge Co. Ltd. The crystal had been grown in the way that the [111] direction was along the rod axis. The sample was cut out so that its surface the (111) plane that confirmed the crystal orientation by X-ray diffraction measurements using a diffractometer at the Center for Scientific and Technological Equipment at the Suranaree University of Technology. The cutting was done using a Struers ACCUTOM-5 cutting machine with a diamond cutting wheel. The surface was carefully polished so that the surface orientation was not changed from that of (111) by using a Strures ROTOPOL-25 polishing machine with a Strures ROTOFORCE-1 force control.

After the procedure of polishing the sample surface had been completed, the sample was cleaned by ultrasonic cleaning. In addition to the physical removing of the layer of adsorbed molecules by ultrasonic vibration, some liquid solvents, acetone and ethyl-alcohol, were used to remove organic compounds sticking to the surface. Finally distilled water was used and fixed to a molybdenum sample holder.

Fig. 3.16 shows derivative Auger spectra of our samples to estimate the amount of oxygen on the surface. Concentration of oxygen atoms can be estimated from peak intensities using equation below.

$$C_O = \frac{I_o / S_o}{(I_o / S_o) + (I_{Ni} / S_{Ni})} \times 100\% \qquad (3.2)$$

Here, I_o represents peak height of oxygen *KLL*, S_o relative sensitivity of oxygen *KLL* at 510 eV of kinetic energy, I_{Ni} peak height at 850 eV of kinetic energy in Fig. 3.16, S_{Ni} relative sensitivity of nickel *LMM* at 850 eV of kinetic, S_o of 1.1012 and S_{Ni} of 1.0478 were used in AES using 5 keV electron beam (Davis, MacDonald, Palmberg, Riach and Weber, 1996). In Equation (3.2), mean free pass is not taken into account because of the cascade process of incident electrons and Auger electrons. However, this cascade process makes Auger spectroscopy surface-sensitive in comparison with that in X-ray photoelectron spectroscopy.

On the basis of the concentration in Equation (3.2), we calculate a concentration corresponding to a monolayer of oxygen on nickel surface. We assume following points. First, there is no other impurity on surface. Second, the total number of Auger electrons from oxygen on the top of surface can be observed. Third, the number of Auger electrons can be estimated by a factor of exponential function as a function of the depth of layer from the surface.

$$\left.\begin{aligned} \text{C}_\text{o}\text{ per monoayer}/100 &= \frac{\exp\left(-\frac{n_\text{o}\cdot d_\text{o}}{\lambda_\text{o}}\right)}{\sum_{n=1}^{\infty}\exp\left(-\frac{n_\text{Ni}\cdot d_\text{o}}{\lambda_\text{Ni}}\right)} \\ &= \frac{1-\exp\left(-\frac{n_\text{Ni}\cdot d}{\lambda_\text{Ni}}\right)}{\exp\left(-\frac{n_\text{Ni}\cdot d}{\lambda_\text{Ni}}\right)} \\ &= 0.15 \end{aligned}\right\} \qquad (3.3)$$

Here, n_o is defined as zero, which is the index of layer from the top layer of oxygen layer on the surface, d_o the interlayer distance between oxygen layers, λ_o the mean free path of oxygen, n_Ni the depth of nickel layer from the surface, d_Ni the

interlayer distance between nickel layer, λ_{Ni} the mean free path of nickel. d_{Ni} is 2.03 Å. λ_{Ni} is 14.4 Å (Tanuma, Powell and Penn, 1990). According to this calculation, one monolayer corresponds to 15% of the concentration.

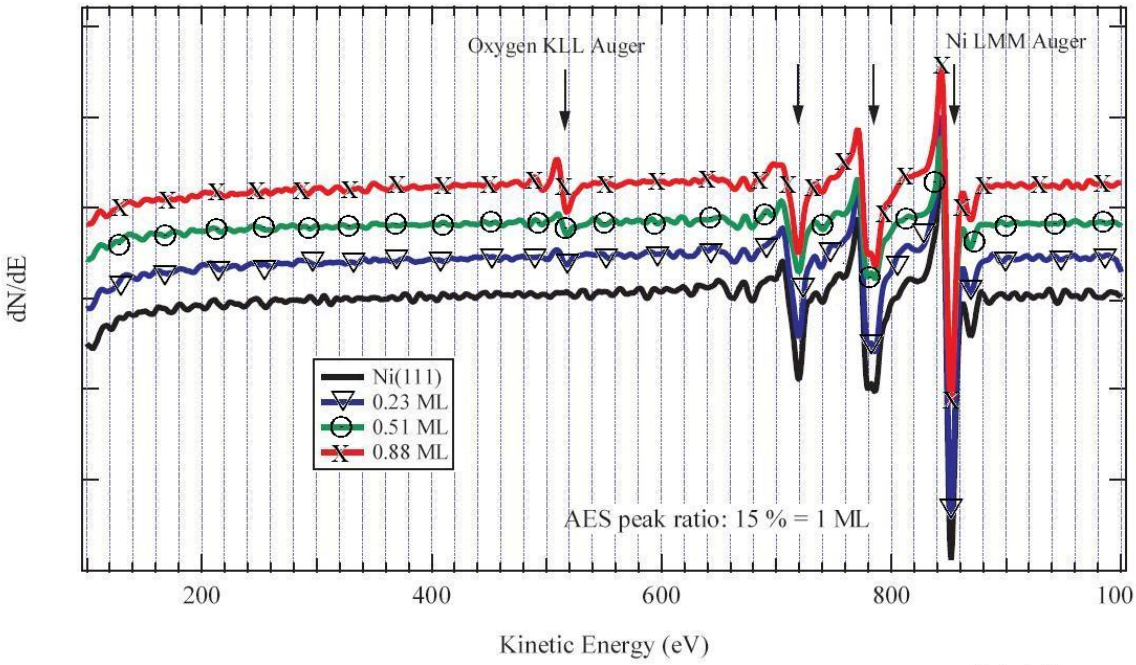

Fig. 3.16 Auger spectra of clean surface p(1×1), 0.23 ML - p(2×2), 0.51 ML - c(2×2) and 0.88 ML - p(1×1) oxygen-adsorbed surfaces.

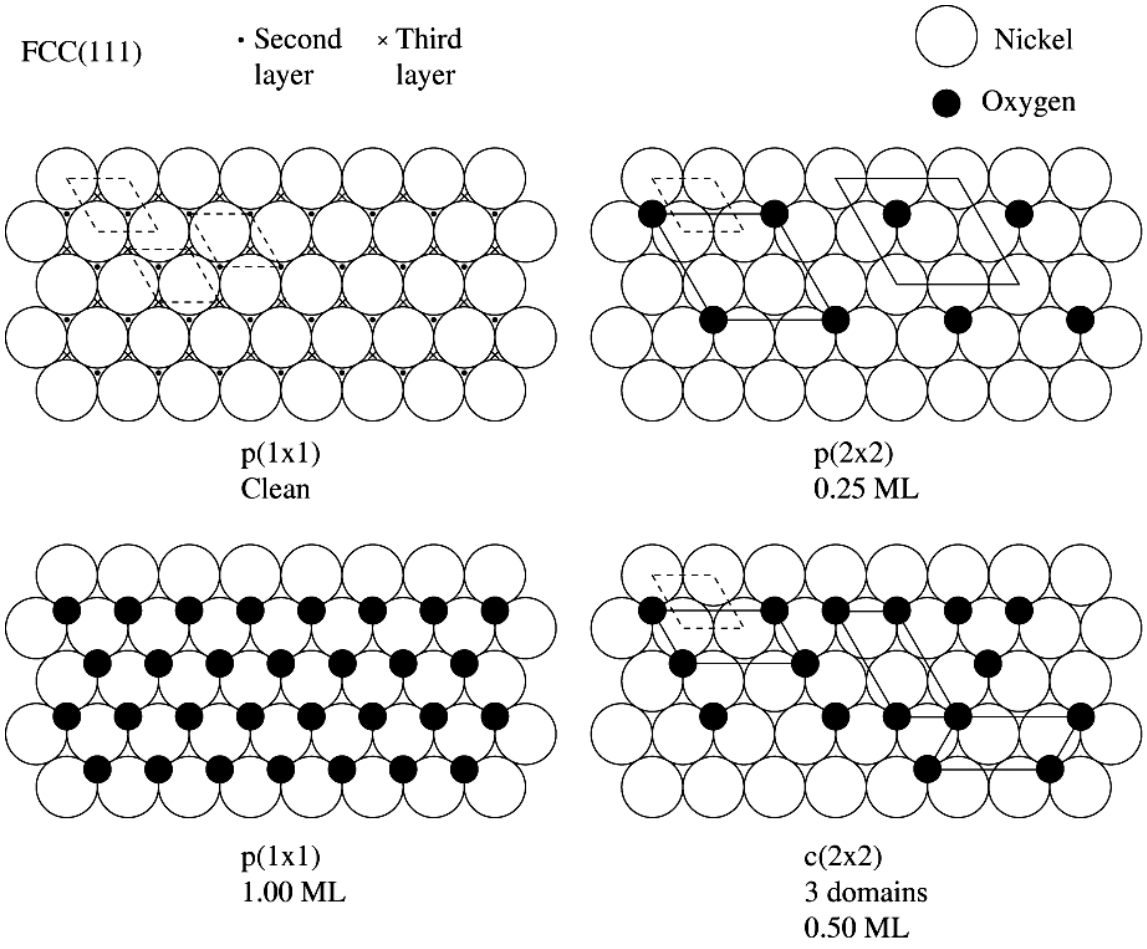

Fig. 3.17 Surface atomic models for clean, p(2×2), c(2×2)-3 domains and p(1×1) oxygen adsorbed Ni(111) surfaces (Top view).

CHAPTER IV

RESULTS AND DISCUSSION

The main purpose of this work is to obtain the energy band structure of clean and oxygen-adsorbed Ni(111) surfaces. The obtained information is fundamental for understanding the electronic properties relevant surfaces. Some theoretical and experimental data have been reported on the energy band structure of surfaces. Thus, it is important to compare the data obtained in this work with those reported so far.

4.1 Experimental conditions

Photoemission experiments were carried out at BL4 of the Siam Photon Laboratory of National Synchrotron Research Center (Nakajima *et al*., 2007). The ARPES apparatus consists of an ion gun, an electron gun, a temperature-controlled sample holder and an electron-energy analyzer (ARUPS10). Pressure in the analysis chamber was below 2×10^{-10} mbar during photoemission measurements. The overall energy resolution of measured spectra resulting 170 meV at 45 eV of photon energy was confirmed on the Fermi edge of a gold sample at room temperature.

The sample treatment was carried out under the following conditions. After degassing of the sample holder, a single-crystal Ni(111) sample (99.999% purity) was bombarded by argon ion with kinetic energy of 1.0 keV with 2.0×10^{-6} mbar to remove sulphur impurity which was monitored by Auger electron spectroscopy (AES). Next, repeated cycles of argon-ion bombardment and subsequent annealing at 720 K

reduced the amounts of carbon and oxygen impurities to be negligible. Finally, the long-range order of periodic surface structure was checked by low-electron-energy diffraction (LEED). The sample surface was identified as a clean surface with a very sharp and low-background p(1×1) LEED pattern. An oxygen-adsorbed Ni(111) surface was prepared by introducing oxygen gas into the chamber where a sample was heated at 450 K. During the flow of oxygen gas, the pressure was kept constant at 1.0×10^{-7} mbar. After the surface was exposed to oxygen gas, the surface was checked by LEED patterns and AES measurements prior to photoemission measurement. Upon oxygen adsorption, c(2×2) and p(1×1) structures appear in 0.51 ML and 0.88 ML O/Ni(111) surfaces, respectively. On the basis of stoichiometry analysis, p(2×2) and p(1×1) lattice structures correspond to 0.25 ML and 1.0 ML in non-reconstructed fcc-(111) surface structures.

Since a real surface has lattice-domain structures caused by steps, defects and so on, the observed LEED patterns correspond to surface structures averaged on the area irradiated with the electron beam. Therefore, the surface of c(2×2)-0.51 ML LEED pattern qualitatively corresponds to a multi-domain c(2×2)-0.50 ML O/Ni(111) surface illustrated in Fig. 4.1. On the other hand, the surface of p(1×1)-0.88 ML LEED pattern corresponds to p(1×1)-1.00 ML O/Ni(111) surface modified by a lack of oxygen adsorbate in the perfect monolayer surface. These correspondences between surface structures and LEED patterns are summarized in Fig. 4.1.

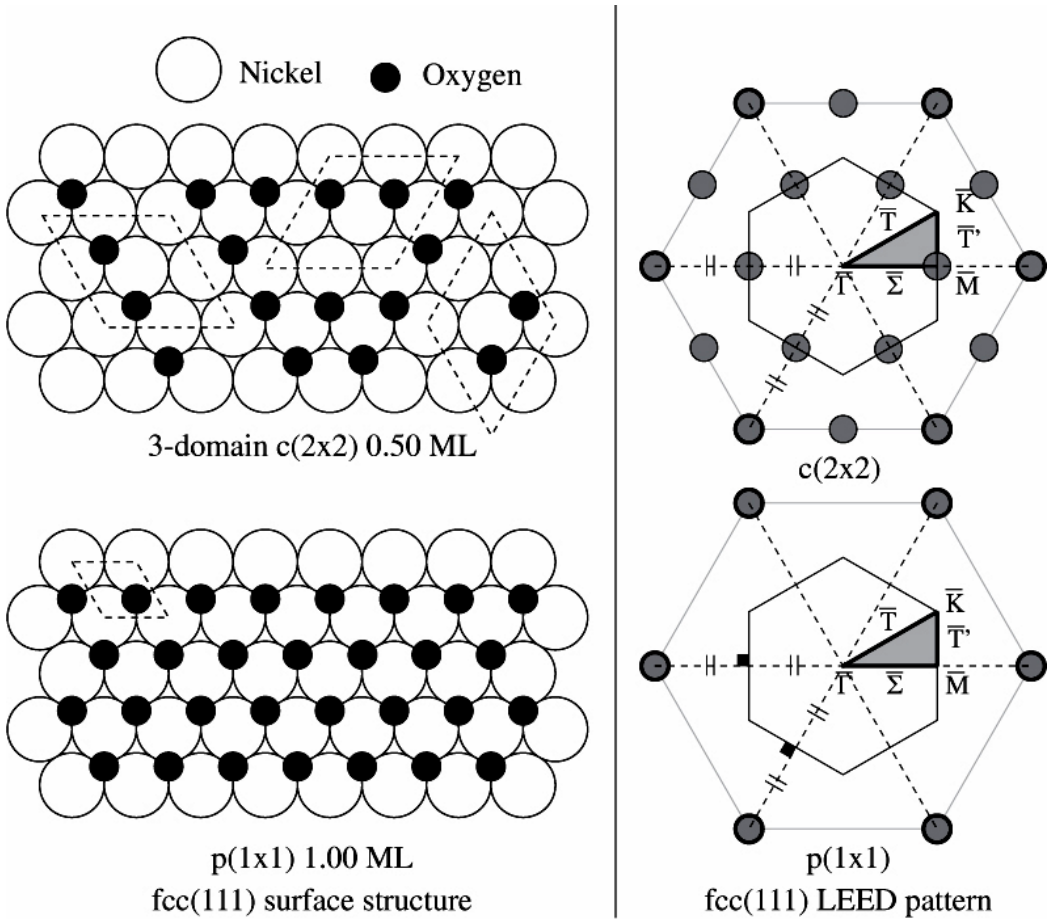

Fig. 4.1 Schematic illustration of atomic and reciprocal structures on O/Ni(111) surfaces. Left figure shows atomic structure of c(2×2)-0.50 ML (top) and p(1×1)-1.00 ML (bottom) oxygen-adsorbed Ni(111) surfaces. Right figure represents LEED patterns on c(2×2) (top) and p(1×1) (bottom) oxygen-adsorbed Ni(111) surfaces. First Brillouin zones are also illustrated with corresponding irreducible representations in the inset of the illustration of LEED patterns.

4.2 Electronic structure on oxygen adsorbed surface

In this section, I present how the oxygen adsorption on Ni(111) surface gives an effect on the spectral intensity that is directly related to the atomic and electronic structures in the surface and interface. Fig. 4.2 shows ARPES spectra of the p(1×1)-clean, c(2×2)-0.51 ML oxygen-adsorbed and p(1×1)-0.88 ML oxygen-adsorbed Ni(111) surfaces. The excitation light incidents on the sample at 60° and the energy distribution of photoelectrons was measueed in normal-emission mode. The photon energy of 45 eV corresponds to the Γ point of bulk Brillouin zone (BZ). To investigate the effects of oxidation to the spectral profiles, each spectrum was normalized to the integrated intensity. In this normalization process, we assumed the same photoionization cross section for Ni 3*d* and O 2*p* states at the photon energy of 45 eV (Yeh and Lindau, www, 1985).

This idea is supported by theoretical atomic subshell photoionization cross section based on the Hartree-Fock-Slater one-electron central potential model as shown in Figs. 2.18 and 2.19 corresponding to Ni and O, respectively. The cross section of Ni3*d* is almost equivalent to that of O2*p* of 9.0 Mbarns at 45 eV of photon energy. Hence in Fig. 4.2, the hybridization between Ni 3*d* and O 2*p* states brought about by the oxygen adsorption are appeared as the same amount of the decrease and increase of the spectral intensity in Ni 3*d* and O 2*p* originated spectral profiles, respectively. In Fig. 4.2, the binding energies of spectral features are indicated by the ticks with letters from **a** to **f**.

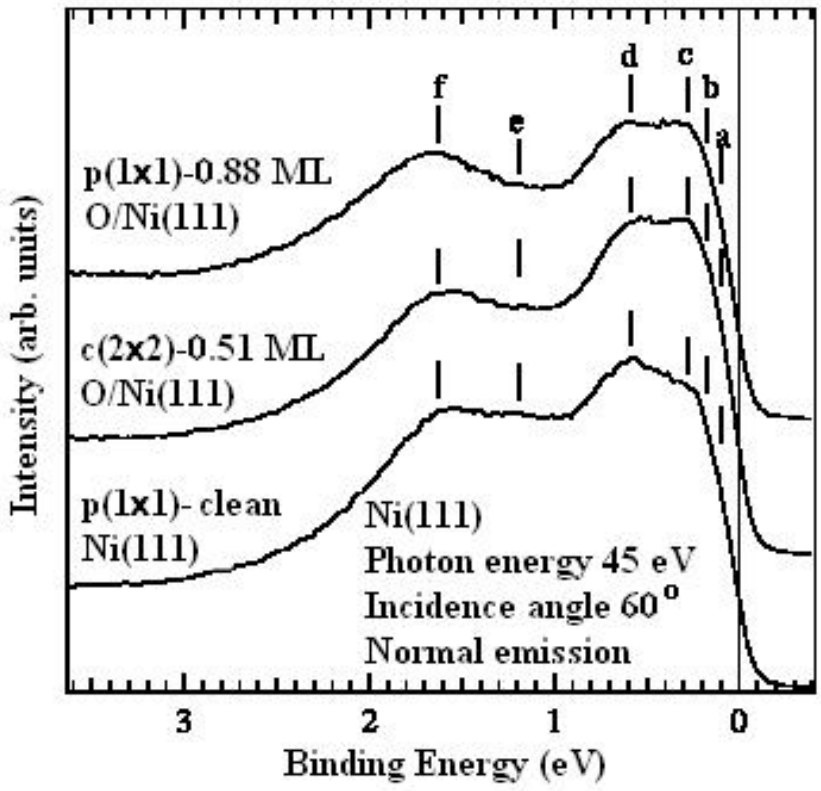

Fig. 4.2 Normal-emission spectra of p(1×1)-clean, c(2×2)-0.51 ML oxygen-adsorbed and p(1×1)-0.88 ML oxygen-adsorbed Ni(111) surfaces. Photon energy of 45 eV is incident on the sample at 60° and photoelectrons are measured in normal emission mode.

Since the oxygen adsorption would break the symmetry of the atomic structure at the surface, the surface states which are observed in the Ni(111) surface disappear on the oxygen-adsorbed surfaces. On the other hand, interface states would appear in the oxygen adsorbed surface by electron transfer from nickel atoms to adsorbed oxygen due to a large electron affinity of oxygen atom.

This results in the surface relaxation increasing the interlayer distance between surface and sub-surface layers. In Fig. 4.2, spectral features **a**, **b** and **c** near the Fermi level (E_F) are assigned to be interfacial states, which are enhanced by the oxygen adsorption in the Ni(111) surfaces.

The feature **d** does not decrease in the c(2×2)-0.51 ML O/Ni(111) surface, while it decreases on the p(1x1)-0.88 ML surface. Therefore, the peak **d** is to be originated from the electronic structures of sub-surface layer.

The feature **e** is originated from surface electronic states because its intensity decreases monotonically with oxygen adsorption.

The peak **f** is assigned to be electronic states in bulk Ni because the spectral intensity does not change much as the adsorption proceeds. The O 2*p* originated features are overlapped in the higher binding-energy side of the feature **f**. Small binding energy shift observed in each spectral feature in different surface conditions are caused by the relaxation of the surface atomic structure by oxygen adsorption.

4.3 Bulk energy bands

The energy-band dispersion along $k_\perp$ direction provides important information not only the bulk but also the surface and interfacial electronic structures that have no $k_\perp$ dispersion. Fig. 4.3 shows ARPES spectra dependent on photon energy on the clean Ni(111) surface. ARPES spectra in Fig. 4.5 were measured in normal-emission mode corresponding to the bulk-energy band along the Γ-Λ-L direction. The light is incident on the sample at 60°. Photon energy is varied over the range between 40 eV and 100 eV. Tick markers represent spectral features and dashed lines the peak locations shown in Fig. 4.2. The geometry of ARPES measurement is also shown in the inset. The inset figure defines incident angle and emission angle.

In Fig. 4.3, spectral features d and e have a constant dispersion in the $k_\perp$ direction. However, the $k_\perp$ dispersions of features **a**, **b** and **c** are not clearly identified because of the overlap of bulk-band structures. The bulk-band structures were calculated on the basis of free-electron final-state approximation. However, it is difficult to assign the spectral features to theoretical bulk-band structures, because the nickel bulk-band structure has served as a touchstone of energy-band calculation in terms of many-electron interaction (Weling and Callaway, 1982).

Our energy band obtained from ARPES spectra in Fig. 4.3 shows in poor agreement with reported first-principle bulk-band calculations (Nakajima *et al*., 2007). However, recently improved calculations including self-energy correction show in better agreement with our result than the others (Manghi, Bellini and Arcangeli, 1997). This result suggests the importance of self-energy correction in the analysis of ARPES spectra based on the energy-band theory.

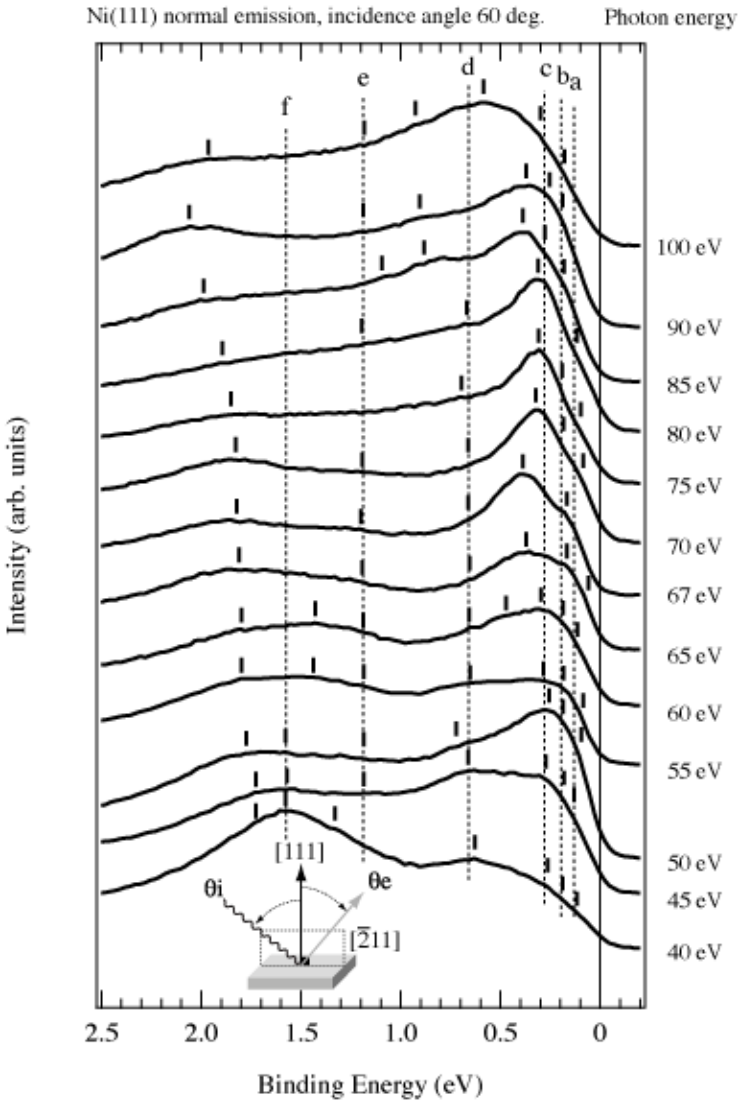

Fig. 4.3 ARPES spectra dependent on photon energy on p(1×1)-clean Ni(111) surface. The spectra were measured at 60° of incident angle. Photon energy is varied in between 40 eV and 100 eV in normal-emission mode that corresponds to the bulk band along the Γ-Λ-L direction. Tick markers represent spectral features and dashed lines the spectral features shown in Fig. 4.2.

4.4 Interfacial energy bands

Fig. 4.4 shows ARPES spectra of the p(1×1)-clean Ni(111), c(2×2)-0.51 ML O/Ni(111) and p(1×1)-0.88 ML O/Ni(111) surfaces, which were measured along Γ-Σ-M direction in the surface BZ. The geometry of ARPES measurements is shown in the inset of the figure. Emission angle of photoelectron is indicated on the right-hand side of each spectrum. The M zone edge at E_F corresponds to the emission angle around 27˚. Tick markers in the normal-emission spectra indicate the spectral features shown in Fig. 4.2. It should be remarked in the figure that at each point in the surface BZ, the spectral profile strongly depends on the amount of oxygen adsorption. This reveals that the energy dispersion of the electronic states at the interface and subsurface is different in the O/Ni(111) system. To elucidate the effects of oxygen adsorption to ARPES spectra, we obtained difference spectra by subtracting O/Ni(111) spectra from clean Ni(111) spectra. Fig. 4.5 shows the difference spectra of (a) c(2×2)-0.51 ML and (b) p(1×1)-0.88 ML O/Ni(111) surfaces from that of the clean Ni(111) surface. The positive area (black) corresponds to the decrease of spectral intensity due to the oxygen adsorption, while the negative area (gray) indicates the increase of spectral intensity. Tick markers in the normal-emission spectra correspond to the spectral features in Fig. 4.2.

In both oxygen-adsorbed surfaces, the spectral features **a**, **b** and **c** near E_F appear as negative areas in the difference spectra and show energy dispersion along Γ-Σ-M direction in the surface BZ. Since their intensities are suppressed by increasing of the oxygen coverage we assigned these features as the majority-spin interfacial states due to hybridization between Ni 3*d* and O 2*p* states. To confirm this assignment we carried out the first-principle energy-band calculation using the Vienna *ab-initio*

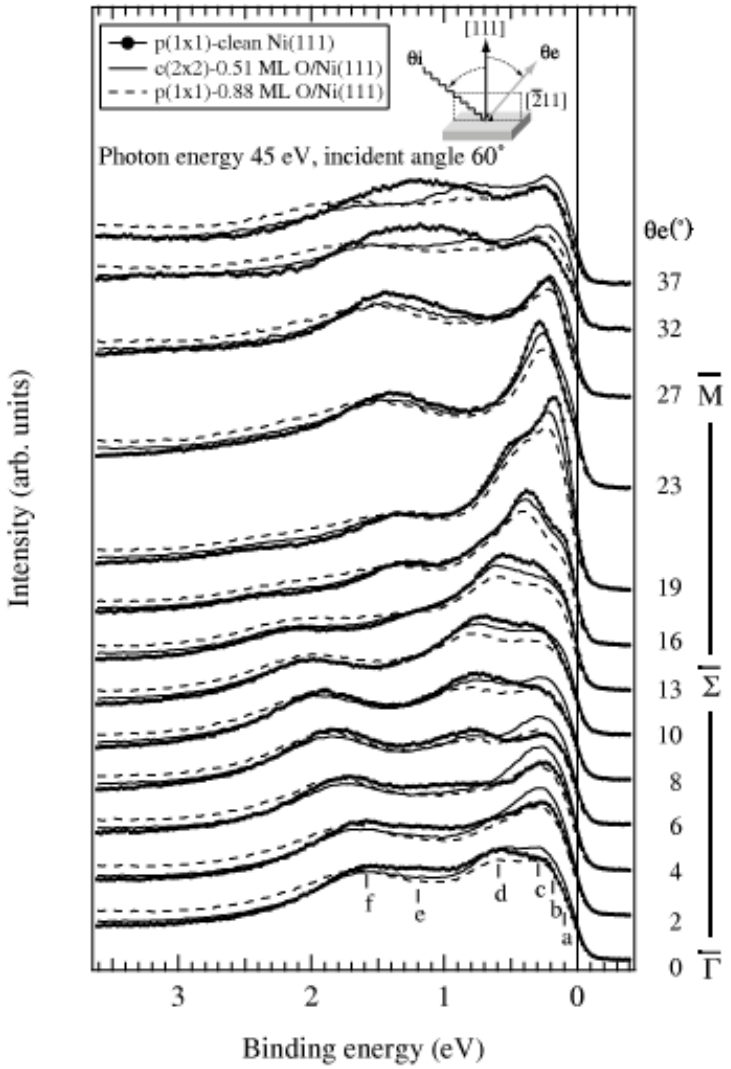

Fig. 4.4 ARPES spectra of the clean Ni(111), c(2×2)-0.51 ML O/Ni(111) and p(1×1)-0.88 ML O/Ni(111) surfaces along the Γ-Σ-M direction. The geometry of ARPES measurement is also shown in the inset with incident angle of θ_i and emission angle of θ_e. Emission angles are indicated on the right-hand side of each spectrum. Tick markers in the normal-emission spectra correspond the spectral features in Fig. 4.2.

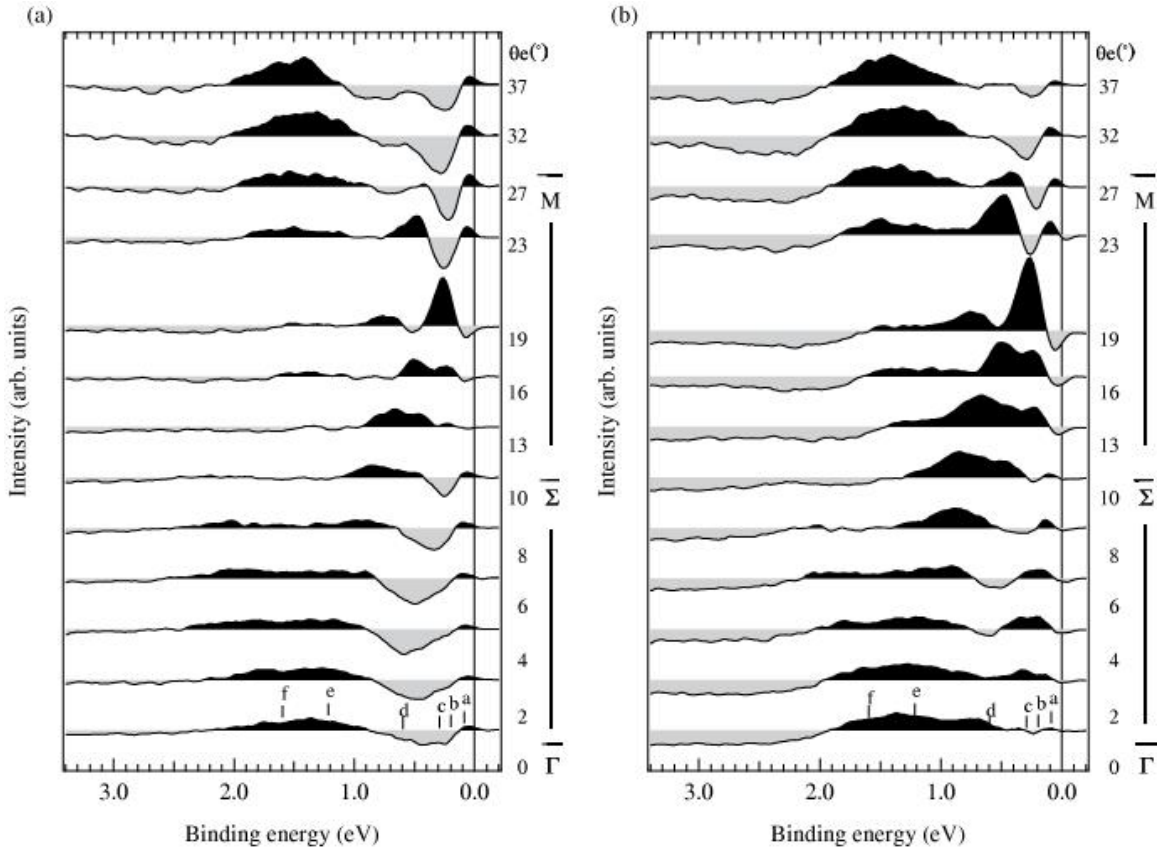

Fig. 4.5 Subtracted ARPES spectra of the (a) c(2×2)-0.51 ML and (b) p(1×1)-0.88 ML O/Ni(111) surfaces from that of the clean Ni(111) surface shown in Fig. 4.3. A positive area is filled with black, while negative area is filled with gray. Tick markers in the normal-emission spectra correspond to the spectral features in Fig. 4.2.

simulation package (Kresse and Hafner, 1993). The molecular-orbital calculation was also carried out by DV-Xα SCAT package to obtain information of the characteristics of the bonding states between Ni 3*d* and O 2*p* orbitals at the interface (Adachi, Tsukada and Satoko, 1978). In both calculations, the oxygen-induced density of states (DOS) was found at the binding energy around 0.5 eV where DOS of clean Ni(111) surface varies smoothly. Fig. 4.6 shows the results of the first-principle energy-band dispersions on the p(1×1)-clean Ni(111) and p(2×2)-0.25 ML O/Ni(111) surfaces calculated for five-nickel layers using ultra-soft pseudo-potentials. Since the minority-spin states have no significant effect on the oxygen adsorption in the occupied states, only majority-spin states are shown in the figure. In Fig. 4.6, the majority-spin bands are distributed at the binding-energy region above 0.5 eV in both surfaces. It should be remarked in O/Ni(111) surface that new state appear in the binding-energy region between 0.3 eV and 0.6 eV, which are indicated by thick lines.

Although the energy dispersion of the new states does not agree well with that of the observed interfacial states near E_F, the binding energies of these new features are in good agreement with oxygen-induced interfacial states observed in the difference spectra in Fig. 4.5. Fig. 4.7 and Fig. 4.8 show the DOS of Ni_9 and O_4/Ni_9 clusters calculated by molecular-orbital method, respectively. The Ni_9 cluster represents a part of clean Ni(111) surface. The O_4/Ni_9 cluster with high symmetry (D_{2h}) is considered to be 0.51 ML O/Ni(111) surface. Bottom of Fig. 4.8 also shows the overlap population between Ni and O atoms corresponding to the contribution of covalent charge to bonding formation. A positive overlap population corresponds to the bonding character, while a negative overlap population the anti-bonding character. A comparison between these molecular-orbital calculations revealed that in the O/Ni

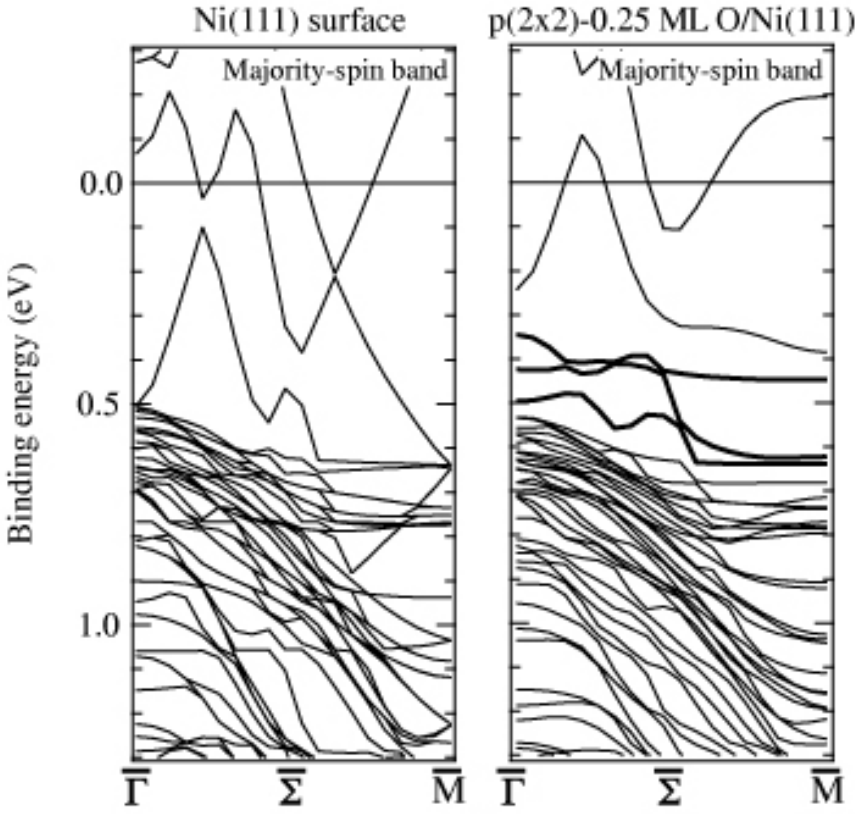

Fig. 4.6 First-principle energy-band dispersions calculation using the Vienna *ab-initio* simulation package (Kresse and Hafner, 1993). On the p(1×1)-clean Ni(111) and p(2×2)-0.25 ML O/Ni(111) surfaces. Left figure represents the energy band on the p(1×1)-clean Ni(111) surface and right figure the energy band on the p(2×2)-0.25 ML O/Ni(111) surface. Only majority-spin bands are shown in the figure.

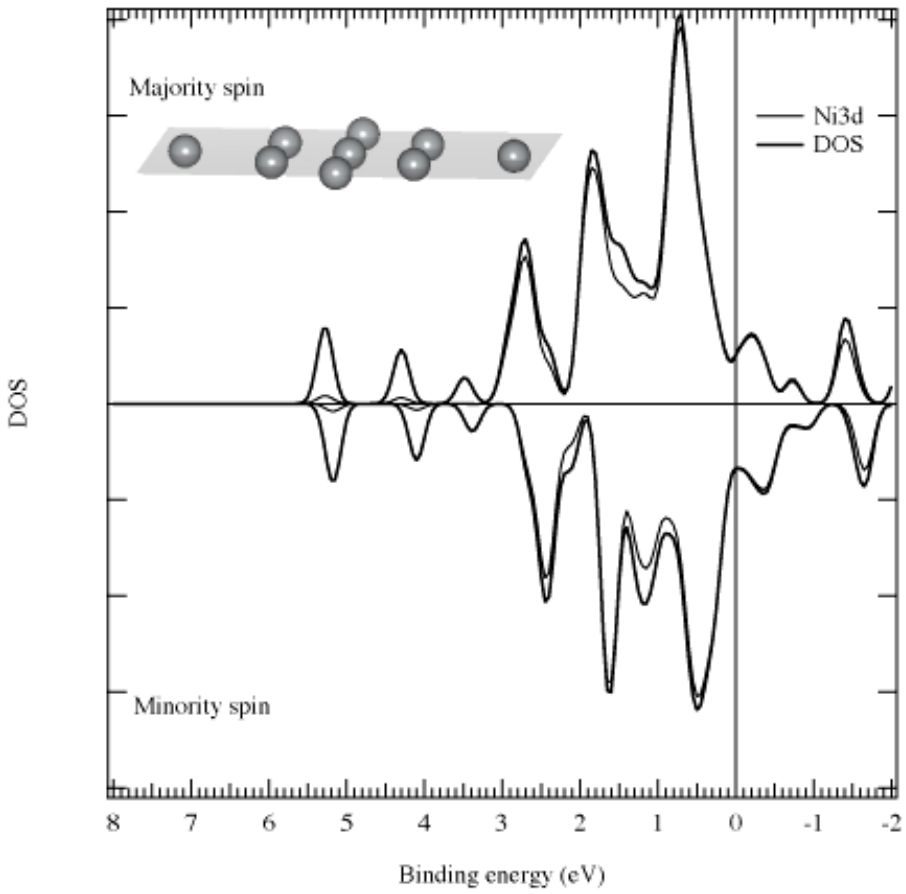

Fig. 4.7 DOS calculation using the DV-Xα method (Adachi, Tsukada and Satoko, 1978). On the Ni cluster. Ni 3*d* partial DOS is also shown. Majority spin and minority spin bands are plotted in positive and negative ordinates, respectively. Cluster models are illustrated in the inset of each figure.

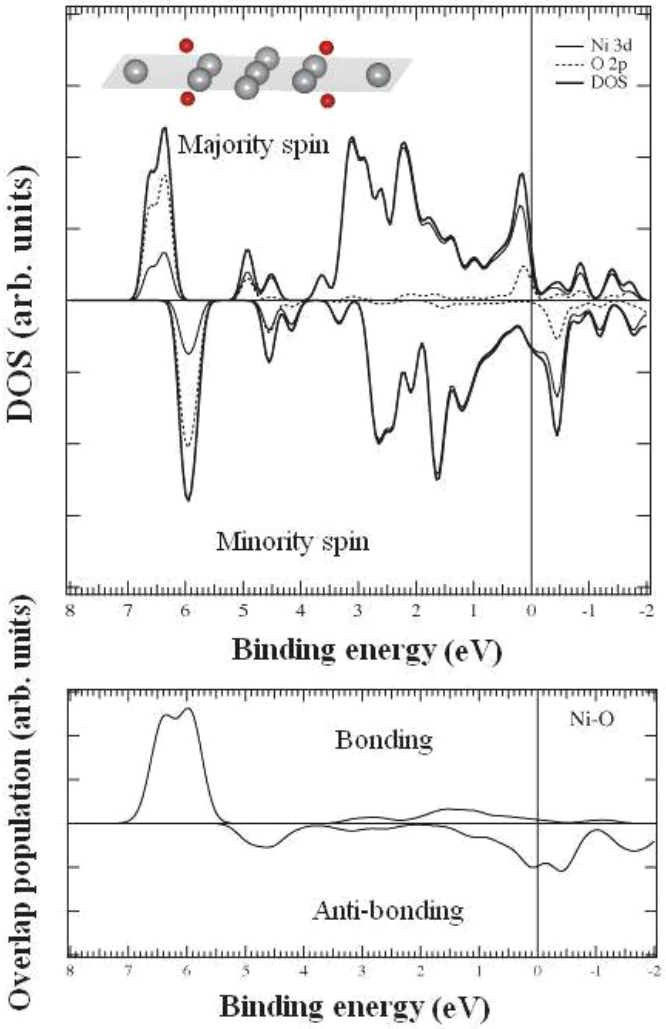

Fig. 4.8 DOS calculation using the DV-Xα method (Adachi, Tsukada and Satoko, 1978). On the O_4/Ni_9 cluster. Ni 3*d* and O 2*p* partial DOS are also shown. Majority spin and minority spin bands are plotted in positive and negative ordinates, respectively. Cluster models are illustrated in the inset of each figure. Large spheres represent Ni atom and small spheres O atom. Bottom figure shows a corresponding overlap population between Ni and O atoms. Positive and negative overlap populations indicate bonding and anti-bonding characters, respectively.

cluster, the new majority-spin DOS appears around the binding energy of 0.2 eV and they are originated from the majority-spin anti-bonding states between Ni 3*d* and O 2*p* states. The cluster model causes the small difference of binding energy.

According to the reported molecular-orbital and relativistic energy-band calculations by Hong *et al*. (2004), the interfacial states correspond to the anti-bonding π states of majority spin and the filling of this anti-bonding states causes a strong surface relaxation and buckling in the subsurface layer to enhance the perpendicular magnetic anisotropy. The reorientation of the magnetization direction due to the oxygen adsorption has been explained by quenching the surface anisotropy. In O/Ni/Cu(001) surface, Hong *et al*. and Amemiya *et al*. (2005), the adsorbates effectively suppress the out-of-plane surface-electron orbitals, which results in the decrease of surface in-plane magnetic anisotropy brought about by spin-orbit interaction. To obtain information of the symmetry of the bonding states between Ni 3*d* and O 2*p* states in our system, we have measured the polarization dependence of ARPES spectra by changing the incident angle of the excitation light. Fig. 4.9 shows ARPES spectra of p(1×1)-clean Ni(111) and p(1×1)-0.88 ML O/Ni(111) surfaces observed with incident angle of 20° (s-polarization) and 60° (sp-polarization). In the figure, the spectral features **a**, **b** and **c** in the p(1×1)-clean Ni(111) surface show larger spectral intensities in s-polarization spectrum than those in sp-polarization spectrum.

In ARPES observed in normal emission mode, the features originated from electronic states with orbital moment perpendicular to the surface would be enhanced in s-polarization geometry. The results reveal that in p(1×1) clean Ni(111) surface, electronic states near E_F dominantly consist of Λ_3 symmetry states (Igarashi, Unger, Hirai and Fulde, 1994; Yamasaki and Fujiwara, 2003; Manghi, Bellini and Arcangeli,

1997). This is consistent to the fact that the easy magnetization axis of Ni is along [111] direction. In p(1×1)-0.88 ML O/Ni(111) surface, the spectral features **a**, **b** and **c** show larger intensities in sp-polarization spectrum than those in s-polarization spectrum. The initial-state symmetries of these features seem to be Λ_1 corresponding to $3d_{x2-y2}$ or $3d_{z2}$ in terms of 3*d* orbital in the central field. Since Ni $3d_{x2-y2}$ state does not make a bond with O 2*p* states and σ-bonding states between Ni $3d_{z2}$ and $2p_z$ would not show energy dispersion observed in Fig. 4.5, the electronic states responsible for the spectral features near E_F are assigned to $3d_{xz}$ and $3d_{yz}$ states, which make π bonding states with O $2p_x$ and O $2p_y$ states, respectively. Fig. 4.9 reveals that in O/Ni(111) surface the spectral features near E_F are due to the hybridization between Ni 3*d* and O 2*p* states, which decreases the contribution on the out-of-plane electron orbitals and suppresses in-plane magnetic anisotropy of Ni(111) surface by spin-orbit interaction. In the Ni/Cu(001) system, the in-plane magnetic anisotropy is dominant in the sample with Ni films of a few monolayers and perpendicular magnetic anisotropy increases with increase of the Ni film thickness. Since ARPES is a surface-sensitive experimental technique, the electronic structures obtained from ARPES spectra reveal characteristics of those within a few monlayers from the surface. Our results obtained in this study correspond to those at the thin end of Ni film in the O/Ni/Cu(001) system, where the in-plane magnetic anisotropy of Ni is suppressed.

In conclusion, the polarization dependence of ARPES spectra elucidates the electron orbital symmetry of the hybridization between Ni 3*d* and O 2*p* states at the O/Ni(111) interface. It is shown that $3d_{xz}$-$2p_x$ and $3d_{yz}$-$2p_y$ anti-bonding π states are responsible for the electronic states at the interface and enhancement of the perpendicular magnetic anisotropy in the oxygen-adsorbed nickel surface.

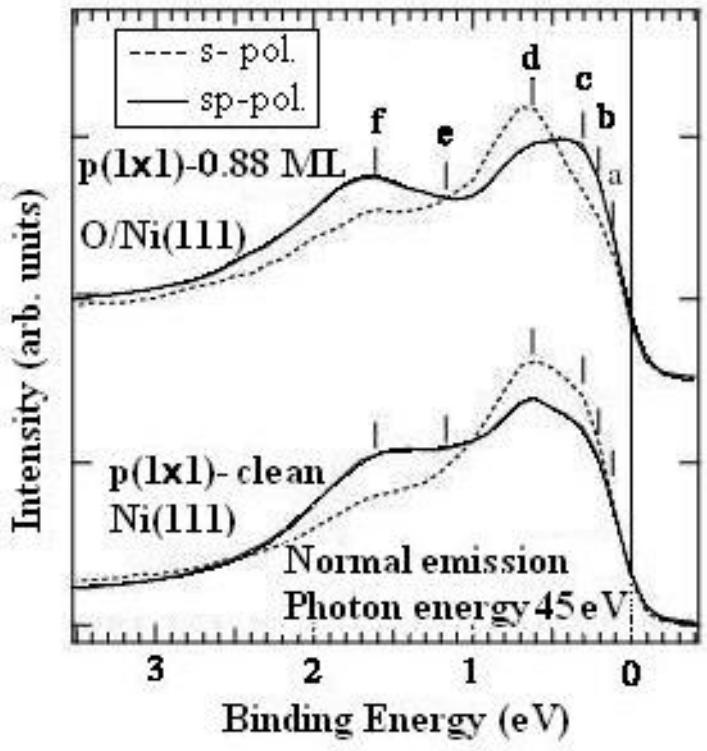

Fig. 4.9 Polarization dependence of ARPES spectra on the clean and p(1×1)-0.88 ML O/Ni(111) surfaces. The polarization was selected by changing incident angle of linearly polarized light on the Ni(111) surface. The incident angles at 20° and 60° correspond to s-polarization (dashed lines) and sp-polarization (solid lines), respectively. Tick markers correspond to the spectral features shown in Fig. 4.2.

4.5 Surface energy bands

The observed energy-band dispersions are compared with a first-principle surface energy-band calculation (Mittendorfer *et al*., 1999). Fig. 4.10 shows the surface energy-bands on the c(2x2)-0.51 ML and p(1x1)-0.88 ML O/Ni(111) surfaces along the Γ-Σ-M direction in surface BZ. M point of surface BZ corresponds to a line at 1.46 $Å^{-1}$ of wave vector. Asterisks with error bars represent energy-band dispersions on the c(2x2)-0.51 ML O/Ni(111) surface and open circles these on the p(1x1)-0.88 ML O/Ni(111) surface. For simplicity, error bars for open circles are omitted. These energy-band dispersions are obtained by second-derivative calculation of subtracted spectra in Fig. 4.5 and error bars correspond to a band width due to correlation effect as well as instrumental resolution. Thick solid and dashed lines represent majority-spin and minority-spin energy-band calculations by Mittendorfer *et al*., respectively. Since the original report on surface energy-band calculation shows only points representing surface states in the surface BZ, we drew lines connecting these points as shown in Fig. 4.10. It should be noted that the negative spectral features in the binding-energy range between 0.1 eV and 0.8 eV measured on the O/Ni(111) surfaces do not appear in Fig. 4.10, because second derivative method was used to obtain the energy-band dispersions.

A difference between energy-band dispersions obtained from the c(2×2)-0.51 ML and p(1×1)-0.88 ML O/Ni(111) surfaces is found to be very small over the first BZ. This result indicates that our computer-processing methods are properly performed for the surface energy-band mapping. The most distinctive difference is an energy band located near the Fermi level in the wave-vector range between 0 and 0.6.

The flat band structure on the c(2×2)-0.51 ML O/Ni(111) surface might be influenced by the enhanced interfacial band discussed in previous section.

Our surface energy-band structures are in poor agreement with the first-principle surface energy-band calculation (Mittendorfer *et al*., 1999). This discrepancy may come from a deviation from single-particle approximation, since the energy-band theory is interpreted as one of approximation in the framework of single-particle Green function in many-electron system. A spectral function, which is imaginary part of Green function, is defined by Hartree-Fock (HF) energy and self energy describing a shift from HF energy and a width of spectral function due to electron-electron screening and scattering, respectively.

$$G_{k\sigma}(\omega) = \left[\omega - \varepsilon_{k\sigma} - \Sigma_{k\sigma}(\omega)\right]^{-1} \tag{4.1}$$

Here, G represents Green function, k wave number, σ spin, ω energy, ε HF energy and Σ self energy. A complex self energy indicates that real and imaginary parts of self energy correspond to the energy shift and the spectral width, respectively.

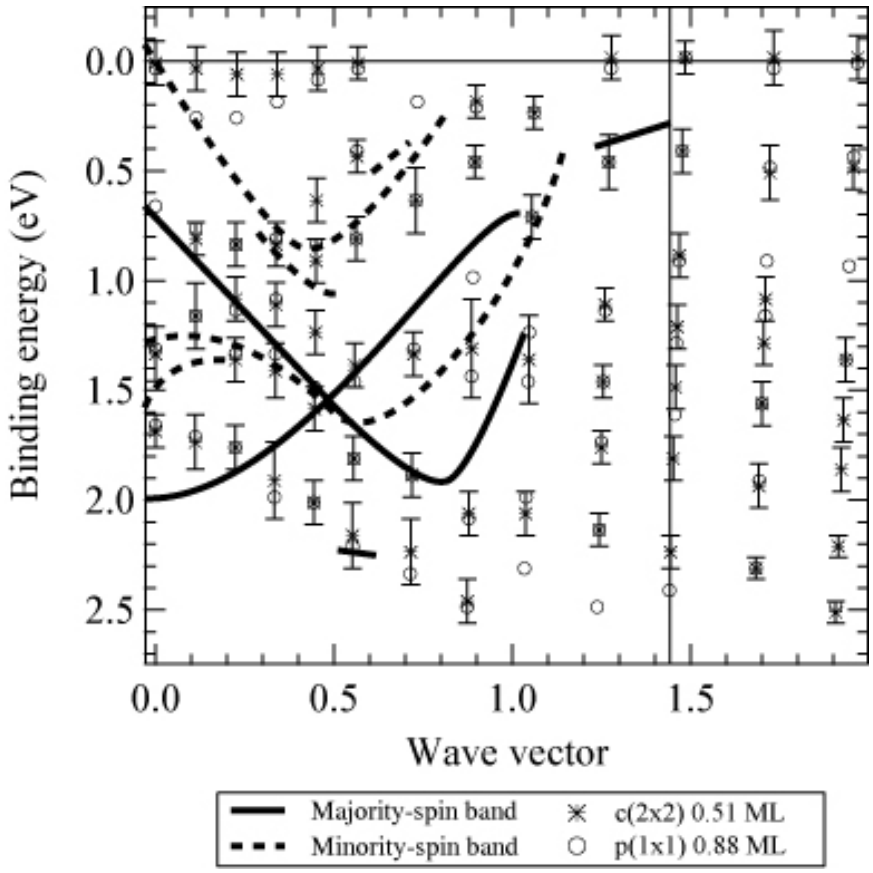

Fig. 4.10 Surface energy-band map compared with spin-dependent surface energy-band calculation along the Γ-Λ-M direction in the surface BZ (Mittendorfer *et al*., 1999). M point in the surface BZ corresponds to a line at 1.46 $Å^{-1}$. Asterisks with error bars represent energy-band dispersions obtained by second-derivative process of c(2×2)-0.51 ML O/Ni(111) spectra. Open circles without error bars indicate energy-band dispersions on p(1×1)-0.88 ML O/Ni(111) surface. Thick lines are majority-spin bands and dashed lines minority-spin bands.

Recent theoretical progress enables us to estimate the complex self energy and exchange-correlation effect in HF energy (Mittendorfer *et al*., 1999; Grechnev *et al*., 2007). According to the reported calculations on the nickel bulk-band structure (Manghi *et al*., 1997), self-energy correction of a majority-spin band is stronger than that of minority-spin band. A lack of an electron in minority-spin band results in a small screening effect on the minority-spin electron. Furthermore, surface energy-band structure is rather different from bulk one, since the reduced coordination number of the surface atoms makes correlation effects more important. In addition, the screening effect is less effective for the surface atoms, which increases correlation effects. Therefore, the self energy of a nickel atom at the surface is obviously quite different from that for bulk atoms. To elucidate the discrepancy between surface energy-band calculation and ARPES energy-band map, the observed energy-band mapping is compared with the quasi-particle energy-band calculation including self-energy correction (Grechnev *et al*.). Fig. 4.11 shows comparison between the observed surface energy-band map and full-potential linear-muffin-tin-orbital local-density approximation plus dynamical mean-field theory (LDA+DMFT) by Grechnev *et al.*, According to Grechnev *et al*., a super-lattice structure consists of three-layer nickel-slabs separated by 30-Å vacuum area in [111] direction. Left and right figures represent the comparison of our energy-band map shown in Fig. 4.10 with majority-spin and minority-spin calculated bands, respectively. The theoretical result is shown by rainbow-color scale that red is a high spectral density and blue is a low spectral density. In a grayscale-printed paper, lighter area corresponds to energy-band structure.

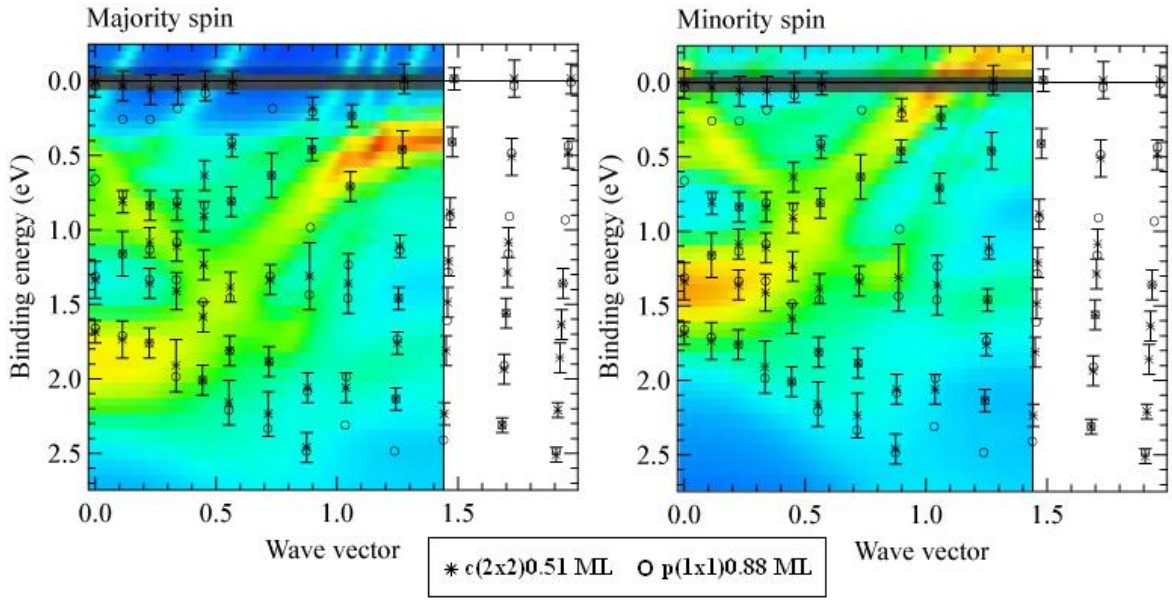

Fig. 4.11 Surface energy-band map compared with spin-dependent surface quasi-particle band calculation along the Γ-Λ-M direction in the surface BZ (Grechnev *et al*., 2007). M point in the surface BZ corresponds to a line at 1.46 $Å^{-1}$. Left and right figures represent majority-spin and minority-spin bands with rainbow-colored scale, respectively. Asterisks with error bars represent energy-band dispersions obtained by second-derivative process of c(2×2)-0.51 ML O/Ni(111) spectra. Open circles without error bars indicate energy-band dispersions on p(1×1)-0.88 ML O/Ni(111) surface.

The experimental energy-band shows in fair agreement in the binding-energy range between 0.8 eV and 1.7 eV around Γ point in the surface BZ of both spin bands. The bands in the binding-energy range between 0.0 eV and 0.5 eV around M point agree with the theory as well. Even though the minority-spin band is located at unoccupied state around M point, the exchange splitting of these bands seems to be 0.5±0.2 eV. In the minority-spin band, the energy-band dispersion from E_F at Γ point to 1.2 eV at 0.9 $Å^{-1}$ has no corresponding feature in the experimental band structure. In the majority-spin band, the energy-band dispersion near E_F from Γ point to 0.6 $Å^{-1}$ shows in good agreement with sp-like surface band that was identical to the report by Himpsel *et al.* (1978), since the energy range below 0.2 eV has a few contribution from majority-spin *d* bands. Since all the other experimental structures are located in the bulk-projected band where the theoretical structures are smeared out, these energy-band structures come from bulk energy bands.

CHAPTER V

CONCLUSION

I investigated surface electronic states of clean and oxygen-adsorbed Ni(111) surfaces using angle-resolved photoemission spectroscopy. Upon oxygen adsorption, c(2×2) and p(1×1) structures appear in 0.51 ML and 0.88 ML O/Ni(111) surfaces, respectively. Comparing experimentally obtained energy dispersion of the surface electronic states with molecular-orbital and energy-band calculations on O/Ni, it is shown that $3d_{xz}$-$2p_x$ and $3d_{yz}$-$2p_y$ anti-bonding π states are responsible for the electronic states at the interface and enhancement of the perpendicular magnetic anisotropy in the oxygen-adsorbed Ni(111) surfaces. Surface energy-band dispersions on Ni(111) show in better agreement with quasi-particle bands than ordinary LDA bands of ferromagnetic Ni surface, which suggests that self-energy correction is significant in surface energy-band calculation.

REFERENCES

REFERENCES

Adachi, H., Tsukada, M. and Satoko, C. (1978). Discrete Variational Xα ClusterCalculations. I. Application to Metal Clusters. **J. Phys. Soc. Jpn**. 45: 875.

Amemiya, K., Sakai, E., Matsumura, D., Abe, H., Ohta, T. and Yokoyama, T. (2005). Spin-reorientation transition of Ni/Cu(100) and CO/Ni/Cu(100): Separation of the surface and bulk components of the x-ray magnetic circular dichroism spectrum. **Phys. Rev. B** 71: 214420-214427.

Argaman, N. and Makov, G. (1999). **Density Functional Theory-an introduction** [On-line]. Available: http://www.yukawa.kyoto-u.ac.jp/abs/physics/9806013.html

Baberschke, K. (1996). The magnetism of nickel monolayers. **Appl. Phys. A** 62: 417.

Berglund, C. N. and Spicer, W. E. (1964). Photoemission studies of copper and silver: theory. **Phys. Rev**. 136 (4A): 1030-1044.

Bouchaert, L.P., Smoluchowski, R. and Wigner, E. (1936). Theory of Brillouin zones and symmetry properties of wave functions in crystals. **Phys. Rev**. 50: 58-67.

Bruno, P. and Renard, J. P. (1989). Magnetic surface anisotropy of transition metal ultrathin films. **Appl. Phys. A** 49: 499-506.

Connolly, J. W. D. (1967). Energy-band in ferromagnetic nickel. **Phys. Rev**. 159: 415-426.

Davis, L. E., MacDonald, N. C., Palmberg, P. W., Riach, G. E., Weber, R.E. (1996). **Handbook of Auger Electron Spectroscopy**. Physical Electronics.

Davisson, C. J. and Germer, L. H. (1927). Diffraction of Electrons by a Crystal of Nickel. **Phys. Rev**. 30: 705-740.

Eberhardt, W. and Plummer, E. W. (1980). Angle-resolved photoemission determination of the band structure and multielectron excitations in Ni. **Phys. Rev. B** 21 (8): 3245-3255.

Ertl, G. and Kuppers, J. (1985). Low energy Electrons and Surface Chemistry. VCH, Weiheim.

Feuerbacher, B. and Willis, R.F. (1976). Photoemission and electron states at clean surfaces**. J. Phys. C: Solid State Phys**. 9: 169-216.

Goldmann, A., Dose, V. and Borstel, G. (1985). Empty electronic states at the (100), (110), and (111) surfaces of nickel, copper, and silver. **Phys. Rev. B** 32: 1971-1980.

Gradmann, U. (1986). Magnetic surface anisotropies. **J. Magn. Magn. Master** (54-57): 733-776.

Grechnev, A., Marco, I.D., Katsnelson, M. I., Lichtenstein, A. I., Wills, J. and Eriksson, O. (2007). Theory of bulk and surface quasiparticle spectra for Fe, Co, and Ni. **Phys. Rev. B** 76: 035107-035120.

Heine, V. (1960). Group theory in quantum mechanics. London: Pergamon Press.

Hermanson, J. (1977). **Solid State Commun**. 22: 9.

Himpsel, F. J. and Eastman, D. E. (1978). Observation of a Λ1-Symmetry Surface state on Ni(111). **Phys. Rev. Lett**. 41: 507-511.

Himpsel, F. J., Knapp, J. A. and Eastman, D. E. (1979). Experimental energy-banddispersions and exchange splitting for Ni. **Phys. Rev. B** 19: 2919-2927.

Hitachi Global Storage Technologies. (2006). **Hitachi** [On-line]. Available: http://www. hitachigst.com/hdd/hddpdf/tech/chart13.pdf.

Hohenberg, P. and Kohn, W. (1964). Inhomogeneous Electron Gas. **Phys. Rev**. 136 : B864.

Hong, J., Wu, R. Q., Lindner, J., Kosubek, E. and Baberschke, K. (2004). Manipulation of Spin Reorientation Transition by Oxygen Surfactant Growth: A Combined Theoretical and Experimental Approach. **Phys. Rev. Lett**. 92: 147202.

Hüfner, S. (1996). **Photoelectron spectroscopy** (2nd ed). Berlin: Springer-Verlag.

Igarashi, J., Unger, P., Hirai, K. and Fulde, P. (1994). Local approach to electron correlations in ferromagnetic nickel. **Phys. Rev. B** 49: 16181-16190.

Ishii, T. (1989). Solid state spectroscopy in the vacuum ultraviolet and soft X-ray region. In H. Winick, D. Xian, Ming-han Ye and T. Huang (eds.). **Applications of synchrotron radiation** (pp. 371-514). New York: Gordon and Breach Science Publishers.

Kilcoyne, A. L. D., Woodruff, D. P., Rowe, J. E. and Gaylord, R. H. (1989). Comparative study of angle-resolved valence-band photoemission from half-monolayer structures of C, N, and O on Ni(100). **Phys. Rev. B** 39: 12604-12611.

Kinoshita, T., et al. (1993). Evidence for Fano interference in spin polarization of the 6-eV satellite in Ni valence-band photoemission. **Phys. Rev. B** 47 (11): R6787-6790.

Kisker, E., Schröder, K., Gudat, W., and Campagna, M. (1985). Spin-polarized angle-resolved photoemission study of the electronic structure of Fe(100) as a function of temperature. **Phys. Rev. B** 31 (1): 329-339.

Kittel, C. (1963). **Quantum theory of solids**. New York: John Wiley & Sons, Inc.

Kittel, C. (1967). **Introduction to solid state physics**. New York: John Wiley & Sons, Inc.

Kohn, W. and Sham, L. J. (1965). Self-Consistent Equations Including Exchange and Correlation Effects. **Phys. Rev**. 140 : A1133.

Knox, R. S. (1963). **Theory of exitons in solid state physics**. New York: Academic Press.

Kresse, G. and Hafner, J. (1993). Ab initio molecular dynamics for liquid metals. **Phys. Rev. B** 47: RC558.

Manghi, F., Bellini. V. and Arcangeli, C. (1997).On-site correlation in valence and core states of ferromagnetic nickel. **Phys. Rev. B** 56: 7149-7161.

Mittendorfer, F., Eichler, A. and Hafner, J. (1999). Molecular precursors in thedissociative adsorption of O2 on Ni(111). **Surf. Sci**. (433-435): 756-760.

Moruzzi, V. L., Janak, J. F. and Williams, A. R. (1978) **Calculated electronic properties of metals**. New York: Pergamon.

Nakajima, H., Buddhakala, M., Chumpolkulwong, S., Supruangnet, R., Kakizaki, A. and Songsiriritthigul, P. (2007). **Proc. 9th Int. Conf. Synchrotron Radiation Instrumentation**. J-Y. Choi and S. Rah (eds.). American Institute of Physics,New York: 543.

National Synchrotron Research Center. (2006). **The new experimental station of the BL4 beamline at Siam Photon Laboratory** [Online]. Available: http://www.nsrc.or.th/_contents/TechSpec/Bl4/Images/BL061023/MultiUHV070626.pdf

Prayoon Songsiriritthigul, et al. (2001). Comparison of varied-line-spacing plane grating and varied-line-spacing spherical grating monochromators for the Siam Photon Source. **Nuclear Instruments and Methods in Physics Research A** 467-468: 593-596.

Prayoon Songsiriritthigul, et al. (2004). The commissioning results of the first beamline at the Siam Photon Laboratory. In T. Warwick, J. Arthur, H. A. Padmore, and J. Stöhr (eds.). **Synchrotron radiation instrumentation: eight international conference** (pp. 372-375). USA: Springer-Verlag.

Prayoon Songsiriritthigul, Weerapong Pairsuwan, Ishii, T., and Kakizaki, A. (2003). Beamline at Siam Photon Laboratory. **Nuclear Instruments and Methods in Phys. Res. B** 199: 565-568.

Quinn, J. J. (1962). Range of Excited Electrons in Metals. **Phys. Rev**. 126: 1453-1457.

Rudberg, E. (1930). **Proc. Roy. Soc**. (London) A127, 111.

Schulz, B. and Babershke, K. (1994). Crossover from in-plane to perpendicular magnetization in ultrathin Ni/Cu(001) films. **Phys. Rev. B** 50: 13467-13471.

Seitz, F. (1940). **Modern theory of solids**. New York: McGraw-Hill, Inc.

Slater, J.C. (1965). **Quantum theory of molecules and solids** (Vol. II). New York: McGraw-Hill, Inc.

Soda, K., Mori, T., Onuki, Y., Komatsubara, T. and Ishii, T. (1988). Optical density of states of valence electrons in CeCu2Si2. **J. Phys. Soc. Japan** 57: 1699-1706.

Spicer, N.E. and Krolikowski, W.F. Photoemission studies of the nobel metal: I. Copper. **Phys. Rev**. 185 (3): 882-900.

Tanuma, S., Powell, C. J. and Penn, D.R. (1990). Material Dependence of Electron Inelastic Mean Free Paths at Low Energies. **J. Vac. Sci. Technol**. A8: 2213-2216.

Thermo Vacuum Generators catalogue. (2006). **Thermo Vacuum** [Online]. Available: http://www.thermovacgen.com

Thuler, M. R., Benbow, R. L. and Hurych, Z. (1983). Photoemission intensities at the 3p threshold resonance of NiO and Ni. **Phys. Rev. B** 27: 2082-2088.

Uiberschke, C. et al., (1999). Lattice Relaxation Driven Reorientation Transition in Nin/Cu(100). **Phys. Rev. Lett**. 82, 1289-1292.

Wakoh, S. and Yamashita, J. (1964). Fermi surface of Ni. **J. Phys. Soc. Japan** 19 (8): 1342-1350.

Wakoh, S. (1965). Band structure of metallic copper and nickel by a self-consistent procedure. **J. Phys. Soc. Japan** 20 (10): 1894-1901.

Weling, F. and Callaway, J. (1982). Semiempirical description of energy bands in nickel. **Phys. Rev. B** 26: 710-719.

Wild, K. (1981). **Auger electron spectroscopy (AES) for surface analysis. Vacuum**. 3: 183-194.

Wiwat Wongkokua. (2004). **Study of Nickel (111) by Photoemission Spectroscopy**. Ph.D. Dissertion, Suranaree University of Technology, Thailand.

Yamasaki, A. and Fujiwara, T. (2003). Electronic Structure of Transition Metals Fe, Ni and Cu in the GW Approximation. **J. Phys. Soc. Jpn**. 72: 607.

Yeh, J. J. and Lindau, I. (1985). **Atomic Data and Nuclear Data Tables** [On-line]. Available: http://ulisse.elettra.trieste.it/services/elements/WebElements.html

Ziman, J. M. (1963). **Principles of the theory of solids**. London: Cambridge University Press.

APPENDICES

APPENDIX A

MOLECULAR ORBITAL CALCULATION

We consider two hydrogen atoms. Each atom has a one-electron state such as Ψ_A for atom A and Ψ_B for atom B, when each atom is isolated. In a molecular, molecular orbital Ψ is similar to Ψ_A near atom A, while it's similar to Ψ_B near atom B. Heitler-London method assumed Ψ can be represented by product of Ψ_A and Ψ_B, while molecular-orbital method based on LCAO assumed Ψ can be represented by sum of Ψ_A and Ψ_B as follows

$$\Psi = c_0\left(c_A\Psi_A + c_B\Psi_B\right). \tag{A.1}$$

Here, Ψ_A and Ψ_B are assumed to be positive value as s orbital. c_0 represents a normalized factor for Ψ, and c_A and c_B are coefficient factors for Ψ_A and Ψ_B, respectively. Each wave function is normalized as

$$\left.\begin{aligned} &\langle\Psi|\Psi\rangle = 1, \quad \langle\Psi_A|\Psi_A\rangle = 1, \quad \langle\Psi_B|\Psi_B\rangle = 1 \\ &\langle\Psi|\Psi\rangle = c_0^2\left\{c_A^2\langle\Psi_A|\Psi_A\rangle + c_A^2\langle\Psi_B|\Psi_B\rangle + 2c_Ac_B\langle\Psi_A|\Psi_B\rangle\right\} = 1. \end{aligned}\right\} \tag{A.2}$$

When c_0 is substituted into equation (A.1), Ψ is expressed as

$$\left.\begin{aligned} \Psi &= \frac{1}{\sqrt{c_A^2 + c_B^2 + 2c_Ac_BS}}\left(c_A\Psi_A + c_B\Psi_B\right). \\ S &= \langle\Psi_A|\Psi_B\rangle. \end{aligned}\right\} \tag{A.3}$$

Here, S is introduced as overlap integral corresponding to the overlap between two one-electron wave functions in the molecule. If S is zero, two functions are separated infinitely. If S is unity, two functions are completely overlapped.

Once we obtain the wave function of molecule, we can calculate, in principle, the energy. The expectation value of the molecule is

$$\left.\begin{aligned} E &= \langle \Psi | H | \Psi \rangle. \\ &= \frac{\left\{ c_A^* \langle \Psi_A | + c_B^* \langle \Psi_B | \right\} H \left\{ c_A | \Psi_A \rangle + c_B | \Psi_B \rangle \right\}}{c_A^2 + c_B^2 + 2 c_A c_B S}. \\ &= \frac{c_A^2 \langle \Psi_A | H | \Psi_A \rangle + c_B^2 \langle \Psi_B | H | \Psi_B \rangle + 2 c_A c_B \langle \Psi_A | H | \Psi_B \rangle}{c_A^2 + c_B^2 + 2 c_A c_B S}. \\ &= \frac{c_A^2 H_{AA} + c_B^2 H_{BB} + 2 c_A c_B H_{AB}}{c_A^2 + c_B^2 + 2 c_A c_B S}. \end{aligned}\right\} \quad \text{(A.4)}$$

Here, H_{AA} represents energy of electron around atom A

$$H_{AA} = \langle \Psi_A | H | \Psi_A \rangle \quad \text{(A.5)}$$

where H_{AA} is negative, since electronic state is stable around atom A. H_{BB} for atom B is the same as H_{AA} for atom A.

The minimum energy is given by the following condition

$$\frac{\partial E}{\partial c_A} = \frac{\partial E}{\partial c_B} = 0 \quad \text{(A.6)}$$

where E is defined as

$$E\left(c_A^2 + c_B^2 + 2 c_A c_B S\right) = c_A^2 H_{AA} + c_B^2 H_{BB} + 2 c_A c_B H_{AB} \quad \text{(A.7)}$$

The partial differentiation in equation (A.6) is performed using the equation (A.7).

$$\left.\begin{aligned}\frac{\partial E}{\partial c_A}\left(c_A^2+c_B^2+2c_Ac_BS\right)+E\left(2c_A+2c_BS\right)&=2c_AH_{AA}+2c_BH_{AB}\\ \frac{\partial E}{\partial c_B}\left(c_A^2+c_B^2+2c_Ac_BS\right)+E\left(2c_B+2c_AS\right)&=2c_BH_{BB}+2c_AH_{AB}.\end{aligned}\right\} \quad (A.8)$$

Equation (A.8) are substituted into equation (A.6)

$$\left.\begin{aligned}c_A\left(H_{AA}-E\right)+c_B\left(H_{AB}-ES\right)&=0\\ c_A\left(H_{AB}-ES\right)+c_B\left(H_{BB}-E\right)&=0.\end{aligned}\right\} \quad (A.9)$$

Finally, the energy E is determined as the equation;

$$\left(H_{AA}-E\right)\left(H_{BB}-E\right)-\left(H_{AB}-ES\right)^2=0. \quad (A.10)$$

Suppose that atom A is the same as atom B, S is positive and H_{AB} is negative. $H_{BB}=H_{AA}$., equation (A.10) is solved as

$$\left.\begin{aligned}E_a&=\frac{H_{AA}-H_{AB}}{1-S}\\ E_b&=\frac{H_{BB}+H_{AB}}{1+S}\\ E_a&>H_{AA}>E_b\end{aligned}\right\} \quad (A.11)$$

where E_b represents energy of bonding state, while E_a energy of anti-bonding state. The overlap integral is important factor to analyze the bonding formation between various orbitals showing different parity as shown in Fig. A1.

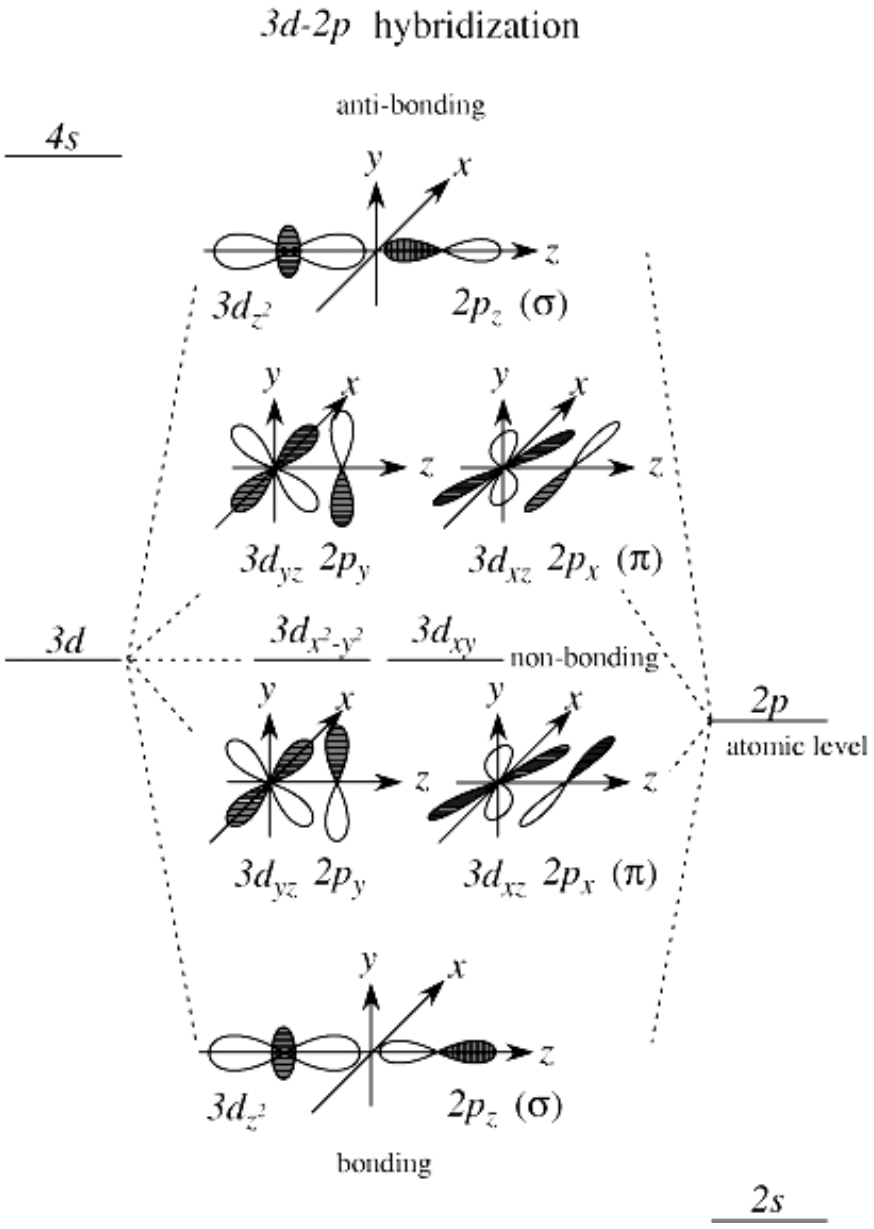

Fig. A.1 Bonding energy diagram between 3*d* and 2*p* atomic orbitals.

APPENDIX B

ENERGY BAND CALCULATION

Let consider *N*-electron system in the external field *v*(r) at position r Hamiltonian of this system is described using atomic units as follows;

$$\left.\begin{aligned} H &= T + V + U \\ T &= \sum_i -\nabla_i^2 \\ V &= \sum_i v(r_i) \\ U &= \sum_{i \le j} \frac{2}{|r_i - r_j|}. \end{aligned}\right\} \quad \text{(B.1)}$$

From variational method, ground-state wave function Ψ at energy E_0 is given by solving equations below.

$$\left.\begin{aligned} H\Psi &= E_0\Psi \\ E_0[\Psi] &= \mathrm{Min}\langle\Psi|H|\Psi\rangle \\ \langle\Psi|\Psi\rangle &= N. \end{aligned}\right\} \quad \text{(B.2)}$$

Since the electron density is defined as $\rho(r) = \Psi^*\Psi$,Ψ, ρ and E_0 can be expressed by *v*(r).

$$\left.\begin{aligned} \Psi &= \Psi[v] \\ \rho &= \rho[v] \\ E_0 &= E_0[v]. \end{aligned}\right\} \quad \text{(B.3)}$$

Since v(r) is determined as three axes such as (x, y, z), N-electron wave function is described by 3N coordinates. In contrary, density functional theory (DFT) provides a simple solution to describe many-electron wave function by using density of electrons that is determined by only three coordinates (Hohenberg and Kohn, 1964).

$$\left.\begin{aligned} v &= v[\rho] \\ \Psi &= \Psi[\rho] \\ E_v[\rho] &= T[\rho] + \int v\rho dv + U[\rho] \\ &= T + \int v\rho dv + \frac{1}{2}\int \frac{\rho(r)\rho(r')}{|r-r'|} dr dr' + E_{XC} \\ &= T_S + \int v\rho dv + E_H + E_{XC} + (T - T_S) \\ &= T_S + \int v\rho dv + E_H + \tilde{E}_{XC}\,. \end{aligned}\right\} \quad \text{(B.4)}$$

Here, E_H represents Hartree energy, E_{XC} exchange-correlation energy and T_S kinetic energy based on independent-particle approximation. Many-electron effect is included into E_{XC} except Hartree energy. T_S and ρ are calculated by using single particle wave function as follows;

$$\left.\begin{aligned} T_S &= \left\langle \Psi \middle| -\sum_i \nabla_i^2 \middle| \Psi \right\rangle \\ &= -\sum_i \int \psi_i^* \nabla_i^2 \psi_i dv \\ \rho &= \sum_i \psi_i^* \psi_i . \end{aligned}\right\} \quad \text{(B.5)}$$

Hohenberg and Kohn introduce effective potential V_{eff} to solve Schrödinger equation of non-interacting many-electron system (Kohn and Sham, 1965).

$$\left.\begin{aligned} E_v[\rho] &= E_B[\rho] + E_D[\rho] \\ E_B[\rho] &= T_S + \int V_{eff}\, \rho dv \\ E_D[\rho] &= -\int V_{eff}\, \rho dv + \int v \rho dv + E_H + \tilde{E}_{XC} . \end{aligned}\right\} \quad \text{(B.6)}$$

From variational method, two conditions are required for equation (B.6).

$$\left.\begin{aligned} \frac{\delta E_B}{\delta \rho} &= 0 \\ \frac{\delta E_D}{\delta \rho} &= 0. \end{aligned}\right\} \quad \text{(B.7)}$$

Equation (B.6) is substituted into equation (B.7) and following equations are obtained.

$$\left.\begin{aligned} -\nabla_i^2 \psi_i(r) + V_{eff}(r) \psi_i(r) &= \varepsilon_i \psi_i(r) \\ V_{eff}(r) &= v(r) + \int \frac{\rho(r')}{|r - r'|} dv' + V_{XC}(r) \\ \rho(r) &= \sum_i |\psi_i|^2 \\ V_{XC}(r) &= \frac{\delta \tilde{E}_{XC}[\rho]}{\delta \rho}. \end{aligned}\right\} \quad \text{(B.8)}$$

These equations are called Kohn-Sham equation. Single particle wave function is determined in first Schrödinger equation. Then, ρ and V_{XC} are calculated from third and fourth equations, respectively. Finally, V_{eff} using ρ and V_{XC} is obtained in second equation, and first equation is solved with new V_{eff}. A simple iteration process is illustrated in Figure 0002.

In general, exchange-correlation energy is approximated by the energy of uniformed electron gas in local area (LDA).

$$\tilde{E}_{XC}[\rho] = \int \rho(r)\varepsilon_{XC}(\rho(r))dv. \tag{B.9}$$

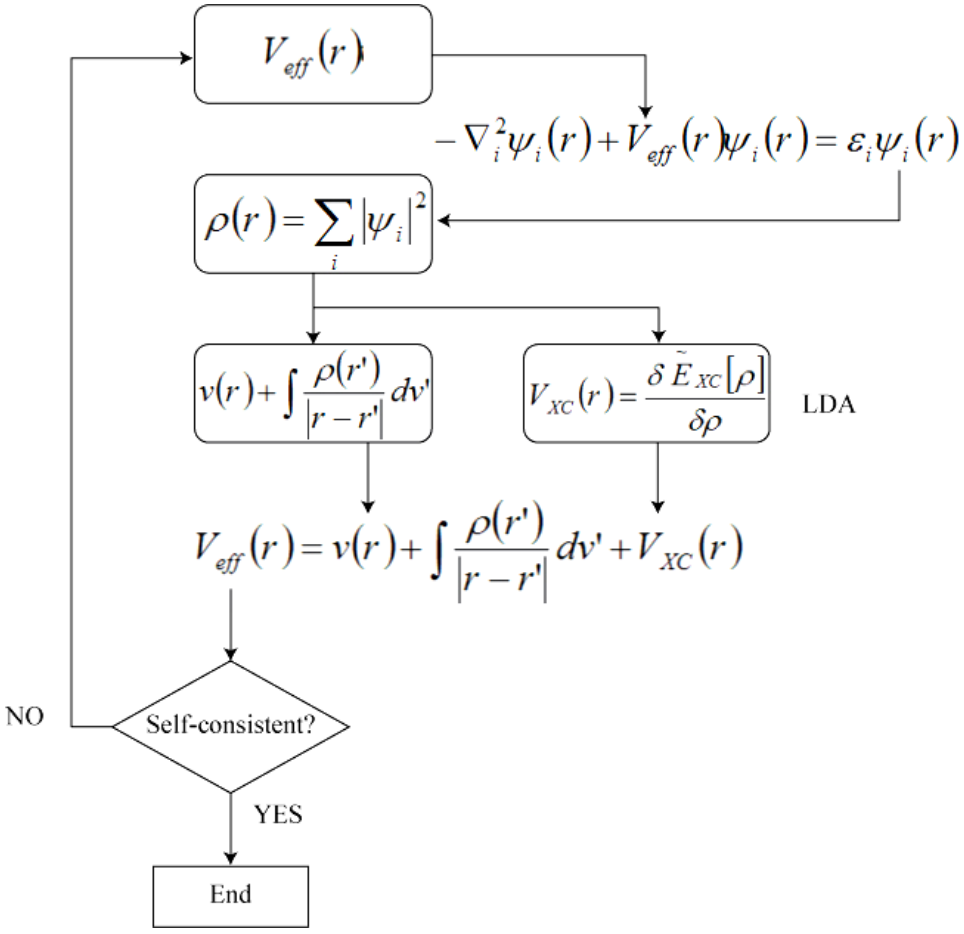

Fig. B.1 Iteration process on DFT calculation.

CURRICULUM VITAE

Mr. Somchai Chumpolkulwong

Date of birth: 19 February 1973

Place of birth: Bangkok, Thailand.

Nationality: Thai.

Address: Department of Physics, Faculty of Science, Udonthani Rajabhat University, Udonthani 41000, Thailand.

Education

Academic year	
1991-1995	Kasetsart University, Bangkok, Thailand.
	Bachelor of Science (Physics).
1996-2000	King Mongkut's University of Technology Thonburi, Thailand.
	Master of Engineering (Material Technology).
2000-2005	Suranaree University of Technology, Nakhon Ratchasima, Thailand.
	Ph.D. in Physics

Academic Experience

1996-at present	Lecturer, Department of Physics, Faculty of Science, Udonthani Rajabhat University**,** Udonthani, Thailand.